The Pennsylvania State University

The Graduate School

College of Earth and Mineral Sciences

ANALYSIS OF CAPILLARY PRESSURE AND RELATIVE PERMEABILITY EFFECTS ON THE PRODUCTIVITY OF NATURALLY FRACTURED GAS-CONDENSATE RESERVOIRS USING COMPOSITIONAL SIMULATION

A Thesis in

Energy and Mineral Engineering

by

Bander Nasser Al Ghamdi

Submitted in Partial Fulfillment

of the Requirements

for the Degree of

Master of Science

December 2009

The thesis of Bander Nasser Al Ghamdi was reviewed and approved* by the following:

Luis Felipe Ayala H.
Assistant Professor of Petroleum and Natural Gas Engineering
Thesis Advisor

Yaw D. Yeboah
Professor and Department Head of Energy and Mineral Engineering

Robert Watson
Associate Professor Emeritus of Petroleum and Natural Gas Engineering and Geo-Environmental Engineering

Zuleima Karpyn
Assistant Professor of Petroleum and Natural Gas Engineering

***Signatures are on file in the Graduate School**

ABSTRACT

The developments of gas-condensate reservoirs are highly dependent on the thermodynamic behavior of the fluids in place. During the depletion of gas-condensate reservoirs, the gas condenses as the pressure of the reservoir reduces below the hydrocarbon dew point pressure, which introduces a liquid phase called retrograde condensate. In such conditions, the productivity experience a reduction in recovery due to the appearance of condensate near the production channels, which in turn reduces the overall flow of hydrocarbons to the surface. The phase behavior of the fluids in place impacts the production scheme of gas-condensate reservoirs, since the recovery of condensate is highly dependent on the changes in composition. In this study, the productivity of naturally fractured gas-condensate reservoirs is addressed using a compositional simulation model to examine the effects of capillary pressure and relative permeability on the recovery of gas-condensate fluids.

Capillary pressure is a function of saturation and it controls the distribution of fluids in the pore spaces of a reservoir. The role of capillary pressure in the distribution of fluids in the reservoir can become more relevant in naturally fractured reservoirs, where the transport of fluids between the matrix and the fractures depends on the capillary pressure. In addition, the deliverability of gas-condensate reservoirs in such conditions is controlled by the transport properties, which are the relative permeabilities between the fluids in a pore-scale. Therefore, this study is devoted to evaluate the growth of condensate coating by examining different compositions (light/heavy) with the activation of the capillary pressure forces, while keeping the depletion rate constant, and deactivating the diffusion effect in the system.

A compositional simulation model was utilized for the evaluation of the influence of fluid characteristics on the severity of condensate coating while assigning tight matrix permeability of 0.001 md, 1 psi/day for depletion rate, and zero capillary pressures. The analysis of the condensate coating on the edges of the matrix blocks lead to the conclusion that the saturation pressure point is controlled by the concentration of heavy components. The sooner the saturation pressure is reached, the sooner condensate appears and hinders the overall recovery of fluids. Using the same conditions applied to the different composition concentration while activating the capillary pressure effect at different pore size distribution indexes (1.5 to 7); the fluid distribution,

movement, and recovery, had a similar behavior indicating that the capillary pressure had insignificant influence on the reservoir fluids behavior. On the other hand, the effect of relative permeabilities showed dependency on the amount of condensate content in the reservoir. The more condensation that takes place, the more influence is applied by the relative permeability curves. The major variable that enhanced the oil-gas relative permeability curve was the fracture parameter (λ) obtained by van Genuchten's (1980) to calculate the oil and gas relative permeabilities. Several values were used to address the fracture parameter to influence the position of the oil-gas relative permeability curve. As a result, it appeared that the influence depends on the amount of condensate content in the reservoir. The more condensation that takes place, the more influence is applied by the relative permeability curves.

TABLE OF CONTENTS

LIST OF FIGURES

LIST OF TABLES

NOMENCLATURE

A_x = total area perpendicular to the flow in the x-direction, ft^3

A_y = total area perpendicular to the flow in the y-direction, ft^3

A_z = total area perpendicular to the flow in the z-direction, ft^3

B_w = water formation volume factor, RB/STB

c_w = water compressibility, psi^{-1}

c_ϕ = pore volume compressibility, psi^{-1}

d = depth of the typical representative matrix block of a naturally fractured reservoir, ft

D_{eff} = effective diffusion coefficient of the gas phase, ft^2/day

D_{mx} = diffusion transmissibility coefficient in the x-direction

D_{my} = diffusion transmissibility coefficient in the y-direction

D_{mz} = diffusion transmissibility coefficient in the z-direction

g = acceleration of gravity, ft/s^2

g_c= conversion factor, 32.174 lb-ft/lbf-s^2

G = depth measured positive in the downward direction, ft

h = thickness, ft

k = absolute permeability, md

k_f = fracture permeability, md

k_m = matrix permeability, md

k_{rg} = relative permeability of the gas phase

k_{ro} = relative permeability of the condensate phase

k_{rog} = relative permeability to oil in the two-phase oil-gas system at irreducible water

k_{row} = relative permeability to oil in a two-phase water-oil system

k_{rw} = relative permeability of the water phase

k_x = absolute permeability in the x- direction, md or perms

k_y= absolute permeability in the y- direction, md or perms

k_z = absolute permeability in the z- direction, md or perms

K_m = vapor-liquid equilibrium ratio of the m-th component in the hydrocarbon mixture

L = size of a rectangular matrix block (d = w = h), ft

M_m = rate of external withdrawal/injection of m-th component in the control volume, $\frac{RB\ .\ lbmol}{RCF\ .\ Day}$

M_m^l = molar flow rate of m-th component entering/leaving perforation l in a multilayered well, $\frac{RB\ .\ lbmol}{RCF\ .\ Day}$

MW_m = molecular weight of the m-th component, lb/lbmol

n_c = total number of components of the hydrocarbon mixture

n_x = total number of gridblocks in the x-direction

n_y = total number of gridblocks in the y-direction

n_z = total number of gridblocks in the z-direction

N_t = total molar rate of hydrocarbon fluids leaving or entering the reservoir, $\frac{RB\ .\ lbmol}{RCF\ .\ Day}$

N_g = molar rate of fluids that is produced as gas on the surface, $\frac{RB\ .\ lbmol}{RCF\ .\ Day}$

N_m = molar rate of m-th component leaving or entering the control volume, lbmol/day

N_m^* = molar rate of m-th component leaving or entering the reservoir, $\frac{RB\ .\ lbmol}{RCF\ .\ Day}$

N_o = molar rate of fluids that is produced as condensate on the surface, $\frac{RB\ .\ lbmol}{RCF\ .\ Day}$

N_w = molar rate of water leaving or entering the control volume, lbmol/day

$\widehat{N}_m$ = molar rate of the m-th component at the interface, $\frac{RB\ .\ lbmol}{RCF\ .\ Day}$

$\widehat{N}_w$ = molar rate of water at the interface, $\frac{RB\ .\ lbmol}{RCF\ .\ Day}$

$OCIP$ = Original condensate in place, STB

$OGIP$ = Original gas in place, MSCF

$OHIP$ = Original hydrocarbons in place, lb/mol

p_{cm} = critical pressure of the m-th component, psia

p_i = initial reservoir pressure, psia.

p_g = pressure of the gas phase, psia

p_o = pressure of the condensate phase, psia

p_{sc} = pressure at standard conditions, taken at the pressure of the stock tank, psia

p_w = pressure of the water phase, psia

p_{wf} = wellbore bottomhole pressure, psia

P_c = Capillary pressure, psi

P_{cgo} = gas/oil capillary pressure, psi

P_{cow} = oil/water capillary pressure, psi

$q_{sc,g}$= volumetric rate of gas produced at the surface, MSCF/D

$q_{sc,o}$ = volumetric rate of condensate produced at the surface, STB/D

$q_{sc,w}$ = volumetric rate of water produced at the surface, STB/D

Q_m = rate of external withdrawal/injection of m-th component in the control volume, lbmol/day

Q_w = rate of external withdrawal/injection of water in the control volume, lbmol/day

R = total molar recovery of hydrocarbons or the universal gas constant, $\frac{10.73\ \ psia\ ft^3}{lbmol\ .\ R}$

R_m = molar recovery of the m-th component

R_g = surface gas recovery

R_o= surface condensate recovery

S_g = gas saturation at reservoir conditions

S_o = condensate saturation at reservoir conditions

S_w = water saturation at reservoir conditions

t = time, days

T_{cm} = critical temperature of the m-th component, ^oF or ^oR

T_{gx} = gas transmissibility coefficient on the x-direction

T_{gy} = gas transmissibility coefficient on the y-direction

T_{gz} = gas transmissibility coefficient on the z-direction

T'_{gx} = gas gravity transmissibility coefficient on the x-direction

T'_{gy} = gas gravity transmissibility coefficient on the y-direction

T'_{gz}= gas gravity transmissibility coefficient on the z-direction

T_{ox} = condensate transmissibility coefficient on the x-direction

T_{oy} = condensate transmissibility coefficient on the y-direction

T_{oz} = condensate transmissibility coefficient on the z-direction

T'_{ox} = condensate gravity transmissibility coefficient on the x-direction

T'_{oy} = condensate gravity transmissibility coefficient on the y-direction

T'_{oz} = condensate gravity transmissibility coefficient on the z-direction

T_{pc} = pseudo-critical temperature of the mixture, ^oR

T_{sc} = temperature at standard conditions, taken at the stock tank, ^{o}R

v_{mo} = velocity of the m-th component in the condensate phase averaged over the entire cross sectional area, ft/s

v_{mg} = velocity of the m-th component in the gas phase averaged over the entire cross sectional area, ft/s

$\bar{v}$ = mixture molar volume, ft^3/lbmol

v_g^D = Darcian velocity of the gas phase due to pressure gradients, ft/s

v_o^D = Darcian velocity of the condensate phase due to pressure gradients, ft/s

v_w^D = Darcian velocity of the water phase due to pressure gradients, ft/s

v_{mg}^F = Fickian velocity of the m-th species in the gas phase due to concentration gradients, ft/s

v_{mo}^F = Fickian velocity of the m-th species in the condensate phase due to concentration gradients, ft/s

v_{wg}^F = Fickian velocity of water due to concentration gradients, ft/s

V_b= bulk volume of the grid block ($\Delta x \Delta y \Delta z$), ft^3

V_P = porous volume of the grid block ($\phi \Delta x \Delta y \Delta z$), ft^3

w = width of the typical representative matrix block of a naturally fractured reservoir, ft

x_m = molar composition of the m-th component in the condensate phase

y_m = molar composition of the m-th component in the gas phase

z_m = overall molar composition of the m-th component in the hydrocarbon mixture

Z_{cm} = compressibility factor of the m-th component at the critical point

Greek

α_g= equilibrium vapor molar fraction

α_o= equilibrium condensate molar fraction

ϕ = porosity

φ_m = compositional conversion factor for the m-th component

μ_g= viscosity of the gas phase, cp

μ_o= viscosity of the condensate phase, cp

μ_w = viscosity of the water phase, cp

Ω_{am} = Peng-Robinson attraction parameter constant for the m-th component in the mixture

Ω_{bm} = Peng-Robinson co-volume parameter constant for the m-th component in the mixture

ρ_g = gas mass density, lb/ft^3

ρ_o = condensate mass density, lb/ft^3

ρ_w = water mass density, lb/ft^3

ρ_{wsc} = water mass density at standard conditions, lb/ft^3

$\bar{\rho}_g$ = gas molar density, lbmol/ft^3

$\bar{\rho}_o$ = condensate molar density, lbmol/ft^3

$\bar{\rho}_w$ = water molar density, lbmol/ft^3

Δt = time discretization, days

ω_m = Pitzer's acentric factor of the m-th component

Δx = finite difference space discretization in the x-direction, ft

Δy = finite difference space discretization in the y-direction, ft

Δz = finite difference space discretization in the z-direction, ft

Φ_g = Hubbert's potential of the gas phase, psia

Φ_o = Hubbert's potential of the condensate phase, psia

Φ_w = Hubbert's potential of the water phase, psia

Subscripts

i= running subscript for gridblocks in the x-direction

j= running subscript for gridblocks in the y-direction

k = running subscript for gridblocks in the z-direction

l = running subscript for layers or perforations in a vertical well

m = running subscript for components

g = gas

o = condensate

w = water

s = running subscript for the Cartesian direction (x, y, or z)

f = running subscript for the phase type (o, g, or w)

ACKNOWLEDGEMENTS

The achievement of this project is a result of enormous support of many people who took a great part in helping me attain such accomplishment.

I would like to express my grateful gratitude to my academic advisor, Dr. Luis Ayala for his unlimited support, patient guidance, and valuable friendship throughout my studies here at Pennsylvania State University. My sincere gratitude also goes to the members of the committee, Dr. Robert Watson and Dr. Zuleima Karpyn, whose knowledge and assistance contributed vastly to the success of my research and to my academic achievement.

Special thanks are conveyed to all my friends across the world, colleagues, and classmates for their encouragement, assistance, and joyful times.

My heartfelt gratitude and appreciation is due to my lovely wife, Faten for standing by my side and for the overwhelming love and endless support. Also I would like to express my gratitude to my charming daughter, Jury, for the love she is expressing which awards me with the strength and courage to keep raising the bar higher.

In Addition, I would like to express my deepest sense of gratitude to my beloved family, for their everlasting support, prayers, and encouragement throughout all the stages of my life. I dedicate all my success to my parents, Nasser and Rafiah, my grandmother, Fatima, and to my family members, Abdullah, Bader, Budoor, Boshra, and Abdullaziz.

Chapter 1

INTRODUCTION

Gas-condensate reservoirs are one of the most important sources of hydrocarbons that support the energy of the world. The growth of consumption of natural gas is strongly dependant on the growth of nations and the needs for more applications that are based on sustainable energy (Tusiani and Shearer, 2007). Therefore, a great deal of attention has been paid to the development of natural gas reserves around the world. In the case of gas-condensate reservoirs, their productivity experiences a reduction in recovery due to the appearance of condensate near the wellbore, which in turn reduces the overall flow of hydrocarbons to the surface. With the increase of gas-condensate reservoir occurrences, reservoir researchers had been effectively influenced to scope their studies toward examining the compositional variation of the fluids based on the changes of reservoir conditions during the last decades.

In general, gas-condensate fluids are mixtures of hydrocarbon molecules that are initially present as a gaseous phase at reservoir conditions. During the depletion of the reservoir fluids, the gas condenses as the pressure of the reservoir reduces below the hydrocarbon dew point pressure, which introduces a liquid phase called retrograde condensate. Figure **1.1** shows a typical pressure-temperature phase diagram, where the gas condensate is a single phase fluid at initial condition (p_i). Once the reservoir is put under production, the reservoir pressure depletes isothermally from the initial condition and declines in a downward motion as illustrated by Figure **1.1**. As the pressure crosses the upper dew point pressure (p_{dewUp}), the attraction between the light components and heavy components of the single phase fluid in the reservoir are weakened, which causes a split between the light and heavy components (Ahmed, 2000). The result of the split enhances the attraction between the heavy components and makes it stronger, which results in the formation of a condensate fluid (Ahmed, 2000). The retrograde condensate keeps accumulating until a maximum liquid dropout is reached (L_{max}) as shown in Figure **1.2**. As the pressure continuous to decline beyond the maximum liquid dropout, the retrograde condensate starts to vaporize indicating the transition zone to the vapor region (Ahmed, 2000). More depletion causes the pressure to decrease further until it reaches the lower dew point curve (p_{dewLow}), where the fluids in the reservoir are all in the vapor phase.

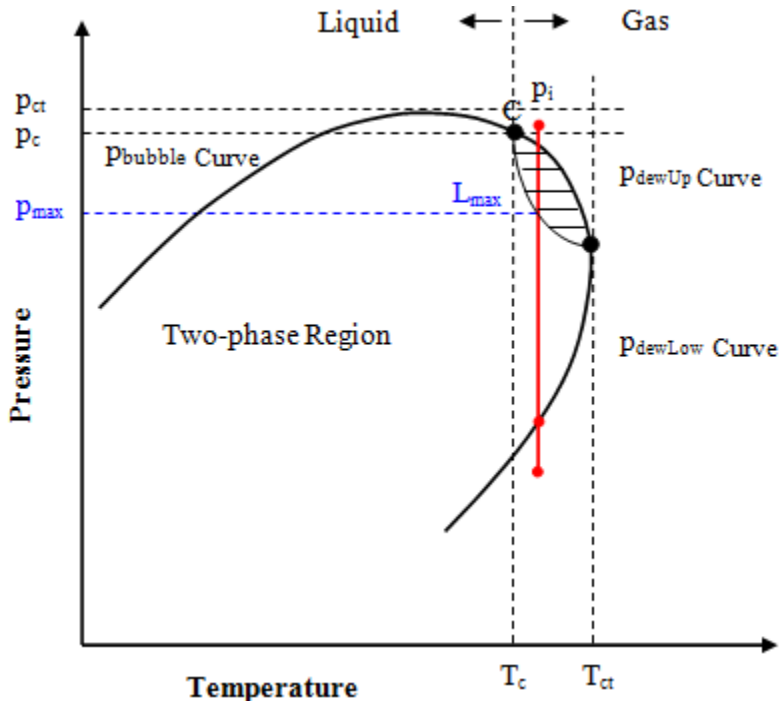

Figure 1.1: A typical phase diagram of a gas-condensate system (*after Ahmed, 2000*)

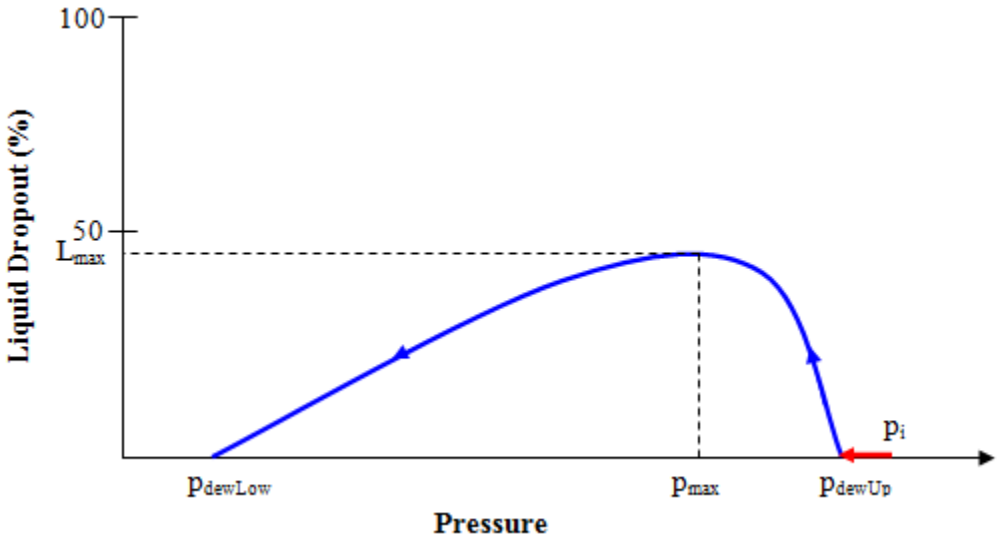

Figure 1.2: A typical liquid dropout diagram

The distribution and deliverability of fluids becomes more effective in naturally fractured reservoirs, where the transport of fluids between the matrix and the fracture depends on the capillary pressure and relative permeability. In nature, naturally fractured reservoirs are presented as complex reservoir systems with non-uniform structures. Ideally, naturally fractured reservoirs are described as group of matrix blocks separated and surrounded by fractures in which the fractures have higher permeability and are interconnected to form flow channels. Once production takes place, the fractured reservoir will experience higher depletion rate compared to conventional matrix blocks. Due to the high depletion at the fractured zones, the reservoir will be prone to faster condensation on the edges of the matrix blocks and in the fracture network. As a result, the condensate will accumulate in these areas and starts to hinder the flow of the gas from the matrix blocks to the wellbore. Therefore, capillary pressure and relative permeability have a great influence on the displacement of fluids in the reservoir and on the overall recovery of fluids in place.

The production scheme of gas-condensate reservoirs impacts the phase behavior of the fluids in place, since the recovery of condensate is highly dependent on the changes in composition. The variation of reservoir fluid properties can be caused by many factors, such as; reservoir pressure, temperature, gravitational forces, and capillary forces. Lee (1989) suggested that the capillary and gravitational forces influence the compositional variation, since the saturation of the gas-condensate systems are controlled by the interfacial forces. In this study, the productivity of naturally fractured gas-condensate reservoirs will be addressed using a compositional simulation model to examine the effect of capillary pressure and relative permeability on the recovery of gas-condensate fluids. The model will be utilized to examine several scenarios of various compositional sets while activating capillary pressure effect to evaluate the productivity of gas-condensate reservoirs.

Chapter 2

BACKGROUND

2.1 Reservoir modeling approaches

Numerical reservoir simulation is a modeling technique heavily used in the development planning of new reservoirs, forecasting the fluid behavior of mature fields, and assessing improvement in hydrocarbon recovery. Reservoir simulation has gone through several developmental stages to come up with numerical models capable of handling large number of computations and maintaining numerical stability.

The evaluation and forecasting of reservoir performance started with the analysis of decline curves and the use of material balance (Fanchi, 2006). Later in time, black oil simulators and compositional simulators came to the picture as more computational capabilities were available. The decline curve analysis basically studies the relationship between production rate and time to forecast the future production potentials. Arps (1945) developed the decline curve analysis to study the production decline behavior by defining three equations, exponential, hyperbolic and harmonic. The analysis concept relies on fitting a line through the production history and assuming the line trend extend into the future. According to Doublet *et al.* (1994), this method utilizes two main variables; the bottom-hole pressure and the production rate, regardless of the reservoir structure or the drive mechanism in the reservoir. The decline curve analysis is very common in studying the performance of wells that lacks sufficient characteristic data, where the only available data are production rates and pressure. Ansah (1996) indicates that almost all research conducted on decline curves analyses are based on enhancing the accuracy of predictions of the work of Arps. Doublet *et al*. (1994) argues that the reason for the wide usage and popularity of the Arps' equations in the industry is for its simplicity and consistency.

Schilthuis (1936) introduced material balance analysis as one of the most powerful tools in the industry, which is capable of providing rich computational approaches to assess the reservoir production forecasting. Kazemi *et al.* (1978) state that the material balance formulations were the foundation that awarded simulation developers with the knowledge to develop multidimensional

simulators. The material balance accounts for material entering or leaving the system and can provides an estimate of mass flows that might not be directly measured. The measurement of the material balance depends on several variables; cumulative field production, reservoir pressure, and fluid properties. However, one of the limitations of this measurement is that it assumes the reservoir behaves as a tank, where the pressure and the rock properties are distributed uniformly at every point. For this reason, the material balance is not applicable for heterogeneous reservoir with complex distribution of properties. Canel *et al.* (1992) highlight that the material balance approach is useful only at the early stages of the reservoir's life when there are less characteristic data for the utilization of a multidimensional simulator.

The advancement in the development of computer application provided the tools for engineers to start the utilization of multidimensional simulators and handle more complex reservoir behaviors. Based on the complexity of the reservoirs' fluid properties, reservoir simulation calculations are classified into two categories: black-oil simulation and compositional simulation. Black-oil simulators are models designed to solve multiphase flow in multidimensional systems, where fluid properties are dependent on pressure and independent on composition. The model consists of a system of non-linear differential equations in terms of pressure and saturation. They are viewed as two-component simulators, which are capable of simulating gas dissolved in the oil phase, and as well as residual oil after the dissolved gas is released below the bubble point pressure. Hepguler and Bard (1997) stress that black-oil simulator only allows for gas to be dissolved into oil and released out of it, but does not accommodate for oil vaporizing into gas phase. This means that the oil and gas phases must maintain a fixed phase composition at all time through the simulation process. Thus, the use of black-oil simulators is constrained by the limitation of addressing the phase transfer and change of composition between gas and oil.

Isothermal depletion in gas-condensate reservoirs introduces an additional level of complexity to the analysis due to the fluid's thermodynamic fluid behavior. In this case, fluid properties are highly dependent on changes of pressure and composition. The thermodynamic fluid behavior is addressed through the joint use of Equations of State (EOS) and compositional material balances which forms what we know today as the compositional simulators. Compositional simulators are capable of appraising the thermodynamic and hydrodynamic behavior of multiphase, multidimensional systems under different reservoir conditions. Kazemi *et al.* (1978) introduced one of the first formulations of multiphase, and multidimensional compositional simulators,

which present the fluid phases as N-component mixtures. Numerically, the compositional simulation computes the compositional changes of the phases of these components using mass conservation and phase equilibrium. With the accuracy of the calculations, compositional simulation provides vast applications for the reservoir engineers to forecast the behavior of complex fluids such as gas-condensates. Therefore, the effect of the capillary forces and relative permeability on the behavior of naturally fractured gas-condensate reservoirs will be examined in this study utilizing a compositional simulator.

2.2 Naturally fractured reservoir

The role of capillary pressure in the distribution of fluids in the reservoir becomes more effective in naturally fractured reservoirs, where the transport of fluids between the matrix and the fracture depends on the capillary pressure. In nature, naturally fractured reservoirs are presented as complex reservoir systems with non-uniform structures. Ideally, naturally fractured reservoirs are group of matrix blocks separated and surrounded by fractures in which the fractures have higher permeability and are interconnected to form flow channels. Figure **2.1** shows the ideal representation of the fractured reservoir in the form of "sugar-cube", which was initiated by Warren and Root (1963). The reason behind using the idealized element is that it can be designed to depict the behavior of the complex system of the fractured reservoir, which eventually brings simplicity for the application of simulation modeling.

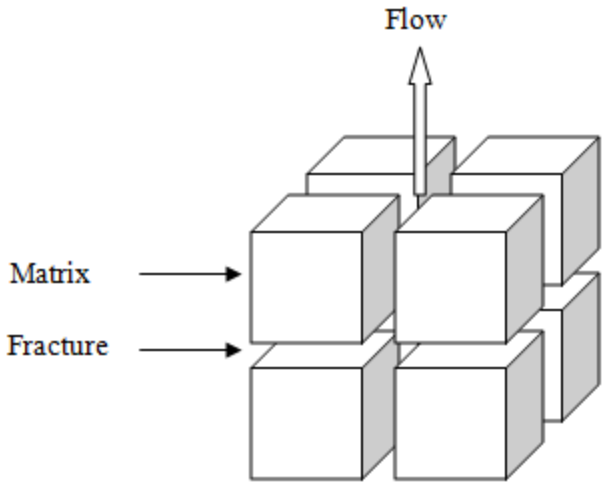

Figure 2.1: Arrangement of matrix blocks and fractures

The matrix blocks contain most of the fluids in place and the flow of these fluids takes place through the fractures network. Gang and Kelkar (2007) indicate that there is no matrix-to-matrix flow, but there is flow from matrix to fracture, because the fractures have higher permeability and they are interconnected with each other to form a flow network to the wellbore.

In gas-condensate reservoirs, most of the gas is stored in the inner of the matrix blocks and once production takes place, the fractured reservoir will experience higher depletion rate compared to conventional matrix blocks. As the depletion occurs, condensate will start to form on the edges of the matrix blocks and in the fracture network. As a result, the condensate will accumulate in these areas and starts to hinder the flow of the gas from the inner of the matrix to the wellbore. Therefore, capillary pressure has a great influence on the displacement of fluids in the reservoir and on the overall recovery of fluids in place.

2.3 Capillary forces effect

The capillary forces are the result of cumulative actions that occur as a consequence of the interfacial tensions between rocks and fluids in a hydrocarbon reservoir, grain sizes and geometry of pore spaces, and the wetting characteristics of the fluids (Ahmed, 2000). For a typical gas-condensate reservoir, the water is the most wetting phase and the condensate is the least wetting phase, while the gas is always considered the non-wetting phase (Fanchi, 2006). Gomes *et al.* (1992) validate that the capillary forces depend on the interfacial tension between oil-water and gas-oil systems, and the geometry and dimensions of the porous network. As two immiscible fluids come in contact with each other, a discontinuity in pressure occurs at the interface resulting in an imbalance forces (Ahmed, 2000). The difference in pressure depends on the curvature separating the two fluids, and is referred to as the capillary pressure. Figure **2.2** illustrates a wetting (*w*) and non-wetting phase (*nw*) in contact with each other, the pressure difference across the interface between p_w and p_{nw} is the capillary pressure as expressed by equation (2.1).

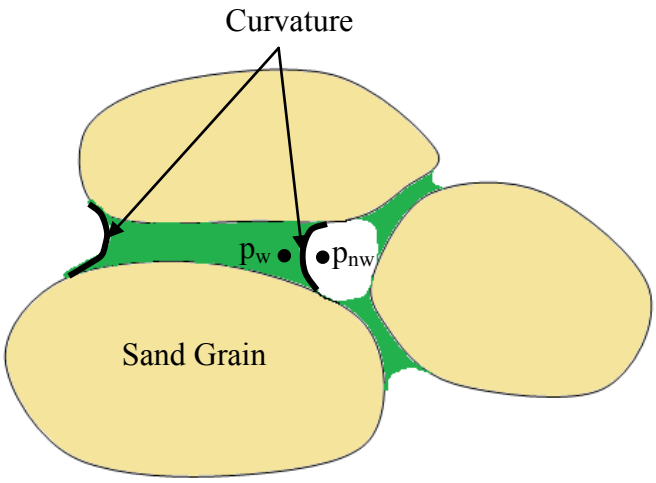

Figure 2.2: Curvature between wetting and non-wetting fluids

Capillary pressure is a function of saturation and it can control the initial distribution of fluids in the pore spaces of a reservoir. Moreover, the role of capillary pressure is highly dependent on the thermodynamic behavioral of the fluids in place, that includes pressure, temperature, and phase compositions. Generally, there are three types of capillary pressure; gas-oil (P_{cgo}), oil-water (P_{cow}), and gas-water (P_{cgw}). For the purpose of this work, gas-condensate capillary pressure effect will be studied while assuming no gas-water capillary pressure effects. Water will be treated as immobile phase at irreducible water saturation, which makes the water saturation and gas-water capillary pressure constants.

Displacement of one fluid by another is controlled by the capillary forces. Ahmed (2000) emphasizes that in order to maintain a porous medium that is exposed to wetting fluid, partially saturated with non-wetting fluid, the pressure of the non-wetting fluid must be greater than the pressure of the wetting fluid. Thus, the capillary relationship between the wetting fluid (p_w) and non-wetting fluid (p_{nw}) can be expressed as shown in equation (2.1), where the capillary pressure is the result of the difference in pressure between the non-wetting and wetting fluids.

$$P_c = p_{nw} - p_w \tag{2.1}$$

The concept of capillary pressure has a great relevance to the initial distribution of fluids in the reservoir. Generally, in reservoirs with multiple mobile phases, water is always the first to occupy the pore spaces with 100% of water saturation before oil and gas immigrates to the aimed reservoir. As soon as oil and gas starts to accumulate at the source rock, the water saturation is reduced to a residual saturation referred to as the connate water saturation. Figure **2.3** represent a typical distribution of fluids in a reservoir with multiple mobile phases, where the capillary pressure-saturation data are interpreted as a function of distance. The figure illustrates the reservoir in terms of pay zones and transition zones. The transition zones are one of the major effects of capillary forces, where there are no sudden changes from 100% water saturation to 100% oil saturation. Similarly, a smooth transition exists between the total liquid saturation (oil, water, or condensate) and the maximum gas saturation. The thickness of the transition zones varies based on the capillary forces, indicating the dependency on the interfacial tensions between rocks and fluids, grain sizes and geometry of pore spaces, and the wetting characteristics of the fluids.

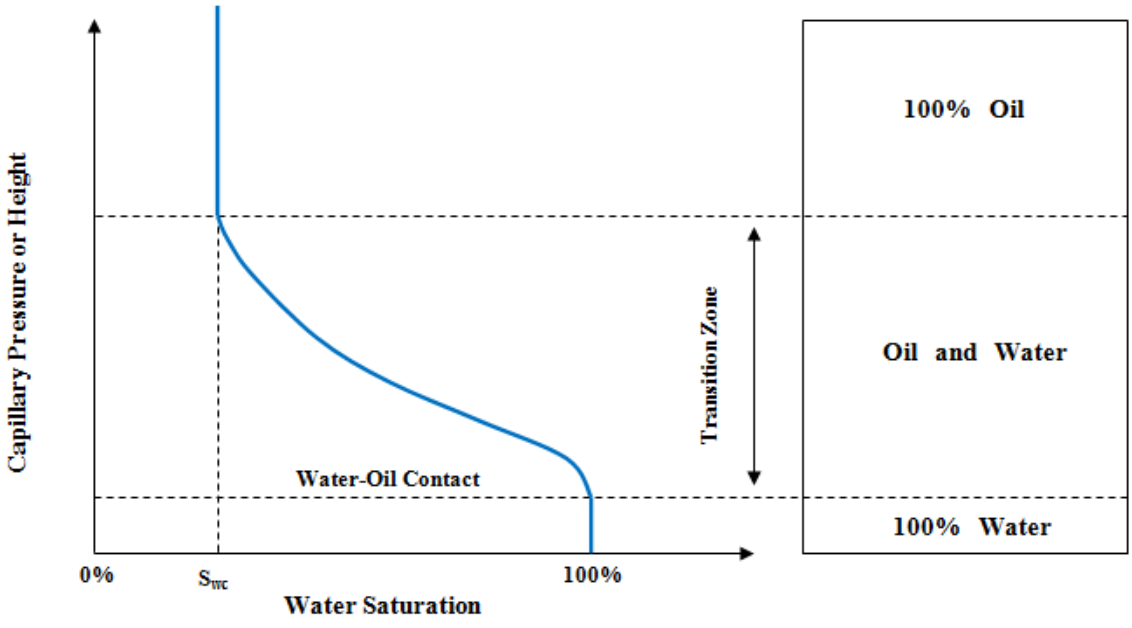

Figure 2.3: A typical water saturation profile

Theoretically, the flow behavior in gas-condensate reservoirs is characterized into three regions once the bottom hole pressure drops below dew point. Figure **2.4**, shows the three regions of the gas-condensate reservoirs; where the first region (R_1) is the region close to the wellbore, the second region (R_2) is the condensate-buildup region, and the third region (R_3) represents the reservoir far from wellbore. The third region exists in gas-condensate reservoirs where the pressure is still higher than the dew point pressure. Due to the pressure condition, the third region contains only gas and is bounded by a boundary condition at which the pressure equals the dew point pressure.

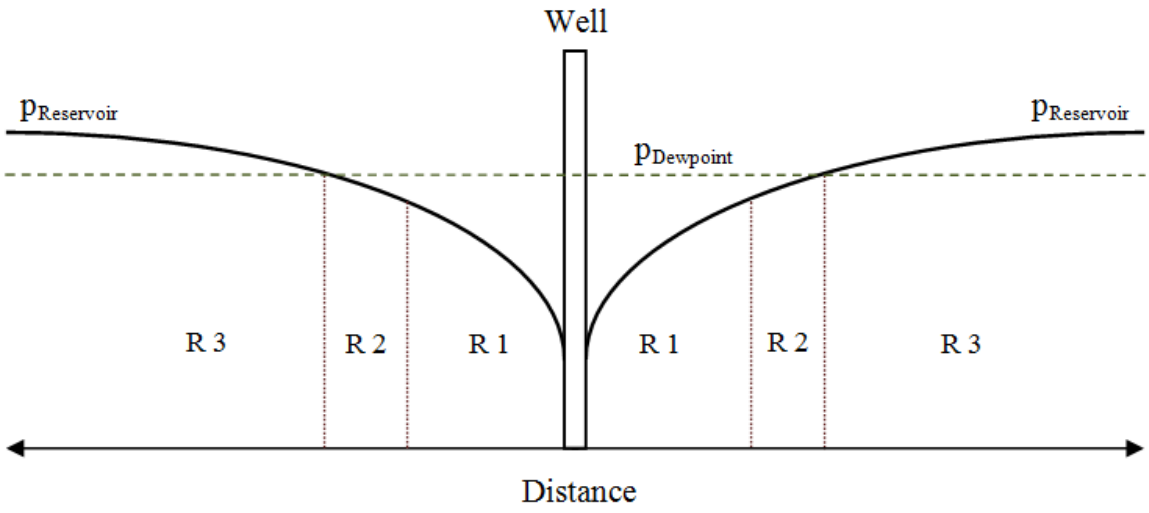

Figure 2.4: A typical three reservoir regions in a gas-condensate system (*after Fan et al., 2005*)

The second region represents the condensate build-up section, where the condensate starts to drop out of the gas. The condensate at this section is immobile because it has low saturation and is trapped by the capillary forces. At this condition, gas keeps flowing while condensate continues to accumulate, occupying pore spaces that were available for the gas flow. Once the critical (residual) condensate saturation is reached, the flow of gas will be hindered by the presence of the condensate in the pore spaces. Meanwhile, the condensate continues to accumulate and the mobility, which is the ratio of relative permeability to the viscosity, starts to be considerable.

The first region represents the reservoir behavior at the wellbore region once the critical condensate saturation is exceeded. Above the critical condensate saturation, the condensate and gas will start to flow and compete for flow paths as illustrated by Figure **2.5**.

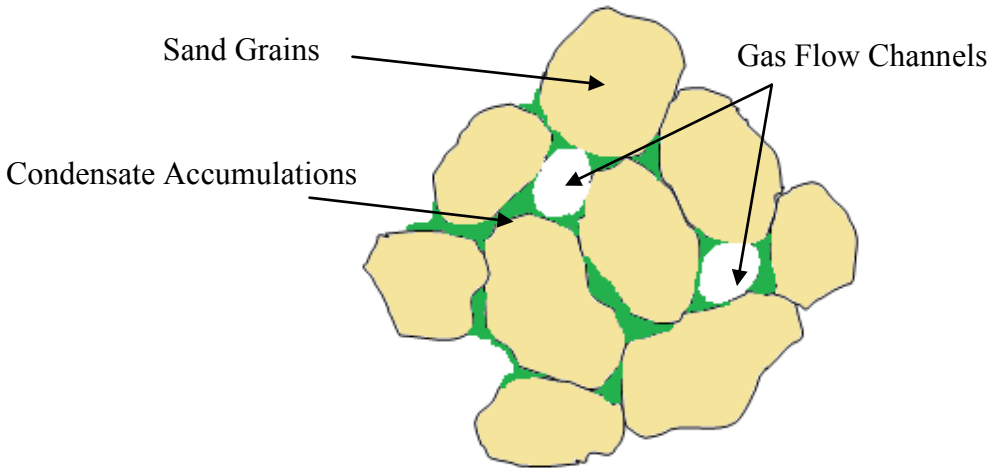

Figure 2.5: Gas-condensate distribution in porous media (*after Fan et al., 2005*)

Unfavorably, the condensate will continue to accumulate until steady-state saturation is reached that is slightly higher than the critical condensate saturation which will cause condensate banking. Bang *et al.* (2006) state that condensate banking can reduce productivity of gas-condensate reservoirs by a factor of 2 to 4. Thus, the deliverability of gas-condensate reservoirs in such conditions is controlled by the transport properties, which are the relative permeabilities and capillary pressures between the fluids in a pore-scale.

Accurate estimation of the capillary pressure distribution is very essential for the prediction of the amount of fluids in place and the distribution pattern in a hydrocarbon reservoir. The magnitude of the capillary forces and the fluid saturation distribution in a reservoir is generally determined through laboratory experiments on core samples. Once results are extracted from the experiment, capillary pressure curves are developed to represent the history profile of the fluid saturations in the reservoir. In most reservoir studies, the capillary curves are utilized to forecast the productivity and behavior of hydrocarbon reservoirs based on the distribution of fluids.

An extensive work has been done throughout the years to develop an empirical correlation that is capable of estimating the capillary pressure curves of hydrocarbon reservoirs. The first developed relation was introduced by Leverett in 1941 after studying a wide range of rock samples. Leverett (1941) developed the J-function as illustrated in equation (2.2). In this equation, Leverett intended to relate the capillary pressure to porosity, interfacial tension, and pore radius, in order to develop a universal capillary curve.

$$J(S_w) = 0.21645 \frac{P_c}{\sigma} \sqrt{\frac{k}{\phi}} \tag{2.2}$$

Few years later, the research was devoted toward relating the pore-scale properties and the fluid characteristics together to get more precise prediction of the capillary pressure behavior. Corey (1954) found a linear relationship between oil and gas capillary pressure curves and developed an expression capable of characterizing the multiphase fluid flow in a reservoir. Equation (2.3a) reflects Corey's equation, where S_w^* is expressed as the normalized wetting phase saturation, S_{wr} as the residual saturation of the wetting phase, and S_{nwi} as the initial saturation of non-wetting phase which is expressed by zero.

$$\frac{1}{P_c^2} = CS_w^* \tag{2.3a}$$

where S_w* is expressed as:

$$S_w^* = \frac{S_w - S_{wr}}{1 - S_{nwi} - S_{wr}} \tag{2.3b}$$

Thomeer (1960) introduced a geometrical factor in his analysis of capillary pressure curves using mercury, in order to classify the capillary pressure curves as functions of pore sizes. A relationship between capillary pressure and mercury saturation was analyzed and a correlation was developed as illustrated in equation (2.4). In the equation, p_e is the entry capillary pressure of the rock, S_{Hg}, is the mercury saturation, $S_{Hg\infty}$ is the mercury saturation at an infinite capillary pressure, and F_g is the pore geometrical factor.

$$P_c = p_e \left(\frac{S_{Hg}}{S_{Hg\infty}} \right)^{\frac{-1}{F_g}} \tag{2.4}$$

Brooks and Corey (1966) carried on the work of Thomeer and modified the capillary pressure function to capture a wide range of geometry classification as shown in equation (2.5). The development of the general form was a result of several conducted analysis on large number of core samples. In Brooks and Corey's equation, λ was introduced to represent the pore size distribution in order to indicate the heterogeneity of the porous medium. According to Gang and Kelkar (2007), the most widely used correlation in the petroleum industry for the prediction of capillary pressure curves is the Brooks-Corey equation.

$$P_c = p_e(S_w^*)^{\frac{-1}{\lambda}} \tag{2.5}$$

Throughout the years, reservoir engineers have always wondered about the vast utilization of Brooks and Corey's model. Li (2004) derived the empirical Brooks-Corey correlation and have found that the theoretical development of the correlation has solid theoretical basis. However, Li and Horne (2003) came across a study of a fractured reservoir, in which the rock samples contained many fractures. The experimental work on the sample using Brooks and Corey's model to represent the capillary pressure curves was not successful due to the high fractal dimension in heterogeneous reservoirs with fractures. The relationship between the fractal dimension and pore size distribution is expressed as shown in equation (2.6). In which, the indication of the heterogeneity relies on the value of the pore size distribution index; the smaller the distribution index, the greater the heterogeneity of the formation and the greater the fractal dimension value will be.

$$\lambda = 3 - D_f \tag{2.6}$$

Despite the findings of Li and Horne (2003), Li (2004) emphasizes that among all the capillary pressure correlation developed, the Brooks-Corey correlation works well for drainage processes in consolidated porous media. The reason the Brooks-Corey correlation is not applicable in imbibitions cases is that the capillary pressure goes to infinity at $1 - S_{wc}$ as shown in Figure **2.6**, which represents the displacement of the wetting phase by the non-wetting phase.

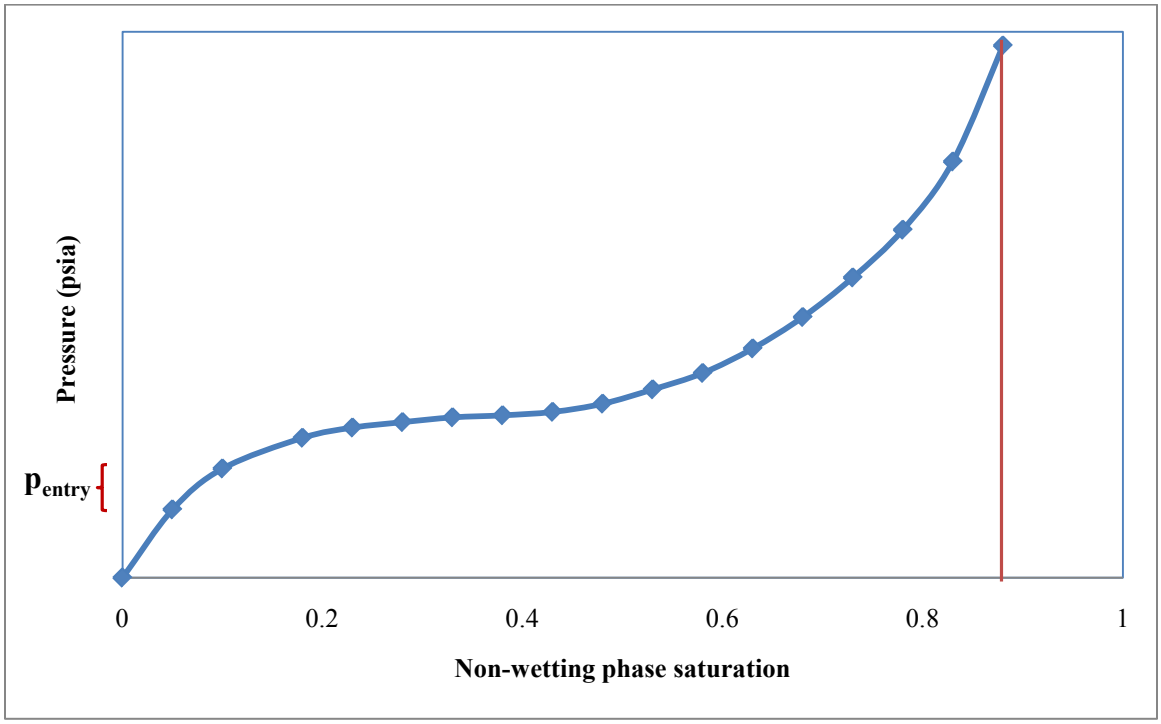

Figure 2.6: A representation of a drainage process

Considering the imbibitions capillary representation, Pooladi-Darvish and Firoozabadi (2000), devoted a great attention toward analyzing the production of oil through imbibitions in fractured water wet matrices. Pooladi-Darvish and Firoozabadi came up with a capillary pressure for imbibitions cases which can be seen in equation (2.7).

$$P_c = - p_{consant} \ln S_w^* \tag{2.7}$$

Four years later, Li (2004) suggested a new capillary pressure model based on the observation and conclusions from his work on the experimental verification of the Brooks-Corey correlation. Li (2004), presented equation (2.8a), where p_{max} represents the capillary pressure at the residual non-wetting phase saturation for the imbibitions case, and represents the capillary pressure at the residual wetting phase saturation for the drainage case.

$$P_c = p_{max} (1 - bS_w^*)^{\frac{-1}{\lambda}} \tag{2.8a}$$

where: $b = 1 - \left(\frac{p_e}{p_{max}}\right)^{-\lambda}$ (2.8b)

2.4 Relative permeability determination

Capillary pressure and relative permeability are the most important parameters in determining the productivity of gas-condensate reservoirs especially as condensate starts to form when the bottom hole pressure falls below the dew point (Mott *et al.*, 2000). The relative permeability can be determined based on the capillary pressure through many ways. One of the general forms of calculating the relative permeability of the wetting and non-wetting phase is the Burdine Model (1953), which was developed to calculate the relative permeabilities using the capillary pressure. The Burdine Model involves two equations represented with a tortuosity factor; the wetting phase relative permeability as shown in equation (2.9a), and the non-wetting phase relative permeability as illustrated by equation (2.10a).

$$k_{rw} = (\lambda_{rw})^2 \frac{\int_0^{S_w} dS_w / (P_c)^2}{\int_0^1 dS_w / (P_c)^2} \tag{2.9a}$$

where: $\lambda_{rw} = \frac{\tau_w(1.0)}{\tau_w(S_w)} = \frac{S_w - S_m}{1 - S_m}$ (2.9b)

and,

$$k_{rnw} = (\lambda_{rnw})^2 \frac{\int_{S_w}^1 dS_w / (P_c)^2}{\int_0^1 dS_w / (P_c)^2} \tag{2.10a}$$

where: $\lambda_{rnw} = \frac{\tau_{nw}(1.0)}{\tau_{nw}(S_w)} = \frac{1 - S_w - S_e}{1 - S_m - S_e}$ (2.10b)

From the equations of Burdine Model, the λ_{rw} and λ_{rnw} are the tortuosity of the wetting and non-wetting phase respectively, the τ_w and τ_{nw} are the tortuosity ratios, and the S_m and S_e are the minimum wetting phase saturation and the equilibrium saturation of the non-wetting phase respectively.

The application of the Burdine Model is utilized in the work of Brook-Corey (1966) and recently in the work of Li (2004). The Brook-Corey (1966) utilized the capillary pressure equation that they developed and derived general representative permeability equations by substituting the capillary pressure equation (2.5) into equation (2.9a) and (2.10a). The wetting and non-wetting equations shown in equations (2.11) and (2.12) were developed based on the Burdine Model with the assumption that $S_e = 0$.

$$k_{rw} = (S_w^*)^{\frac{2+3\lambda}{\lambda}} \tag{2.11}$$

$$k_{rnw} = (1 - S_w^*)^2 \left[1 - (S_w^*)^{\frac{2+\lambda}{\lambda}}\right] \tag{2.12}$$

Recently, Li (2004) introduced a new relative permeability model considering the development carried out by Brooks-Corey and following the same approach of deriving the new sets of equation from the Burdine Model. The wetting and non-wetting relative permeability equations are illustrated by equations (2.13) and (2.14).

$$k_{rw} = \frac{1-(1-bS_w^*)^{\frac{2+\lambda}{\lambda}}}{1-\alpha^{\frac{2+\lambda}{\lambda}}}(S_w^*)^2 \tag{2.13}$$

$$k_{rnw} = \frac{(1-bS_w^*)^{\frac{2+\lambda}{\lambda}} - \alpha^{\frac{2+\lambda}{\lambda}}}{1-\alpha^{\frac{2+\lambda}{\lambda}}}(1 - S_w^*)^2 \tag{2.14}$$

where: $\alpha = \left(\frac{p_e}{p_{max}}\right)^{-\lambda}$ (2.15)

One of the great advantages of Li's equation is that in the representation of homogenous reservoirs, the Li (2004) equations would be reduced and expressed as the Brook-Corey equations (2.11) and (2.12).

The determination of the relative permeability based on the near-well conditions, requires the understanding of the relationship between gas and oil relative permeaiblities. Chopra and Carter (1986) considered in their study the prediction of gas-condensate reservoir performance as condensate starts forming near the well. The study concentrated on providing sufficient evidence on the validity of the assumption that in a two-phase region, the volumetric flow rates ratio equals the ratio of the volume fractions obtain under constant-composition expansion conditions. The study was conducted through the utilization of phase equilibrium concept and material balance equations. Chopra and Carter (1986) concluded with the emphasis that the relationship between gas and oil relative permeabilities illustrated by a ratio is a function of PVT properties and can be expressed as shown in equation (2.16).

$$\frac{k_{rg}}{k_{ro}} = \frac{V_g \mu_g}{V_o \mu_o} \tag{2.16}$$

In the work of Whitson *et al.* (2003), he relates to the work of Chopra and Carter (1986) by indicating that an accurate development of gas-condensate relative permeabilities requires correlating the ratio in equation (2.16) to the capillary number. The near-wellbore region experience gas flowing at high velocity, allowing the viscous forces to be extremely higher than the capillary forces. The ratio of the viscous forces to the capillary forces is referred to as the capillary number. The higher the capillary number, the higher the relative permeability of the gas phase. In the approach of Whitson *et al.* (2003), the modeling of relative permeability curves was achieved through the fitting of steady-state gas-condensate relative permeability data in the form of $k_{rg} = f\left(\frac{k_{rg}}{k_{ro}}\right)$. Three correlations were used for the fitting of the gas-condensate relative permeability data and describing capillary number, Arco's, Chierici's, and Corey's model. Whitson concluded that all three correlations behave identically in describing the behavior of $k_{rg} = f\left(\frac{k_{rg}}{k_{ro}}\right)$ and that the capillary number should be related to the development of gas-condensate relative permeabilities through the expression described by equation (2.17a).

$$N_c = \frac{V_{pg}\,\mu_g}{\sigma_{go}} \tag{2.17a}$$

where: $V_{pg} = \frac{V_g}{\phi.(1-S_{wi})}$ (2.17b)

In the present study, a great attention will be devoted toward assessing the impact of capillary forces and relative permeability effect on the hydrocarbon behavior and productivity of a fractured gas-condensate reservoir using a fully-implicit compositional simulator. The work will include different sets of capillary profile and relative permeability curves in order to evaluate the influence on the behavior and displacement of the fluids in the reservoir upon isothermal depletion.

Chapter 3

PROBLEM STATEMENT

Gas-condensate fluids are mixtures of hydrocarbon that are initially present as a gaseous phase at initial conditions of discovery. During the depletion of the reservoirs, the gas condenses as the pressure of the reservoir reduces below the hydrocarbon dew point pressure, which introduces a liquid phase called retrograde condensate. The productivity in the gas-condensate reservoirs experience a reduction in recovery due to the appearance of condensate near the wellbore, which in turn reduces the overall flow of hydrocarbons to the surface.

In this study, the productivity of naturally fractured gas-condensate reservoirs will be addressed using a compositional simulation model to examine the effect of capillary pressure and relative permeability on the recovery of gas-condensate fluids. Capillary pressure is a function of saturation and it controls the distribution of fluids in the pore spaces of a reservoir. The role of capillary pressure in the distribution of fluids in the reservoir becomes more effective in naturally fractured reservoirs, where the transport of fluids between the matrix and the fracture depends on the capillary pressure and relative permeability.

In fractured gas-condensate reservoirs, most of the gas is stored in the inner of matrix blocks and once production takes place, the fractured reservoir will experience higher depletion rate compared to conventional matrix blocks. As the depletion occurs, condensate will start to form on the edges of the matrix blocks and as a result will hinder the flow of the gas from the inner of the matrix to the wellbore. Therefore, capillary pressure has a great influence on the displacement of fluids in the reservoir and on the overall recovery of fluids in place. Thus, this study will be devoted to evaluate the growth of condensate coating by examining different compositions (light/heavy) with the activation of the capillary pressure effects, while keeping the depletion rate constant, and deactivating the diffusion effect in the system.

Chapter 4

MODEL FORMULATION

Compositional simulators are aimed at simplifying the prediction of thermodynamic behavior and productivity upon process such as gas injection and gas cycling into volatile oil or retrograde gas-condensate reservoirs. They are used to study recovery schemes for reservoirs where the behavior of fluids are highly dependent on pressure and composition. The built-in model of such simulators accounts for three dimensional and three-phase flow in a gas condensate reservoir with the presence of gravitational and capillary forces. The formulation of the model is accommodated with the governing equation which includes; partial differential equations, Equation of State for phase equilibrium relations, and the constraint equations which include unity of saturations and mole fractions of components.

The compositional model used for the purpose of this study was built to account for one water phase and two hydrocarbon phases, gas and condensate, that consists of N-components. The flow equations for the phases are discretized in a fully-implicit finite difference form, where the primary unknowns are solved simultaneously. The non-linear equations developed as a result of the finite difference equations are solved using Newton-Raphson approach, which solves the nonlinear equations through an iterative technique used to direct the solution to a specified tolerance.

The general form of the governing differential equations used in the model, where hydrocarbon fluid components are found both in the liquid and gas phases, were derived from the substitution of a velocity model responsible for the flow of fluids within the system into the continuity equation. The continuity equation can be derived by selecting control volume (CV) at which the fluids are flowing through each of its faces, and writing the molar-balance over the specified volume. Figure **4.1**, illustrates a rectangular coordinates hosting a rectangular flow system flowing through the six faces of the control volume (CV).

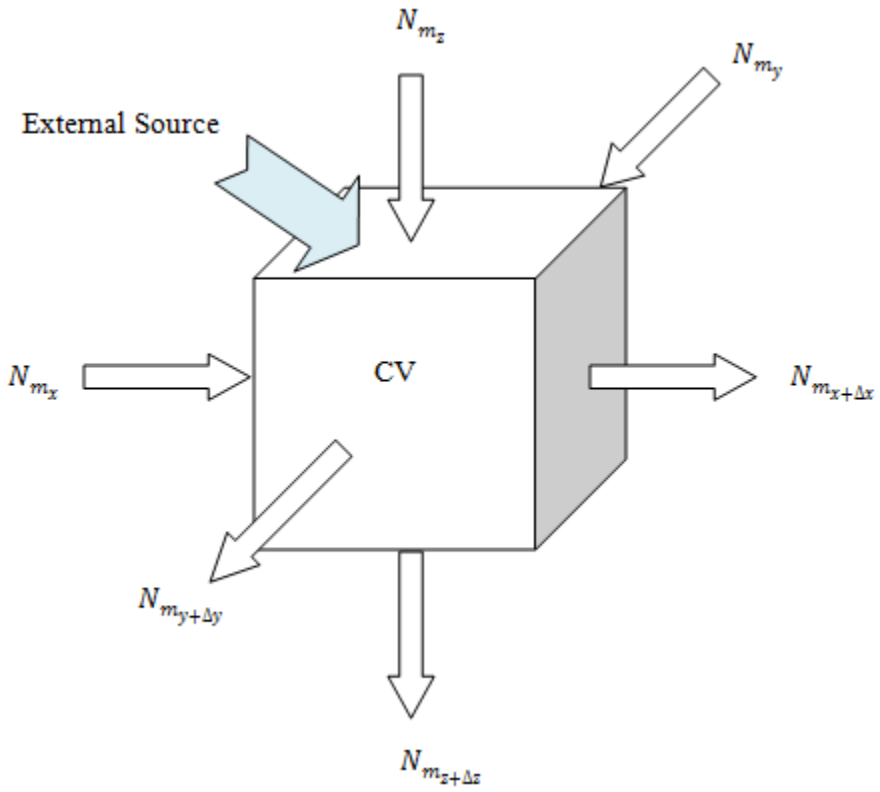

Figure 4.1: Rectangular control volume illustration

Considering the previous illustration of the control volume, the molar-balance of the continuity equation of each *m-th* component entering or leaving the system can be expresses over time (Δt) in the form of:

(Moles entering CV – Moles leaving CV) + Molar external source = Accumulation

… (4.1)

In order to obtain a mathematical representation of equation (4.1), the following representations are considered:

Moles of m-components IN = $(N_{m_x} + N_{m_y} + N_{m_z})\Delta t$ (4.2a)

Moles of m-components OUT = $(N_{m_{x+\Delta x}} + N_{m_{y+\Delta y}} + N_{m_{z+\Delta z}})\Delta t$ (4.2b)

Accumulation = $(\Delta x \Delta y \Delta z \phi(\mathrm{S_o x_m \bar{\rho}_o} + \mathrm{S_g y_m \bar{\rho}_g}))_{t+\Delta t} - (\Delta x \Delta y \Delta z \phi(\mathrm{S_o x_m \bar{\rho}_o} + \mathrm{S_g y_m \bar{\rho}_g}))_t$

… (4.2c)

Considering that the molar flow rate (N_m) in the previous illustration is a contribution of the flow rate of the components in the condensate and gas phase, equation (4.1) can be expressed as the following while dividing by (Δt) and assigning positive (+) sign to flow going into the system and negative (-) for flow leaving the system:

$$-\left[\left(N_{mo}+N_{mg}\right)_{x+\Delta x}-\left(N_{mo}+N_{mg}\right)_{x}\right]-\left[\left(N_{mo}+N_{mg}\right)_{y+\Delta y}-\left(N_{mo}+N_{mg}\right)_{y}\right]-\left[\left(N_{mo}+N_{mg}\right)_{z+\Delta z}-\left(N_{mo}+N_{mg}\right)_{z}\right]+Q_m=\Delta x\Delta y\Delta z\frac{\left[\phi(\mathrm{S_o x_m}\bar{\rho}_{\mathrm{o}}+\mathrm{S_g y_m}\bar{\rho}_{\mathrm{g}})\right]_{t+\Delta t}-\left[\phi(\mathrm{S_o x_m}\bar{\rho}_{\mathrm{o}}+\mathrm{S_g y_m}\bar{\rho}_{\mathrm{g}})\right]_{t}}{\Delta t} \quad \ldots (4.3)$$

The expression of (4.3) can be expanded by expressing the molar flow rate through each face of the control volume (x, y, and z) as a function of the phase movement velocity, the fraction of the molar density of the phase, and the area perpendicular to the flow direction. The expression can be re-constructed to give the following form:

$$-\left[\left(\mathrm{x_m}\rho_{\mathrm{o}}v_{mox}A_x+\mathrm{y_m}\rho_{\mathrm{g}}v_{mgx}A_x\right)_{x+\Delta x}-\left(\mathrm{x_m}\rho_{\mathrm{o}}v_{mox}A_x+\mathrm{y_m}\rho_{\mathrm{g}}v_{mgx}A_x\right)_{x}\right]-\left[\left(\mathrm{x_m}\rho_{\mathrm{o}}v_{moy}A_y+\mathrm{y_m}\rho_{\mathrm{g}}v_{mgy}A_y\right)_{y+\Delta y}-\left(\mathrm{x_m}\rho_{\mathrm{o}}v_{moy}A_y+\mathrm{y_m}\rho_{\mathrm{g}}v_{mgy}A_y\right)_{y}\right]-\left[\left(\mathrm{x_m}\rho_{\mathrm{o}}v_{moz}A_z+\mathrm{y_m}\rho_{\mathrm{g}}v_{mgz}A_z\right)_{z+\Delta z}-\left(\mathrm{x_m}\rho_{\mathrm{o}}v_{moz}A_z+\mathrm{y_m}\rho_{\mathrm{g}}v_{mgz}A_z\right)_{z}\right]+Q_m=\Delta x\Delta y\Delta z\frac{\left[\phi(\mathrm{S_o x_m}\bar{\rho}_{\mathrm{o}}+\mathrm{S_g y_m}\bar{\rho}_{\mathrm{g}})\right]_{t+\Delta t}-\left[\phi(\mathrm{S_o x_m}\bar{\rho}_{\mathrm{o}}+\mathrm{S_g y_m}\bar{\rho}_{\mathrm{g}})\right]_{t}}{\Delta t} \quad \ldots (4.4)$$

By dividing equation (4.4) by the bulk volume ($V_b=\Delta x\Delta y\Delta z$), the following expression is obtained:

$$-\frac{\left[\left(\mathrm{x_m}\rho_o v_{mox} + \mathrm{y_m}\rho_g v_{mgx}\right)_{x+\Delta x} - \left(\mathrm{x_m}\rho_o v_{mox} + \mathrm{y_m}\rho_g v_{mgx}\right)_x\right]}{\Delta x}$$

$$-\frac{\left[\left(\mathrm{x_m}\rho_o v_{moy} + \mathrm{y_m}\rho_g v_{mgy}\right)_{y+\Delta y} - \left(\mathrm{x_m}\rho_o v_{moy} + \mathrm{y_m}\rho_g v_{mgy}\right)_y\right]}{\Delta y}$$

$$-\frac{\left[\left(\mathrm{x_m}\rho_o v_{moz} + \mathrm{y_m}\rho_g v_{mgz}\right)_{z+\Delta z} - \left(\mathrm{x_m}\rho_o v_{moz} + \mathrm{y_m}\rho_g v_{mgz}\right)_z\right]}{\Delta z} + \frac{Q_m}{V_b}$$

$$= \frac{\left[\phi(\mathrm{S_o x_m}\bar{\rho}_o + \mathrm{S_g y_m}\bar{\rho}_g)\right]_{t+\Delta t} - \left[\phi(\mathrm{S_o x_m}\bar{\rho}_o + \mathrm{S_g y_m}\bar{\rho}_g)\right]_t}{\Delta t} \quad \ldots (4.5)$$

In order to write equation (4.5) in the differential form, the limits of Δx, Δy, Δz, and Δt need to be taken in for form of $\lim_{\Delta s\to 0}\{Left\ hand\ side\} = \lim_{\Delta s\to 0}\{Left\ hand\ side\}$. While recalling that $\lim_{\Delta s\to 0}\frac{f(s+\Delta s)-f(s)}{\Delta s} = \frac{\partial f}{\partial s}$, the previous expression can be re-written in the differential form as shown below:

$$-\frac{\partial}{\partial x}\left(\mathrm{x_m}\bar{\rho}_o v_{mox} + \mathrm{y_m}\bar{\rho}_g v_{mgx}\right) - \frac{\partial}{\partial y}\left(\mathrm{x_m}\bar{\rho}_o v_{moy} + \mathrm{y_m}\bar{\rho}_g v_{mgy}\right)$$

$$-\frac{\partial}{\partial z}\left(\mathrm{x_m}\bar{\rho}_o v_{moz} + \mathrm{y_m}\bar{\rho}_g v_{mgz}\right) + \frac{Q_m}{V_b} = \frac{\partial}{\partial t}\left[\phi(\mathrm{S_o x_m}\bar{\rho}_o + \mathrm{S_g y_m}\bar{\rho}_g)\right] \quad (4.6)$$

In order to express continuity equation for variable flow area, equation (4.6) need to be multiplied by the bulk volume which would give the following representation of the continuity equation used in this model:

$$-\frac{\partial}{\partial x}\left(\mathrm{x_m}\bar{\rho}_o v_{mox} A_x + \mathrm{y_m}\bar{\rho}_g v_{mgx} A_x\right) - \frac{\partial}{\partial y}\left(\mathrm{x_m}\bar{\rho}_o v_{moy} A_y + \mathrm{y_m}\bar{\rho}_g v_{mgy} A_y\right)$$

$$-\frac{\partial}{\partial z}\left(\mathrm{x_m}\bar{\rho}_o v_{moz} A_z + \mathrm{y_m}\bar{\rho}_g v_{mgz} A_z\right) + Q_m = V_b\frac{\partial}{\partial t}\left[\phi(\mathrm{S_o x_m}\bar{\rho}_o + \mathrm{S_g y_m}\bar{\rho}_g)\right] \quad (4.7)$$

To come up with the governing differential equation of hydrocarbon, a suitable velocity model needs to be substituted in the molar velocity terms of equation (4.7) to represent the flow of fluids within the system. The model used for this work, which was developed by Ayala (2006), was built to accommodate a multi-mechanistic flow. In other words, the model is capable of considering different flow potentials which are responsible of the flow in the system.

The concept of the multi-mechanistic flow was introduced by Ertekin *et al.* (1986), which emphasizes that the fluid flow within the system is driven by the concentration or density gradients denoted as diffusion and the bulk velocity which is influenced by the pressure gradient. Thus, the total molar velocity is a result of the flow driven by the bulk Darcian effect (v_{fs}^{D}) added to the flow caused by the Flickian component (v_{mfs}^{F}) as illustrated in equations (4.8a) and (4.8b).

$$v_{mos} = v_{os}^{D} + v_{mos}^{F} \quad ; \quad s = x, y, \text{ and } z \qquad (4.8a)$$

$$v_{mgs} = v_{gs}^{D} + v_{mgs}^{F} \quad ; \quad s = x, y, \text{ and } z \qquad (4.8b)$$

According to Ayala (2006), the diffusion effect in the liquid phase is less significant than in the gas phase, which makes the diffusion forces in the condensate negligible as indicated in equations (4.9a) and (4.9b).

$$v_{mos} = v_{os}^{D} \quad ; \quad s = x, y, \text{ and } z \qquad (4.9a)$$

$$v_{mgs} = v_{gs}^{D} + v_{gs}^{F} \quad ; \quad s = x, y, \text{ and } z \qquad (4.9b)$$

where: $v_{fs}^{D} = -5.615 \frac{k_s k_{rf}}{\mu_f} \frac{\partial \Phi_f}{\partial s}$; $f = o$, or g , $s = x$, y, and z (4.9c)

and, $v_{gs}^{F} = -\phi S_g \frac{D_{eff}}{\rho_g} \frac{\partial \rho_g}{\partial s}$; $s = x, y, \text{ and } z$ (4.9d)

By substituting the velocity terms in the continuity equation (4.7) and dividing the whole term by 5.615 to adjust the units to (RB/day)(lbmole/RCF), we get the following differential material balance equation:

$$\begin{aligned}
&\frac{\partial}{\partial x}\left(x_m \bar{\rho}_o A_x \frac{k_x k_{ro}}{\mu_o}\frac{\partial \Phi_o}{\partial x} + y_m \bar{\rho}_g A_x \frac{k_x k_{rg}}{\mu_g}\frac{\partial \Phi_g}{\partial x} + y_m \phi S_g A_x \frac{D_{eff}}{5.615}\frac{\partial \bar{\rho}_g}{\partial x}\right)\Delta x \\
&+\frac{\partial}{\partial y}\left(x_m \bar{\rho}_o A_y \frac{k_y k_{ro}}{\mu_o}\frac{\partial \Phi_o}{\partial y} + y_m \bar{\rho}_g A_y \frac{k_y k_{rg}}{\mu_g}\frac{\partial \Phi_g}{\partial y} + y_m \phi S_g A_y \frac{D_{eff}}{5.615}\frac{\partial \bar{\rho}_g}{\partial y}\right)\Delta y \\
&+\frac{\partial}{\partial z}\left(x_m \bar{\rho}_o A_z \frac{k_z k_{ro}}{\mu_o}\frac{\partial \Phi_o}{\partial z} + y_m \bar{\rho}_g A_z \frac{k_z k_{rg}}{\mu_g}\frac{\partial \Phi_g}{\partial z} + y_m \phi S_g A_z \frac{D_{eff}}{5.615}\frac{\partial \bar{\rho}_g}{\partial z}\right)\Delta z \\
&+M_m = \frac{V_b}{5.615}\frac{\partial}{\partial t}\left[\phi\left(S_o x_m \bar{\rho}_o + S_g y_m \bar{\rho}_g\right)\right] \quad ; \quad m = 1, 2, \ldots, n_c
\end{aligned} \qquad \ldots (4.10a)$$

where: $M_m = \frac{Q_m}{5.615}$ (4.10b)

and, $\frac{\partial \Phi_f}{\partial s} = \frac{\partial p_f}{\partial s} - \frac{1}{144}\frac{g}{g_c}\rho_f \frac{\partial G}{\partial s}$; $f = o, or\ g$, $s = x, y, and\ z$ (4.10c)

Re-arranging equation (4.10a), leads to the final representation of the governing differential equations used in the model, which was presented in the work of Ayala (2006).

$$\frac{\partial}{\partial x}\left(x_m \bar{\rho}_o A_x \frac{k_x k_{ro}}{\mu_o}\frac{\partial p_o}{\partial x} + y_m \bar{\rho}_g A_x \frac{k_x k_{rg}}{\mu_g}\frac{\partial p_g}{\partial x} + y_m \phi S_g A_x \frac{D_{eff}}{5.615}\frac{\partial \bar{\rho}_g}{\partial x}\right)\Delta x$$
$$-\frac{\partial}{\partial x}\left(\frac{1}{144}\frac{g}{g_c}\rho_o x_m \bar{\rho}_o A_x \frac{k_x k_{ro}}{\mu_o}\frac{\partial G}{\partial x} + \frac{1}{144}\frac{g}{g_c}\rho_g y_m \bar{\rho}_g A_x \frac{k_x k_{rg}}{\mu_g}\frac{\partial G}{\partial x}\right)\Delta x$$
$$+\frac{\partial}{\partial y}\left(x_m \bar{\rho}_o A_y \frac{k_y k_{ro}}{\mu_o}\frac{\partial p_o}{\partial y} + y_m \bar{\rho}_g A_y \frac{k_y k_{rg}}{\mu_g}\frac{\partial p_g}{\partial y} + y_m \phi S_g A_y \frac{D_{eff}}{5.615}\frac{\partial \bar{\rho}_g}{\partial y}\right)\Delta y$$
$$-\frac{\partial}{\partial y}\left(\frac{1}{144}\frac{g}{g_c}\rho_o x_m \bar{\rho}_o A_y \frac{k_y k_{ro}}{\mu_o}\frac{\partial G}{\partial y} + \frac{1}{144}\frac{g}{g_c}\rho_g y_m \bar{\rho}_g A_y \frac{k_y k_{rg}}{\mu_g}\frac{\partial G}{\partial y}\right)\Delta y$$
$$+\frac{\partial}{\partial z}\left(x_m \bar{\rho}_o A_z \frac{k_z k_{ro}}{\mu_o}\frac{\partial p_o}{\partial z} + y_m \bar{\rho}_g A_z \frac{k_z k_{rg}}{\mu_g}\frac{\partial p_g}{\partial z} + y_m \phi S_g A_z \frac{D_{eff}}{5.615}\frac{\partial \bar{\rho}_g}{\partial z}\right)\Delta z$$
$$-\frac{\partial}{\partial y}\left(\frac{1}{144}\frac{g}{g_c}\rho_o x_m \bar{\rho}_o A_z \frac{k_z k_{ro}}{\mu_o}\frac{\partial G}{\partial z} + \frac{1}{144}\frac{g}{g_c}\rho_g y_m \bar{\rho}_g A_z \frac{k_z k_{rg}}{\mu_g}\frac{\partial G}{\partial z}\right)\Delta z$$
$$+M_m = \frac{V_b}{5.615}\frac{\partial}{\partial t}\left[\phi\left(S_o x_m \bar{\rho}_o + S_g y_m \bar{\rho}_g\right)\right]; \qquad m = 1, 2, \ldots, n_c \tag{4.11}$$

In this work, the porous medium is considered to be wetted by water and condensate. In addition, there are neither hydrocarbons dissolved in the water phase nor water can be found in solution with hydrocarbon phases which means that the interfacial diffusion effect are eliminated. Thus, since the water is not reacting with the hydrocarbon and the diffusion phenomenon is insignificant in the liquid phase, water is treated as a mobile phase at which the flow is only driven by Darcy's law. Equation (4.12) represents the flow equation of water in the form of partial differential. The details of the derivation of the water equation and its assumptions are found in Appendix A.

$$\frac{\partial}{\partial x}\left(\frac{A_x k_x k_{rw}}{\beta_w \mu_w}\frac{\partial p_w}{\partial x} - \frac{1}{144}\frac{g}{g_c}\rho_o \frac{A_x k_x k_{rw}}{\beta_w \mu_w}\frac{\partial G}{\partial x}\right)\Delta x + \frac{\partial}{\partial y}\left(\frac{A_y k_y k_{rw}}{\beta_w \mu_w}\frac{\partial p_w}{\partial y} - \frac{1}{144}\frac{g}{g_c}\rho_o \frac{A_y k_y k_{rw}}{\beta_w \mu_w}\frac{\partial G}{\partial y}\right)\Delta y$$
$$+ \frac{\partial}{\partial z}\left(\frac{A_z k_z k_{rw}}{\beta_w \mu_w}\frac{\partial p_w}{\partial z} - \frac{1}{144}\frac{g}{g_c}\rho_o \frac{A_z k_z k_{rw}}{\beta_w \mu_w}\frac{\partial G}{\partial z}\right)\Delta z + q_{sc,w}$$
$$= \frac{V_b}{5.615}\frac{\partial}{\partial t}\left[\frac{\phi\, S_w}{\beta_w}\right] \qquad (4.12)$$

The model is represented with $3n_c$+6 unknowns and $3n_c$+6 equations listed in Table **4.1**. Moreover, all the other variables of the equations are calculated as a function of the dependent variables.

Table 4.1: Inventory of equations and unknowns

Inventory of Unknowns	
Fluid Pressures	p_o, p_g, p_w
Fluid Saturations	S_o, S_g, S_w
Overall Composition	z_m *(m=1, 2, 3, …, n_c)*
Condensate Composition	x_m *(m=1, 2, 3, …, n_c)*
Gas Composition	y_m *(m=1, 2, 3, …, n_c)*
Total	*$3n_c$+6 unknowns*

Inventory of Equations	
Differential molar balances (4.11)	*nc-equations*
Water material balance (4.12)	*1 equation*
Condensate Equilibrium Equations (4.16)	*nc-equations*
Gas equilibrium equations (4.17)	*nc-equations*
Vapor fraction/saturation relationship (4.19)	*1 equation*
Saturation constraint (4.20)	*1 equation*
Capillary pressure relationships (4.23 & 4.24)	*2 equation*
Overall composition constraint (4.15)	*1 equation*
Total	*$3n_c$+6 equations*

In order to simplify the calculation of the given equations, the number of unknowns is reduced and the eliminated variables are calculated after the principle unknowns are computed. For this work, the principle unknowns are considered to be the overall molar composition (z_m), gas phase pressure (p_g), and the water phase saturation (S_w).

Since there are no reaction between water and the hydrocarbon phases, the thermodynamic equilibrium is assumed to be reached instantaneously at any point and time in the reservoir. The equilibrium of vapor molar fraction of the reservoir mixture (α_g) and the vapor-liquid equilibrium ratio (K_m) of each component is reached through flash calculations at any given pressure (p_g), overall composition (z_m), and reservoir temperature. The thermodynamic equilibrium is set to be reached once the following constraints are met:

$$K_m = \frac{y_m}{x_m} \quad ; \quad m=1, 2, \ldots, n_c \tag{4.13}$$

$$z_m = y_m \alpha_g + x_m (1 - \alpha_g) \quad ; \quad m=1, 2, \ldots, n_c \tag{4.14}$$

$$\sum_{m=1}^{n_c} z_m = 1 \tag{4.15}$$

$$x_m = \varphi_m z_m \quad ; \quad m=1, 2, \ldots, n_c \tag{4.16}$$

$$y_m = \varphi_m K_m z_m \quad ; \quad m=1, 2, \ldots, n_c \tag{4.17}$$

$$\varphi_m = (\alpha_g K_m - \alpha_g + 1)^{-1} \tag{4.18}$$

where vapor molar function is:

$$\alpha_g = \frac{\bar{\rho}_g S_g}{\bar{\rho}_o S_o + \bar{\rho}_g S_g} \tag{4.19}$$

Meanwhile, for the definition of gas saturation, the following constraints were considered:

$$S_o + S_w + S_g = 1 \tag{4.20}$$

$$\text{Thus, } S_g = 1 - S_o - S_w \tag{4.21}$$

$$\text{Where } S_o = \frac{\bar{\rho}_g (1-\alpha_g)}{\bar{\rho}_o \alpha_g + \bar{\rho}_g (1-\alpha_g)} (1 - S_w) \tag{4.22}$$

Assuming that the water and condensate are the wetting phases in the reservoir, the capillary pressures are used to calculated the water and oil pressures as a function of the phase satruations.

$$P_{cgo}(S_g) = p_g - p_o \tag{4.23}$$

$$P_{cow}(S_w) = p_o - p_w \tag{4.24}$$

Thus,

$$p_o = p_g - P_{cgo}(S_g) \tag{4.25}$$

$$p_w = p_o - P_{cow}(S_w) = \left[p_g - P_{cgo}(S_g)\right] - P_{cow}(S_w) \tag{4.26}$$

At this stage, all the equations and constraints are defined and presented in a non-linear form that requires a special iterative procedure to be solved. Before using the iterative technique, the non-linear equations developed earlier will be replaced with finite differences approximation derived from Taylor's series as shown in Appendix B. The development of the finite differences approximation will lead to the final representation of the governing equations, which is represented in the form of the molar flows at the interfaces of the elemental volume described in Figure 4.1.

In this model, the equations are discretized in a fully-implicit finite difference form, where the principle unknowns (z_m , p_g and S_w) are solved simultaneously using Newton-Raphson procedure. The gas pressure (p_g) and overall composition (z_m) are calculated at each block of the reservoir through flash calculations, which yield to equilibrium molar vapor fraction (α_g) and the vapor-liquid equilibrium ratios (K_m). The results of the flash calculations are then carried to calculate the condensate compositions and the gas compositions for each component, as shown in equations (4.16) and (4.17), which also yield to the calculations of molar densities and viscosities. Using the fluid properties, the molar vapor fraction, and the water saturation; the oil saturation can be calculated with equation (4.22). The thermodynamic equilibrium requires that condensate and gas saturation should be related, thus, the gas saturation is calculated using the general saturation constraint as shown in equation (4.21). Finally, with the utilization of the capillary pressure equations, the condensate and water pressure are calculated using equations (4.25) and (4.26) respectively.

The fully-implicit technique allows all the primary unknowns to be calculated at the same time step, and update the solution using the iterative procedure until convergence is achieved, refer to Figure **4.2**. Once the specified tolerance is met, all the values are updated and can be carried out to the next time step.

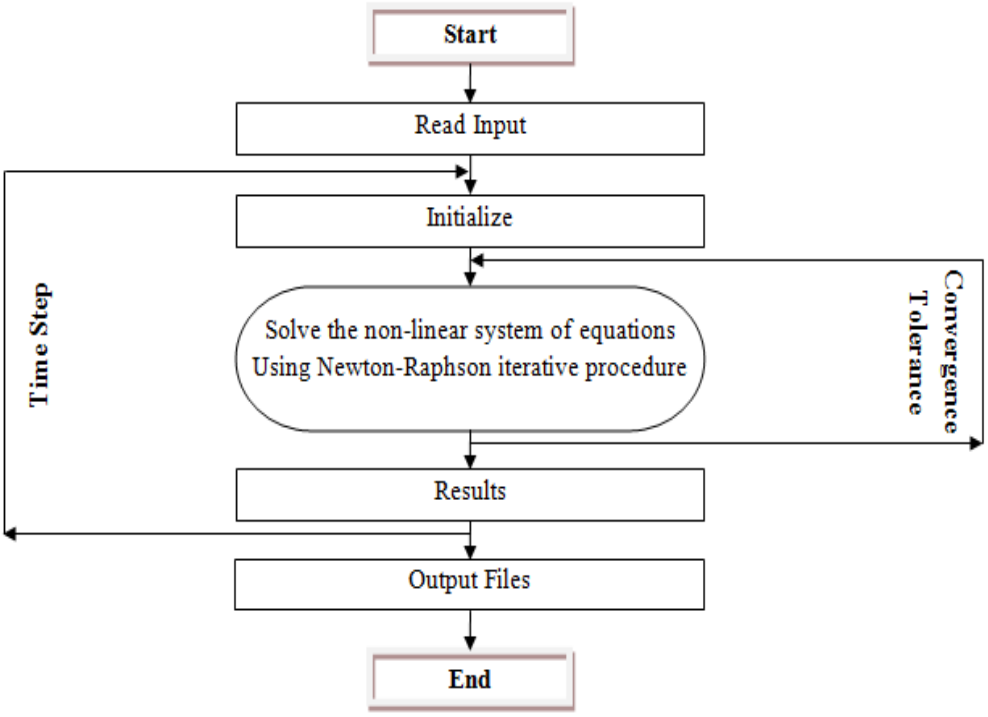

Figure 4.2: A typical fully-implicit simulator flow chart

Solution techniques for non-linear equations are available in different forms, but these techniques depend on many factors; such as computational expenses, speed of convergence, level of accuracy, and stability. Despite the large computational expense of a fully-implicit computational solver, the numerical solution can be achieved in less iterative steps with larger time steps.

Compositional simulators are efficient tools to be utilized for the forecasting of gas-condensate fluid behavior and the assessing of recovery enhancement. In the early development of compositional simulators, the effect of capillary pressure was considered and it was first implemented by Coats (1980). The consideration of capillary effect was presented in the development of a fully-implicit compositional simulator that is capable of handling three-dimensional and three-phase systems.

The formulation of the simulator was equipped with equation of state and utilized the Newton-Raphson linearization procedure for the estimation of pressure, saturation, and phase compositions. An illustration of the capillary pressure variables can be found in Appendix B, where the differential governing equation is derived to form the finite different approximation. In this study, a fully-implicit compositional simulator with similar formulation as introduced in this section was utilized for the purpose of studying the effects of capillary pressure forces on fractured gas-condensate reservoirs.

Chapter 5

RESULTS AND DISCUSSION

5.1 System under study

Numerical reservoir simulation is a modeling technique greatly used in the development, forecasting, and prediction of productivity of new and mature reservoirs to obtain higher recoveries. In this study, a fully-implicit compositional simulator with similar formulation as introduced in Chapter 4 was utilized for the purpose of studying the effects of capillary pressure and relative permeability assumptions on the behavior of fractured gas-condensate reservoirs. It has been indicated that the role of capillary pressure in the distribution of fluids in the reservoir can become more effective in naturally fractured reservoirs, where the transport and distribution of fluids between the matrix and the fracture can depend on the capillary pressure and relative permeability. Naturally fractured reservoirs are typically represented as a group of matrix blocks separated and surrounded by fractures, which can be ideally as represented in Figure **2.5** in the form of "sugar-cube" model introduced by Warren and Root (1963).

In gas-condensate reservoirs, most of the gas is stored in the inner of matrix blocks and once production takes place, the fractured reservoir experiences faster depletion compared to matrix blocks. In fractured reservoirs, there is no matrix-to-matrix flow, but there is a matrix-to-fracture flow. Fractures have higher permeability and they are interconnected with each other to form a flow network to the wellbore. Once the depletion occurs, condensate starts to form on the edges of the matrix blocks and in the fracture network. As a result, the condensate will accumulate in these areas and starts to hinder the flow of the gas from the inner of the matrix to the wellbore. At this point, we would like to explore the influence of capillary pressure assumptions on the displacement of fluids in the reservoir and on the overall recovery of fluids in place.

Figure **5.1** illustrates a sampled blocks selected for a cross-sectional view in order to show the effect of condensate appearance. Figure **5.2** shows the effect of the appearance of condensate on the flow performance of fractured gas-condensate reservoirs as the pressure drops below dew point. Before the condensate starts to form on the edges of the matrix block (Figure **5.2a**), the

flow of gas from the inner of the matrix to the fracture network is flat and moves in all directions upon the establishment of pressure/gravitational gradient. Once condensate starts to form a coat on the matrix block (Figure **5.2b**), the flow of gas will be hindered and the movement will scatter around trying to establish flow paths toward the fractured channels.

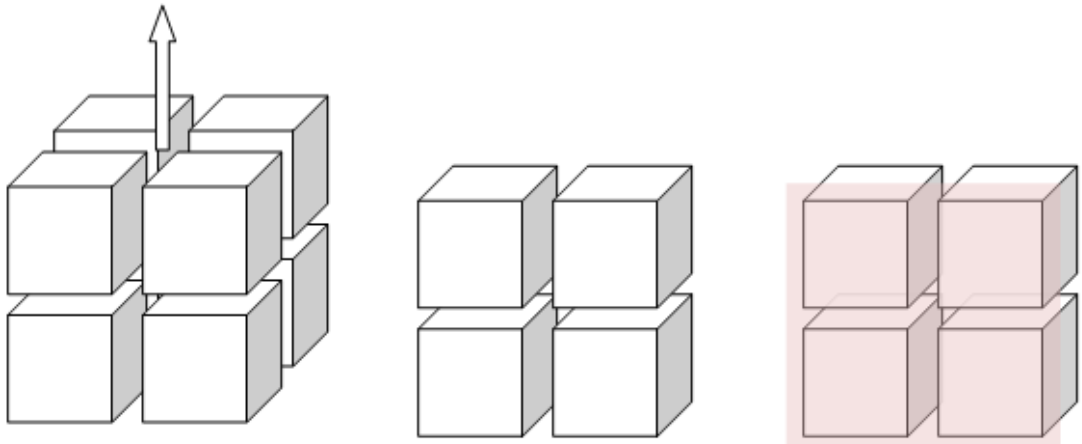

a. Sugar-cube blocks b. Taking a sample c. Cross-sectional view

Figure 5.1: Sampling from "sugar-cube" blocks

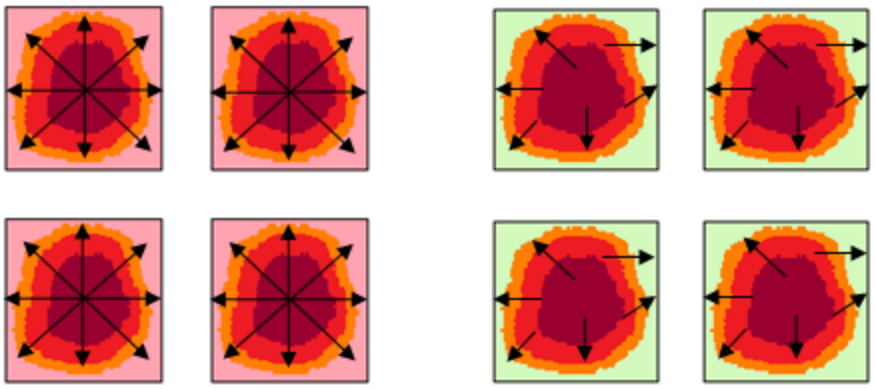

a. Flow before condensate appearance b. Flow after condensate accumulation

Figure 5.2: Flow performance as condensate starts to form on the edges of the matrix

5.2 Constructing the numerical study

In this section, the set up of the model and data sets used are introduced along with the assumptions associated with the study. First, the concept of using a single-matrix block is introduced as an elemental volume where fluids are accumulating and flowing into and out of the system. Second, several sets of compositional combinations are introduced, which had been used to analyze the condensate coating on the edges of matrix blocks.

Naturally fractured reservoirs can be represented as a group of matrix blocks separated and surrounded by fractures, in which fractures have a higher permeability and are interconnected forming a flow network. The inner matrix blocks accumulates most of the fluids in the reservoir and based on the boundary condition established by the surrounding fractures, the matrix blocks will discharge its fluids into the fractured channels to be transported to the wellbore. In nature, naturally fractured reservoirs are presented as complex reservoir systems with non-uniform structures. In order to visually describe a fractured reservoir for the purpose of studying the productivity and impairment on recoveries, naturally fractured reservoirs are ideally visualized in the form of sugar-cubes as introduced by Warren and Root (1963). This idealized model can be designed to depict the behavior of complex fractured reservoirs and facilitate their study. In order to make this idealized approach more amenable to numerical simulation, a single-block out of the stacked matrix of blocks is used to represent the behavior of the reservoir.

Over the years, the behavior of each single-block out of the stacked blocks has been used to study and understand the overall productivity of these reservoirs as shown in Figure **5.3**. According to Peaceman (1976) understanding the behavior of fractured reservoirs, which are characterized by large number of matrix blocks surrounded by highly-conductive fractures network, depends on the understanding of the performance of the single matrix blocks under different boundary conditions. Van Golf-Racht (1982) emphasized that the reason behind the use of single-matrix block to represent the reservoir is that a single block that is surrounded by fracture network is in no communication with the adjacent blocks, which makes it self-governing and a good representative sample of the building blocks of the matrix.

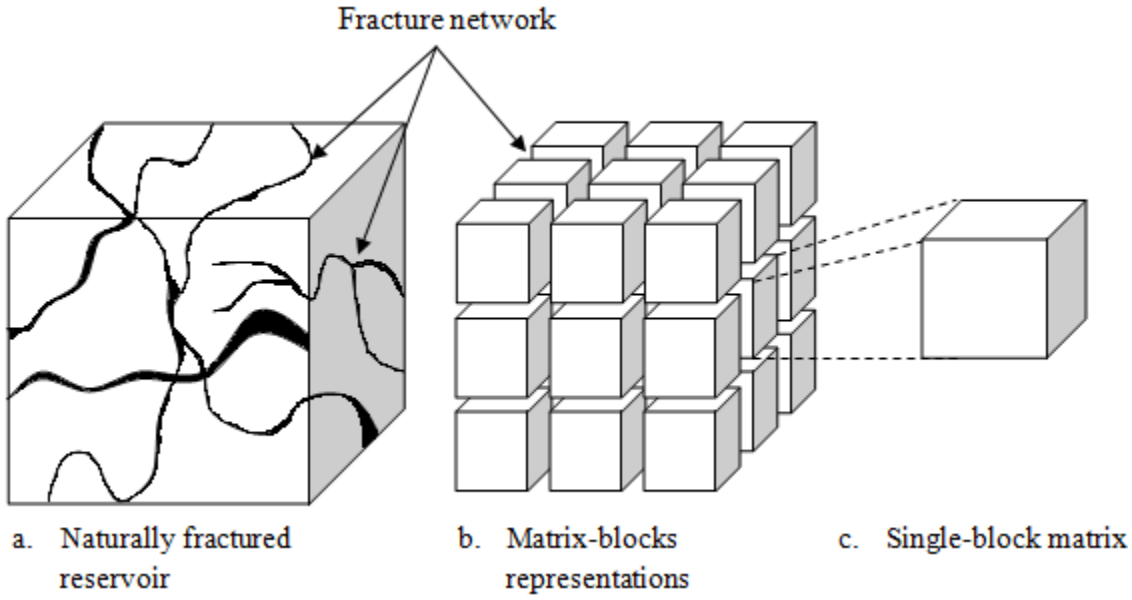

Figure 5.3: Numerical representation of naturally fractured reservoir (*after Warren and Root, 1963*)

In this study, the single-block matrix represents the elemental volume of naturally fractured reservoir with equal dimensions in x, y, and z directions, with all the sides surrounded by fracture network. All the sides of the block are open for flow upon the establishment of boundary conditions. Flow is symmetrical with respect to the x and y direction which allows one quarter of the single-block matrix capable of representing the behavior of the whole block. Due to the presence of gravitational forces, symmetry is not possible in the z direction. Figure **5.4** illustrates the new representation of the single-block matrix with the consideration of symmetrical flow. However, with the new representation, it is considered that there are no flow boundaries in the symmetry planes due to the absence of conductive channels. The single-block matrix is surrounded by fractures at the upper most layers of the four sides that are other than the symmetry planes.

The quarter block is discretized in uniform cell dimensions of 500 ft ($\Delta x = \Delta y = \Delta z$), with a total number of gridblocks of 11 x 11 x 22 as shown in Figure **5.5**, which includes the fracture gridblocks surrounding the system. From the work of Ayala (2004), it was suggested to use refined gridblocks toward the edges of the matrix block where the fractures are located as shown in Figure **5.6**, in order to allow the simulator to simply capture the condensate coating behavior.

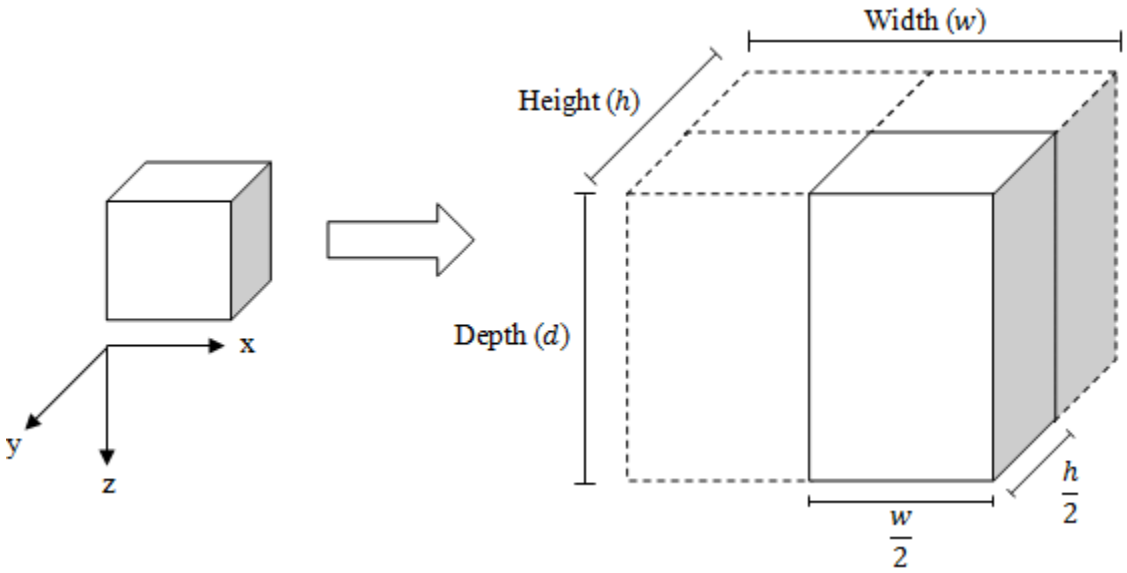

Figure 5.4: Representation of the quarter single-block matrix (*after Ayala, 2004*)

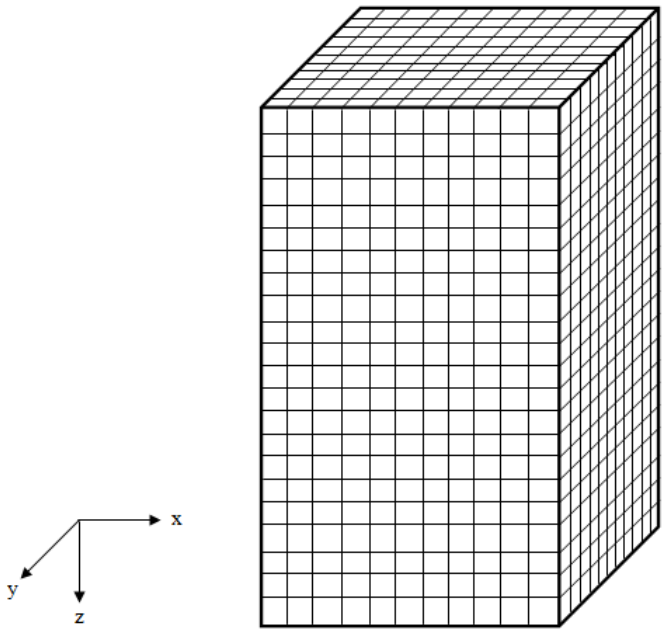

Figure 5.5: Grid block system including fracture blocks

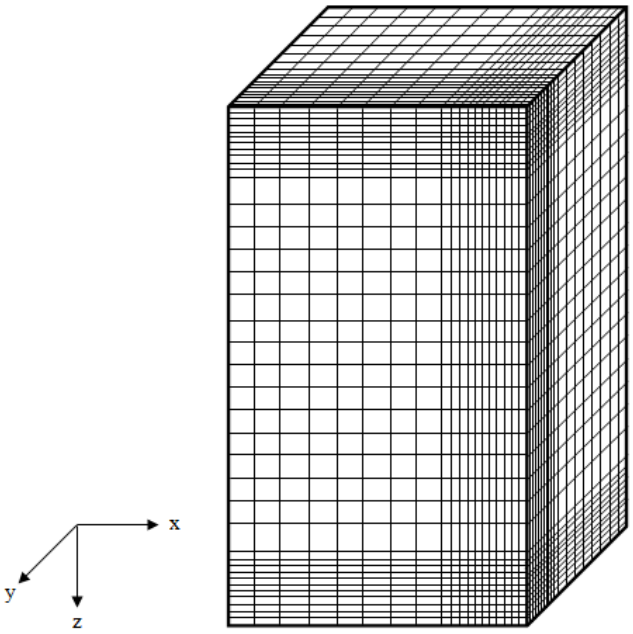

Figure 5.6: Grid refinement toward fractures

After presenting the single-block model, it is time to present the data used to construct the simulation calculations. Tables **5.1** to Table **5.7**, show the data used as parameters for the simulation study. Table **5.1** represents the variables that were kept constant throughout all simulations scenarios, which include the rock properties of the matrix and the fracture along with the initial pressures and temperatures for both domains. Table **5.2** shows the properties of the phases present in the system, which includes the properties of hydrocarbon and water. The table refers the hydrocarbon properties to Table **5.3**, where the fluid are classified and described in more detail. In addition, Table **5.4** presents the different sets of compositions data that have been used in this study to examine different coating concentration. Table **5.5** presents the surface separation facility information represented by two separators and a stock tank. Table **5.6** displays the oil/gas relative permeability and capillary pressure data, where the capillary pressure data is initiated with zeros at this stage. Table **5.7** displays the oil/water relative permeability data with a fixed capillary pressure data since the intention is not to test the effect of the oil/water capillary effect due to the absence of interactions between water and hydrocarbon. Lastly, it is important to indicate that all the scenarios considered in this study have been set to run for a simulation period of 3600 days (10 years).

Table 5.1: Constant variables throughout the study

Matrix		
Matrix block dimension	500	ft
Initial pressure	4000	psia
Temperature	200	^{o}F
Rock compressibility	0	cp^{-1}
Porosity	0.13	
Permeability	$1x10^{-3}$	md
Fracture		
Initial fracture pressure	4000	psia
Minimum fracture pressure	600	psia
Temperature	200	^{o}F
Fracture width	0.01	ft
Fracture permeability	2000	md
Fracture depletion rate	1	psi/day

Table 5.2: Fluid properties

Hydrocarbon		
Hydrocarbon properties	Table 5.3	
Effective Diffusion	0	ft^2/day
Water		
Water saturation (Swirr)	0.3	
Water compressibility	0	cp^{-1}
Initial water FVF	1	RB/STB
Water viscosity	0.78	cp
Water density at SC	62.4	lb/ft3

Table 5.3: Hydrocarbon fluid properties

Fluid Characterization							
Comp	MW_m	T_{cm} (F)	P_{cm} (psia)	Z_{cm}	ω_m	Ω_{am}	Ω_{bm}
P1	16.38	-120.01	662.81	0.28741	0.01330	0.42312848	0.08046461
P2	31.77	89.83	752.19	0.28860	0.11304	0.45192604	0.07926051
P3	50.64	245.87	581.03	0.28126	0.17244	0.45984739	0.07843675
P4	76.92	410.94	481.06	0.25534	0.23561	0.45811880	0.07791799
P5	120.13	600.51	385.00	0.26069	0.34585	0.39778691	0.07510754
P6	210.87	823.88	253.07	0.23087	0.55335	0.39778691	0.07510754

Binary Interaction Coefficients						
Comp	P1	P2	P3	P4	P5	P6
P1	0	0.000986	0.007843	0.023942	0.037841	0.047445
P2	0.000986	0	0.003695	0.010541	0.010541	0.010541
P3	0.007843	0.003695	0	0.002281	0.002281	0.002281
P4	0.023942	0.010541	0.002281	0	0	0
P5	0.037841	0.010541	0.002281	0	0	0
P6	0.047445	0.010541	0.002281	0	0	0

Table 5.4: Different sets of fluid composition

Comp	Z_1	Z_2	Z_3	Z_4	Z_5
P1	0.708800	0.692233	0.679300	0.649300	0.627800
P2	0.099000	0.099000	0.099000	0.099000	0.099000
P3	0.110800	0.110800	0.110800	0.110800	0.110800
P4	0.045000	0.045000	0.045000	0.045000	0.045000
P5	0.234660	0.052966	0.052966	0.052966	0.052966
P6	0.000001	0.000001	0.012934	0.042934	0.064434

Table 5.5: Surface separation facility information

Separator	Pressure (psia)	Temperature (F)
Primary	315	60
Second Stage	65	60
Stock Tank	14.7	60

Table 5.6: Oil/gas relative permeability and capillary pressure data

S_g	K_{rg}	K_{rog}	P_{cgo}
0.000	0.0000	0.8000	0.0000
0.040	0.0050	0.6500	0.0000
0.080	0.0130	0.5130	0.0000
0.120	0.0260	0.4000	0.0000
0.160	0.0400	0.3150	0.0000
0.200	0.0580	0.2500	0.0000
0.240	0.0780	0.1960	0.0000
0.280	0.1000	0.1500	0.0000
0.320	0.1260	0.1120	0.0000
0.360	0.1560	0.0820	0.0000
0.400	0.1870	0.0600	0.0000
0.440	0.2220	0.0400	0.0000
0.480	0.2600	0.0240	0.0000
0.520	0.3000	0.0120	0.0000
0.560	0.3480	0.0050	0.0000
0.600	0.4000	0.0000	0.0000
0.610	0.4125	0.0000	0.0000
0.640	0.4500	0.0000	0.0000
0.670	0.5050	0.0000	0.0000
0.700	0.5620	0.0000	0.0000

Table 5.7: Oil/water relative permeability and capillary pressure data

S_w	K_{rw}	K_{row}	P_{cow}
0.300	0.0000	0.8000	50.0000
0.340	0.0020	0.6500	32.0000
0.380	0.0100	0.5130	21.0000
0.420	0.0200	0.4000	15.5000
0.460	0.0330	0.3150	12.0000
0.500	0.0490	0.2500	9.2000
0.540	0.0660	0.1960	7.0000
0.580	0.0900	0.1500	5.3000
0.620	0.1190	0.1120	4.2000
0.660	0.1500	0.0820	3.4000
0.700	0.1860	0.0600	2.7000
0.740	0.2270	0.0400	2.1000
0.780	0.2770	0.0240	1.7000
0.820	0.3300	0.0120	1.3000
0.860	0.3900	0.0050	1.0000
0.900	0.4610	0.0000	0.7000
0.940	0.5450	0.0000	0.5000
0.960	0.6180	0.0000	0.3000
0.970	0.6960	0.0000	0.1000
1.000	1.0000	0.0000	0.0000

5.3 Testing different composition concentrations

Several sets of compositional combinations have been used for the analysis of the condensate coating on the edges of the matrix blocks. The purpose of this approach is to capture different severities of condensate blocking as a function of the characteristics of the fluids in place. Table **5.8** displays the different sets of composition combinations used in this study, which are denoted by *Fluid A* through *Fluid E*. Each fluid has an initial produced Condensate Gas Ratio (CGR), which is used as an indicator of fluid type and quantity of heavy components in the initial reservoir fluids (McCain, 1993). Gas-condensate reservoirs have CGR between 66.66 and 312 STB/MMSCF (McCain, 1993). Reservoir fluids characterized with a CGR less than 66.66 STB/MMSCF are considered to be wet-gas reservoirs, and reservoir fluids with a CGR larger than 312 STB/MMSCF are considered to be volatile-oil reservoirs. The first two sets of the table describe lighter fluids, where light compositions dominate over the heavy components. In these systems, it is expected to have minimal reservoir condensation. Fluid C has moderate characteristics, which allows it to be considered as the base case in all of the simulation runs for comparison purposes of severity of condensate blockage. The last two sets demonstrate the heavier fluids, where condensate is expected to appear in sufficient quantitative, dominate the pore spaces, and need large mobility.

Table 5.8: Composition combinations considered in this study

	P1	P2	P3	P4	P5	P6	CGR STB/MMSCF
Fluid A	0.708800	0.099000	0.110800	0.045000	0.023466	0.000001	66.66
Fluid B	0.692233	0.099000	0.110800	0.045000	0.052966	0.000001	116.46
Fluid C	0.679300	0.099000	0.110800	0.045000	0.052966	0.012934	153.27
Fluid D	0.649300	0.099000	0.110800	0.045000	0.052966	0.042934	242.32
Fluid E	0.627800	0.099000	0.110800	0.045000	0.052966	0.064434	310.05

Before the effect of capillary pressure on the productivity of gas-condensate reservoirs is analyzed, it will be assumed that there is no oil-gas capillary pressure effect. For simplicity, the oil-gas capillary pressure values will be zeroed in order to initially demonstrate the influence of the different compositional combinations on the recovery schemes of gas-condensate reservoirs. In addition, this study neglects diffusive during the analysis of the productivity of naturally fractured gas-condensate reservoir.

Figure **5.7** to Figure **5.23** display the results obtained from the numerical study using the different compositional combinations introduced in Table **5.8**. This section introduces the behavior of naturally gas-condensate reservoir using a base case (*Fluid C*) in order to set the bases for the analysis of heavy and light fluids in place. Figure **5.7** presents the recovery of gas, molar hydrocarbon, and condensate using compositional combination of Fluid C. Figures **5.7** represents a typical recovery behavior of a gas-condensate system, where the recovery starts at the same point and maintain the same recovery until the pressure drops below dew point and condensate appears. The production profile and the recovery trends indicate that the dew point pressure is reached after 828 days of production.

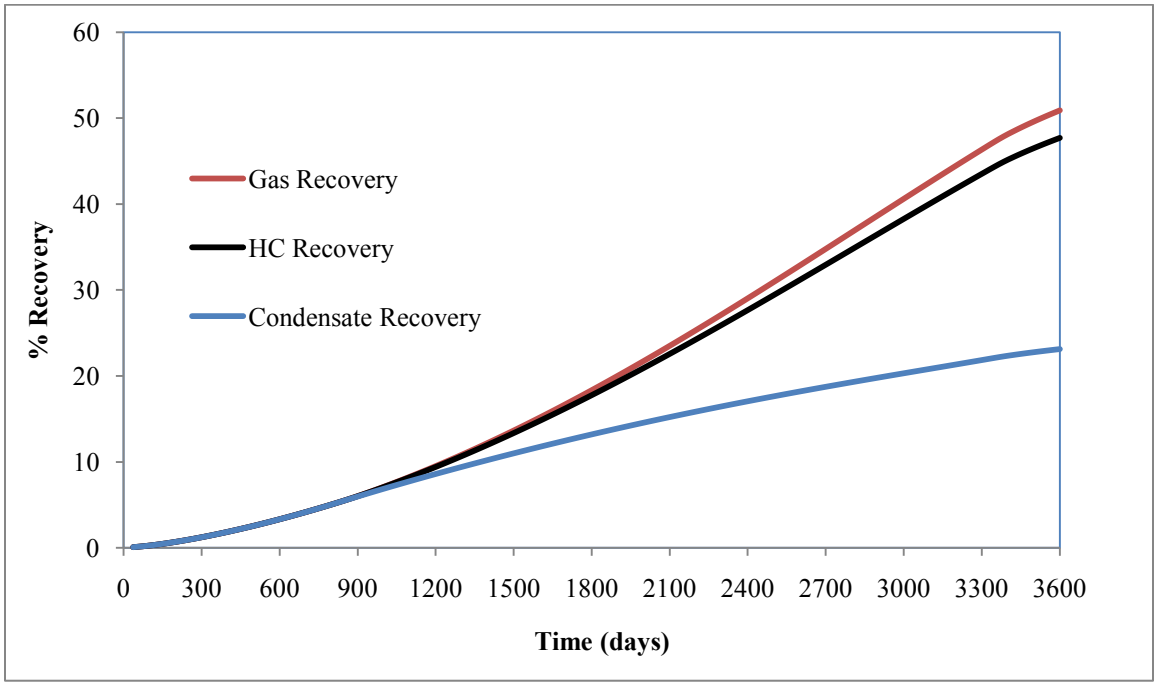

Figure 5.7: Gas and condensate recoveries for Fluid C

Once condensate starts to form, the molar recovery and condensate recovery will depart from the recovery of gas. At the end of 10 years of production and under the fracture depletion condition illustrated by Figure **5.8**; recoveries of gas, molar hydrocarbon, and condensate from the original fluid in place are determined to be 50.93%, 47.71%, and 23.14% respectively.

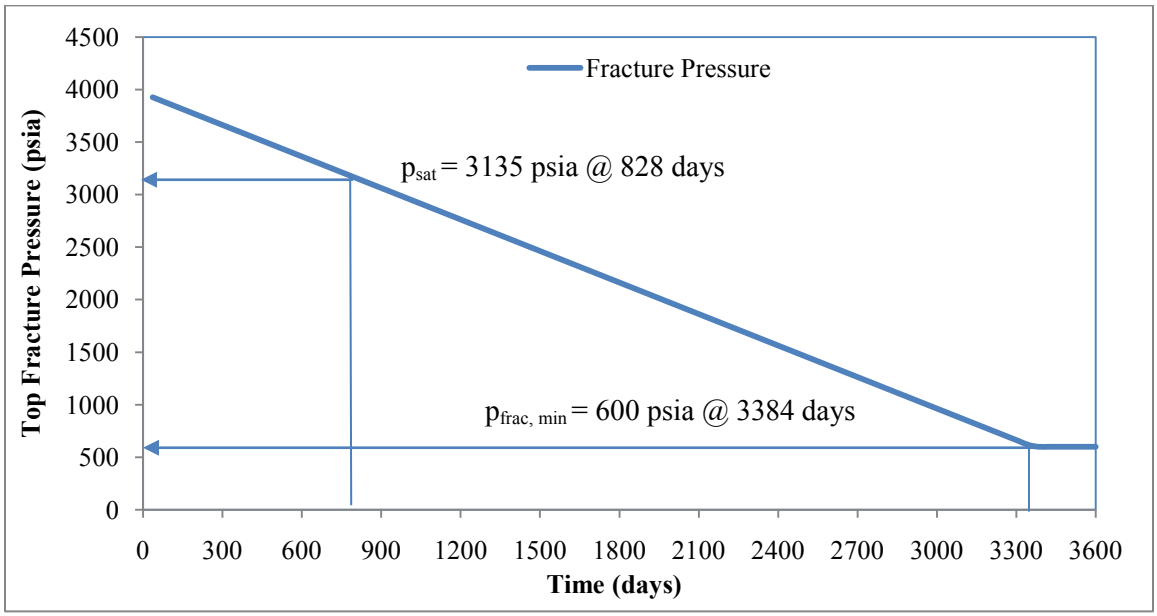

Figure 5.8: Fracture pressure profile for Fluid C under a 1 psi/day depletion rate

Figure **5.9** presents the production rates for the quarter block that is under evaluation. It shows an increasing trend of production at surface for gas, molar, and condensate. Once condensate forms, insignificant changes are observed in the production rate around 828 days (Figure **5.9**) especially in the case of gas production. Condensate production increases at surface conditions before reaching saturation pressure because as gas flows to the surface under surface pressure conditions, which are lower than the saturation pressure, condensate tends to form on the surface. After condensate starts to form at reservoir conditions, the production tends to decline in a firmly steady pattern. The reason of the low production of condensate despite the richness of condensation in the reservoir as shown in Figure **5.10** is due to the fact that most of the heavy components of the condensate are lost to the formation. Towards the end of simulation period, a noticeable sharp decline is observed at time 3384 days for all production rates. The sudden decline is a result of reaching the minimum fracture pressure of 600 psia which is maintained to the end of simulation period as shown in Figure **5.8**.

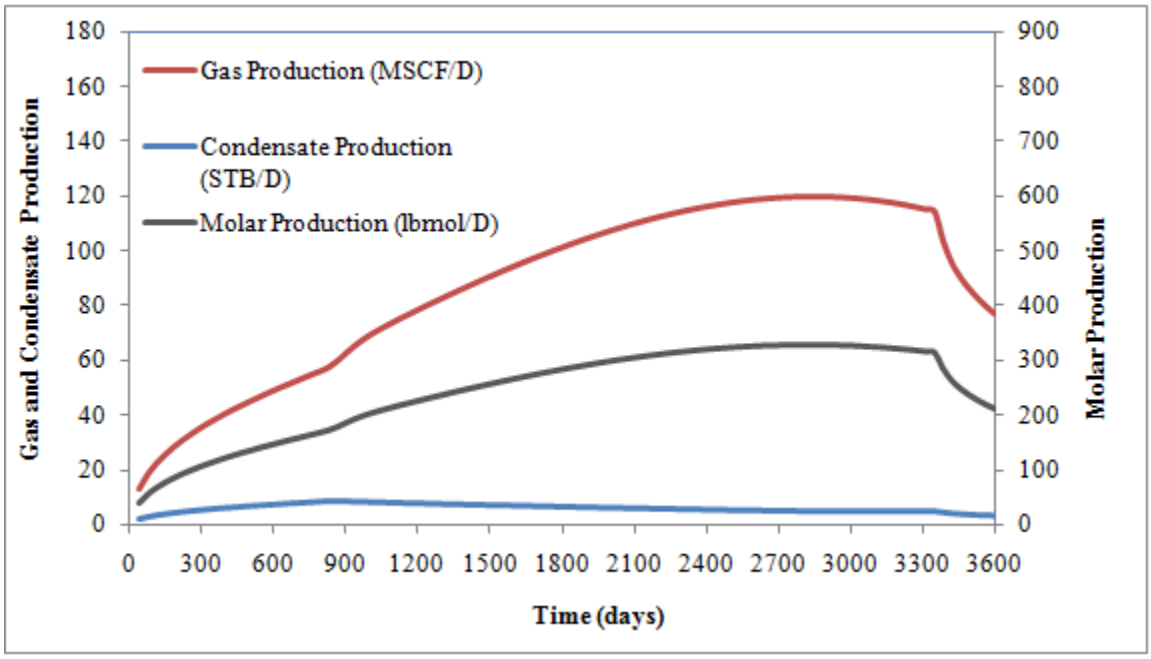

Figure 5.9: Quarter block production rates for Fluid C

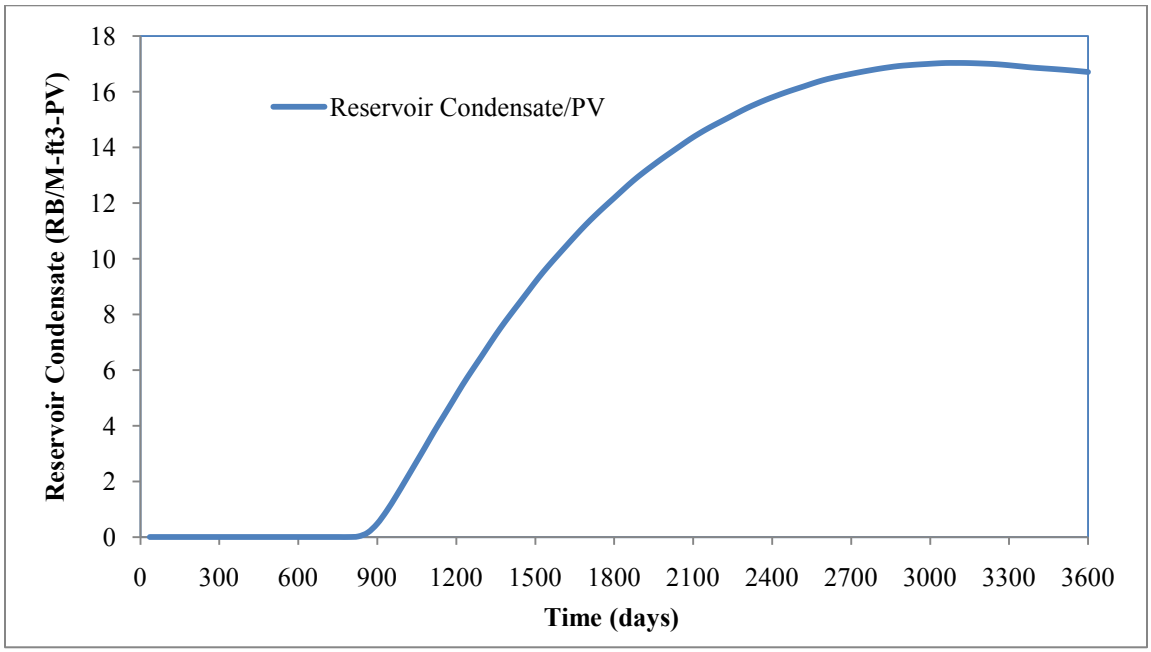

Figure 5.10: Condensation in the reservoir for Fluid C

Figure **5.11** displays the condensate saturation profiles at different times, for a mid-line vertical cross section of the representative block. Figure **5.11** illustrates the accumulation and propagation of condensate which hinders the flow of gas located at the inner portion of the block. The thickness of the condensation coating follows the same condensation profile shown in Figure **5.10**. Once the condensate forms it starts to accumulate on the edges of the matrix as shown at 1000 days and keeps coating the edges of the matrix as time progresses. The condensate continues to accumulate on the edges of the matrix and tends to move toward the inner of the matrix. As condensation continues the gas in the inner portion of the matrix will start to feel the impairment of flowing to the production channels.

Condensate formation starts at the edges of the matrix block where pressures are lower due to their proximity to the fractures network. At 1200 days, condensate coats all sides of the block. Coating is a function of the pressure depletion at each point of the matrix block. Once the pressure drops below saturation pressure, condensate invades that given location where the drop in pressure has been reached. As the pressure declines toward the inner of the matrix, condensate will continue to immigrate until it covers the inner portion of the matrix as shown at 3000 days. Referring to the same time (3000 days) in Figure **5.10**, the trend of the condensation tends to decline firmly after reaching the maximum condensation, which indicates that the continues depletion caused some of the condensate to revaporize. Toward the end of the simulation period, the condensate will experience revaporization at the edges of the matrix as indicated in Figure **5.11** at 3600 days, where that saturation at the edges is approximately 9%. The 3600 days snapshot of condensate saturation displays the situation where condensate has flooded the entire matrix, thus impairing the flow of gas out of the matrix.

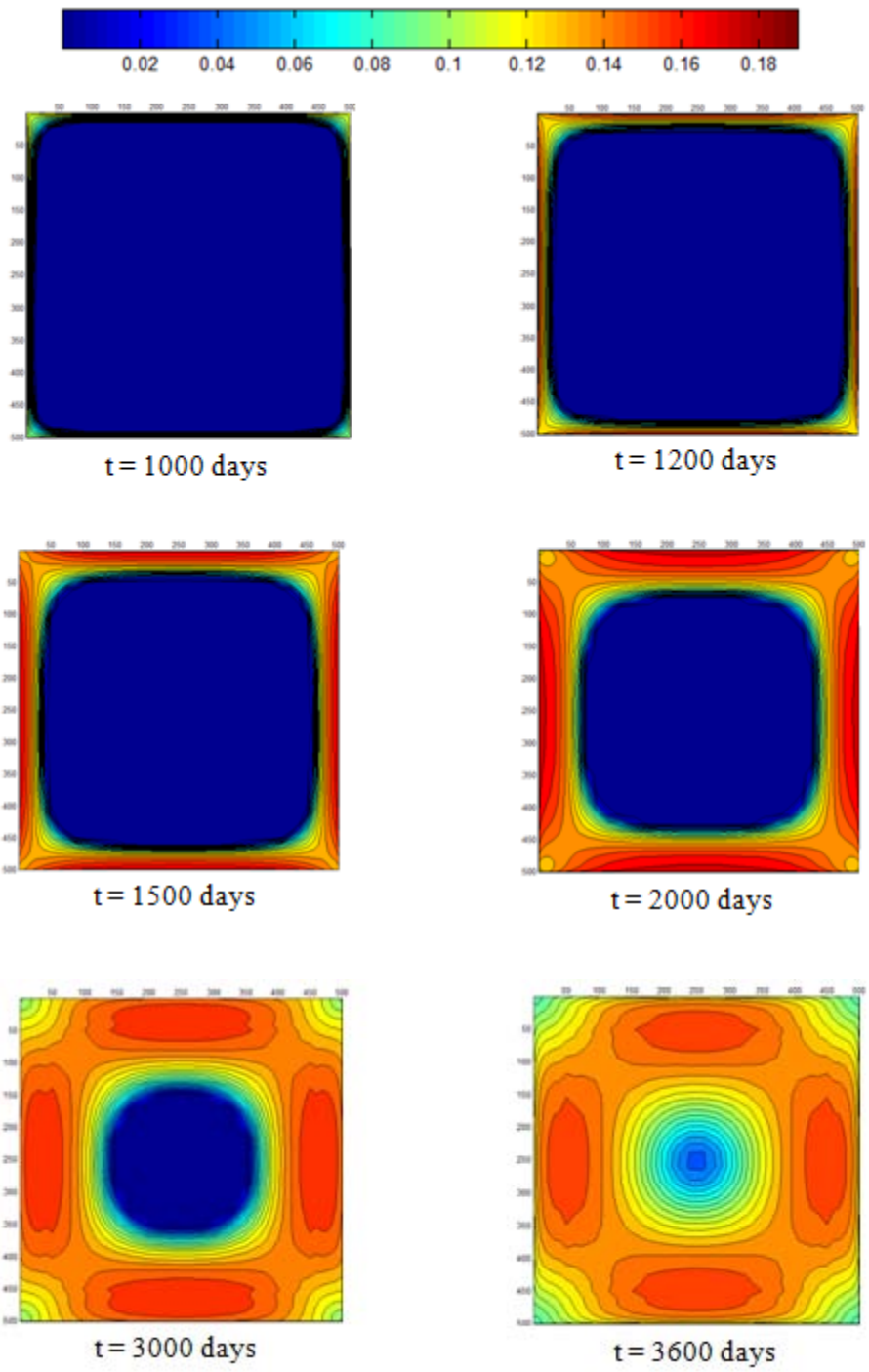

Figure 5.11: Condensate saturation profiles for Fluid C

In order to test the effect of composition on the severity of condensate coating and its effect on recovery, two lighter and two heavier fluid characterizations were studied and compared to the results of the intermediate case (Fluid C). The first two sets of the table (Table **5.8**) describe the lighter fluids denoted as Fluid A and Fluid B, where light compositions dominate over the heavy components. The last two sets of the table describe the heavier fluids denoted as Fluid D and Fluid E, which consist mainly of heavy components and few light ends. The same simulation conditions had been applied to all of the sets in order to have one common ground for comparison. Since the concentrations of the components of all of the sets are different, each of the sets has a different condensate content which controls the overall content in the reservoir and the surface recovery of hydrocarbon. Figure **5.12** represents the condensate content of the reservoir fluids of Fluid C which is initiated at 153.3 bbl/MMSCF and maintained until condensate forms in the reservoir. The condensate content of gas in place and the condensate content in the well stream is the same until the saturation pressure is reached and condensate starts forming, which at this point the condensate content will decline due to the lost heavy components to the formation. As the depletion progresses, condensate revaporizes and the trend of the condensate content of well stream will pick up toward the curve of the condensate content of gas in place.

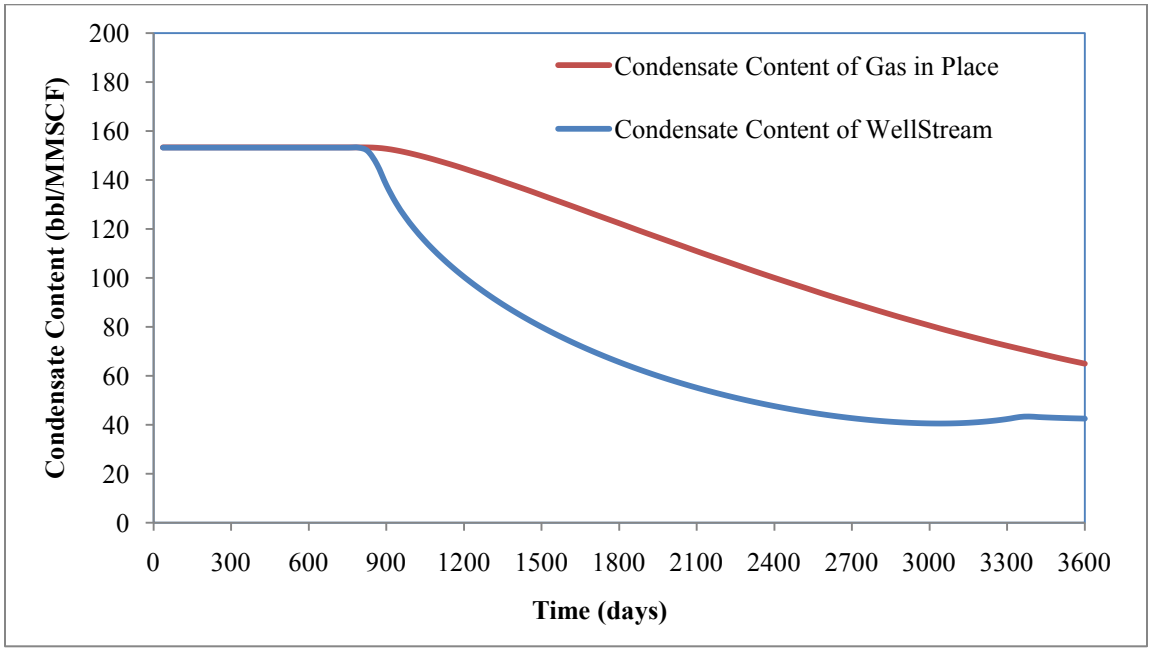

Figure 5.12: Condensate content changes for Fluid C

The difference between the two curves represents the severity of impairment applied by the condensate coating on the recovery of fluids at the surface. As the condensate starts to form on the edges of the matrix blocks, where the fractures are located to withdraw fluids for production, fluids with light ends will start to flow through the edges to the surface as lean gas. As the lean gas reaches the surface, where the pressure conditions are lower than saturation pressure at reservoir conditions, condensate drops out but in less quantities compared to the condensate content of the reservoir fluids, which is illustrated by the gap between the two condensate contents of Figure **5.12**.

As the concentrations of the light components becomes more dominant over the heavy components, the condensate content in the reservoir and at surface is reduced. Figure **5.13** represents the condensate content of the reservoir fluids of Fluid A which is initiated at 66.7 bbl/MMSCF and maintained until condensate forms in the reservoir. The condensate content of gas in place and the condensate content in the well stream is the same until the saturation pressure is reached and condensate starts forming. Due to the low concentration of heavy components, a very slight decline is felt in the condensate content of the reservoir fluid. Figure **5.14** illustrate the low condensate saturation in the reservoir, which is extremely low compared to the condensate saturation of the intermediate gas composition.

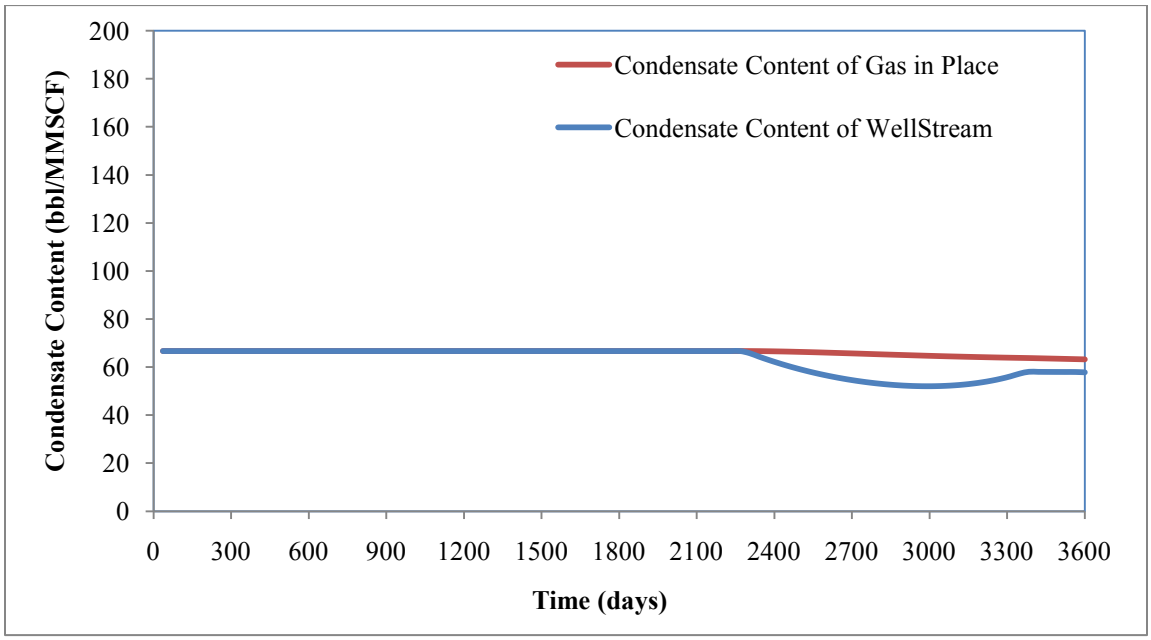

Figure 5.13: Condensate content changes for Fluid A

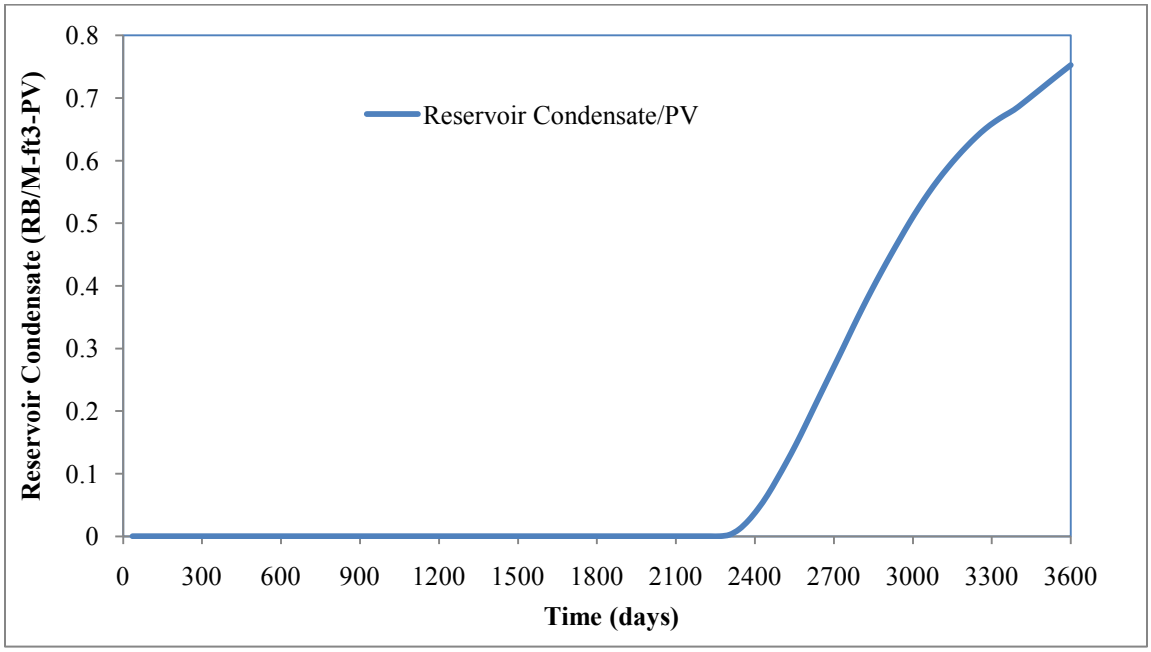

Figure 5.14: Condensation in the reservoir for Fluid A

With the low condensation in the reservoir, the gas is allowed to flow to surface with insignificant impairment. As the gas reaches the surface, condensation take place in quantities very close to the amount of condensation that appears in the reservoir as indicated by the small difference between the two curves of condensate content in Figure **5.13**. The appearance of condensate takes place very late in time due to the fact that the saturation pressure for this type of condensate combination is 1702 psia which is reached after depleting the reservoir for 2268 days. Figure **5.15** presents the late appearance of condensate and the low accumulation due to the low concentration of heavy components in the reservoir. The insignificant impairment can be seen clearly by noticing the low accumulation of the thin condensate coating on the sides of the matrix block as depletion progresses in time. As a result of the insignificant impairment on the flow of gas, the productions under the conditions of Fluid A are higher compared to the base case as indicated by Figure **5.16**. The recoveries of gas, molar hydrocarbon, and condensate from the fluids in place are determined to be 53.38%, 53.14%, and 49.53% respectively.

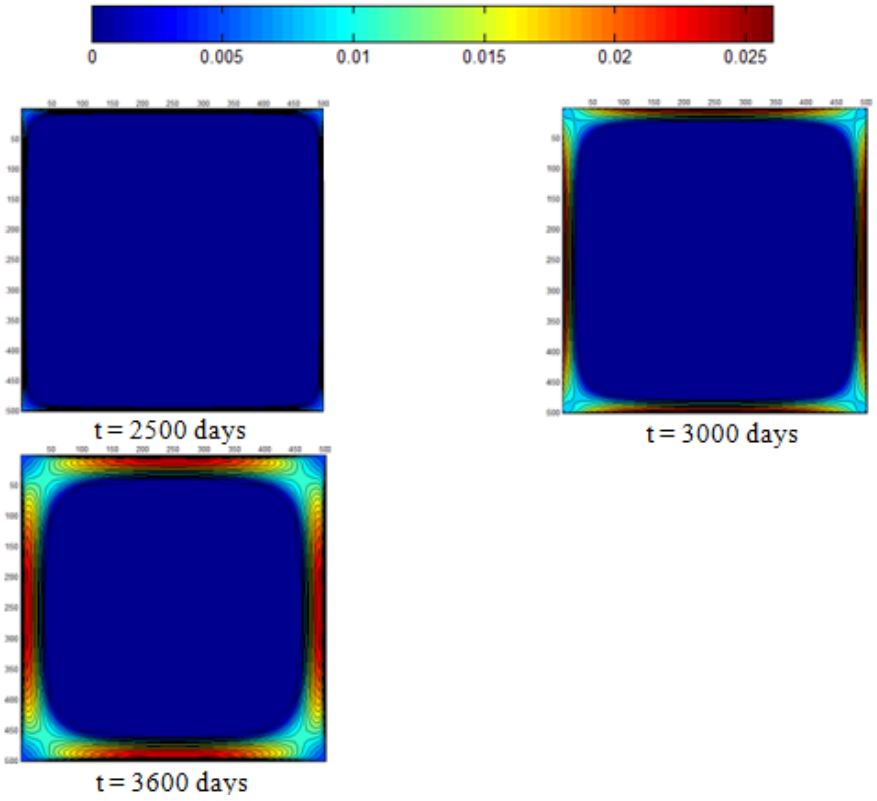

Figure 5.15: Condensate saturation profiles for Fluid A

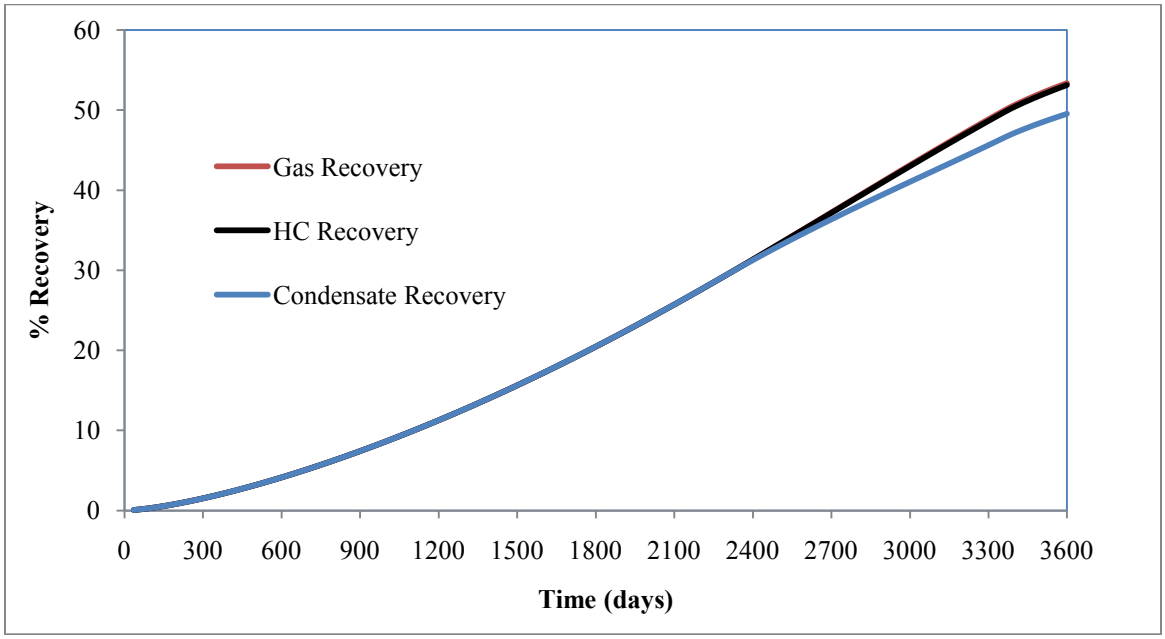

Figure 5.16: Gas and condensate recoveries for Fluid A

Figure **5.17** represents the condensate content of reservoir Fluid B which is initiated at 116.5 bbl/MMSCF and maintained until condensate forms in the reservoir. The trends of the condensate content of gas in place and the condensate content in the well stream are picking up a behavior that is the average between Fluid A and Fluid C. The condensate saturation shown in Figure **5.18** displays the amount of heavy components present in Fluid B compared to Fluid A and Fluid C. As the condensate content of the fluids in place increases, more condensate is expected to form in the reservoir as well as condensation at surface. The appearance of condensate takes place very late in time due to the fact that the saturation pressure for this type of condensate combination is 2418 psia which is reached after depleting the reservoir for 1548 days. In the case of Fluid B, once the saturation pressure is reached, condensate will accumulate faster and reach mobility sooner than in Fluid A but slower than Fluid C and that is due to the concentration of the heavy components. Figure **5.20** presents the late appearance of condensate and the low accumulation of condensate. Toward the end of the simulation, condensate coating appears to have a moderate thickness which implies more impairment compared to Fluid A due to the increase in condensate volume in the reservoir. This can be seen clearly by noticing the recoveries of fluids toward the end of the simulation as seen in Figure **5.19**. The recoveries of gas, molar hydrocarbon, and condensate from the fluids in place are determined to be 52.20%, 50.38%, and 34.48% respectively.

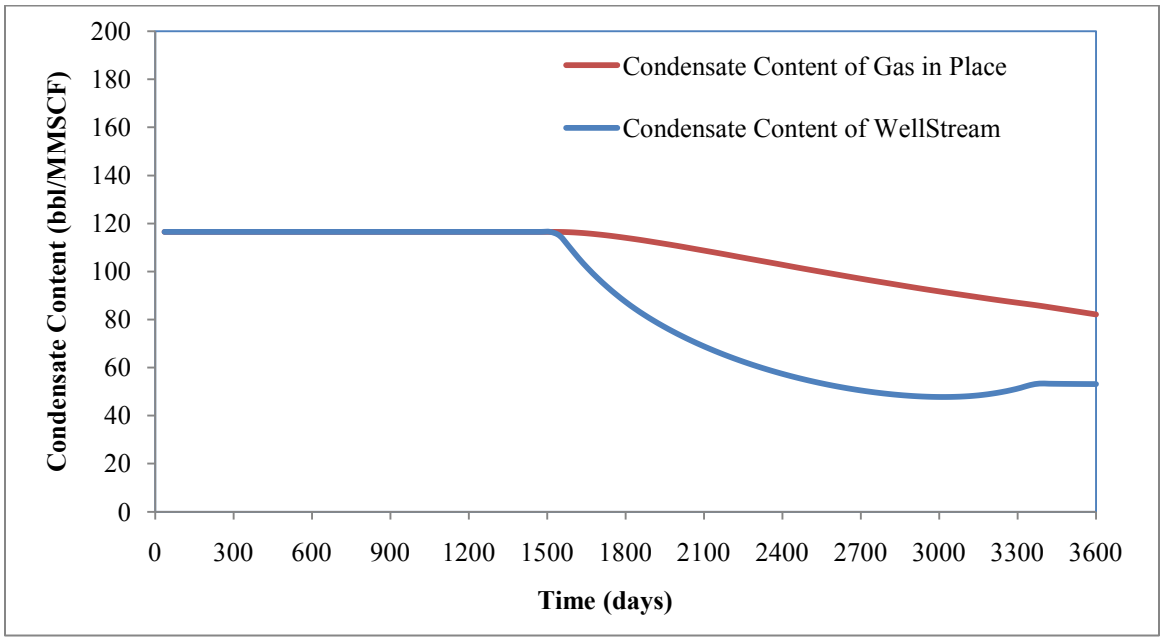

Figure 5.17: Condensate content changes for Fluid B

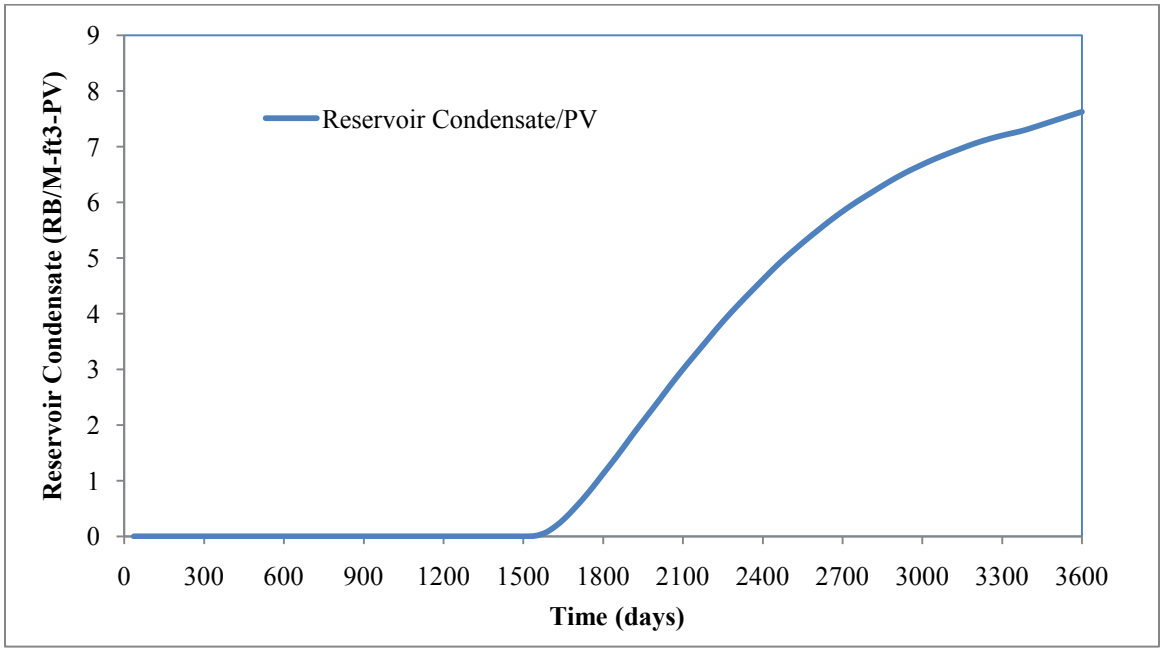

Figure 5.18: Condensation in the reservoir for Fluid B

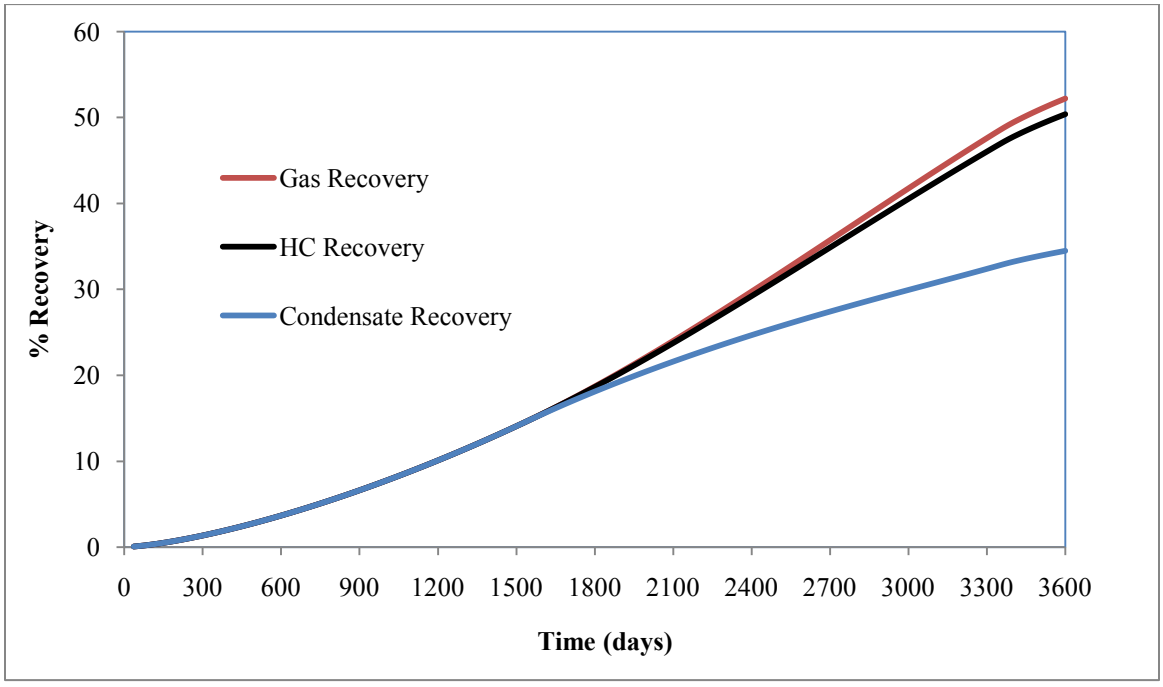

Figure 5.19: Gas and condensate recoveries for Fluid B

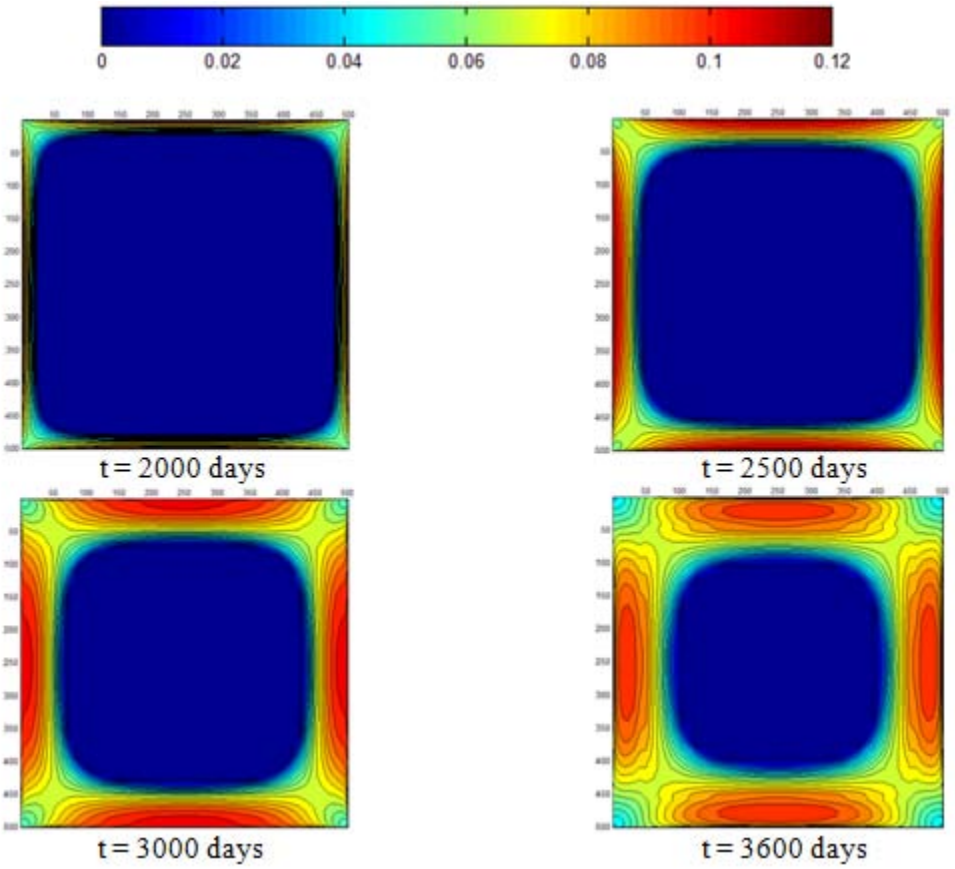

Figure 5.20: Condensate saturation profiles for Fluid B

Considering the last two sets in Table **5.8** denoted as Fluid D and Fluid E, which consist mainly of heavy components and few light ends, higher condensate volumes are expected to form in the reservoir once dew point conditions are reached. Figure **5.21** represents the condensate content of the reservoir fluids of Fluid D which is initiated at 242.3 bbl/MMSCF. Due to the high concentration of heavy components in Fluid D, the saturation pressure is reached early in the life of the reservoir and the system experiences a flush of condensate as indicated by the kink in condensate content of wellstream around 300 days. Since most of the gas in the reservoir consists mainly of heavy ends as indicated by Figure **5.22**; once condensate forms, all the heavy ends of the gas are lost to the condensate causing a continuous decline on the condensate content of gas in place. In addition, losing most of the heavy components to the formation has also caused the recovery of condensate to be low as indicated by Figure **5.23**, where the recoveries of gas, molar hydrocarbon, and condensate from the fluids in place are determined to be 46.32%, 41.49%, and 14.48% respectively.

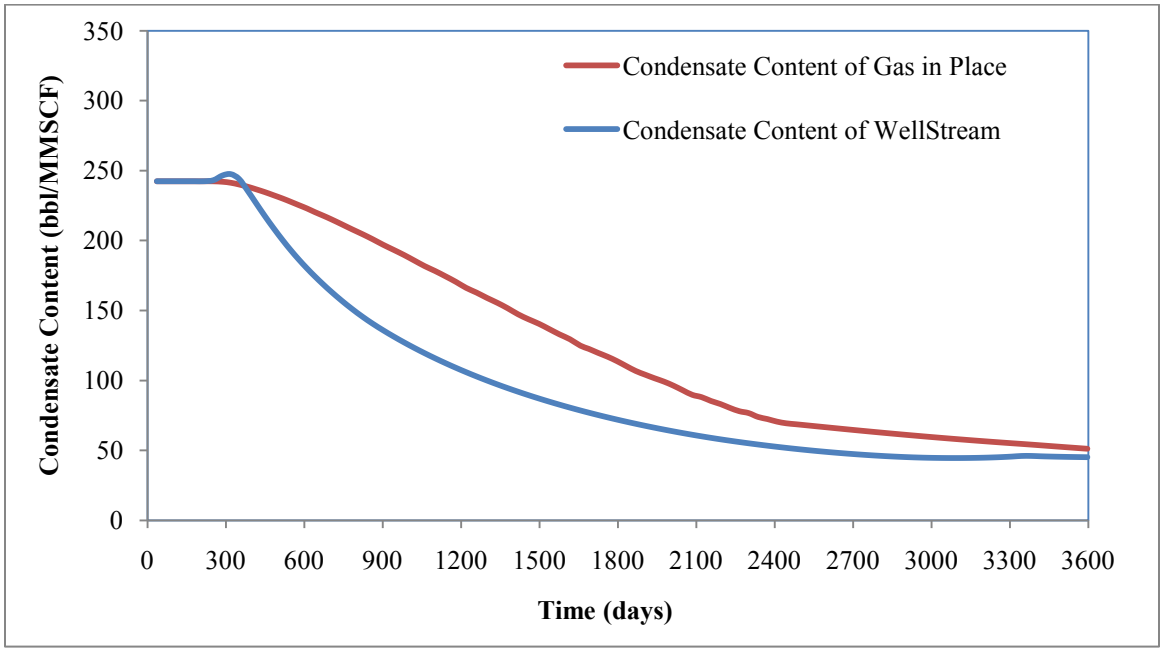

Figure 5.21: Condensate content changes for Fluid D

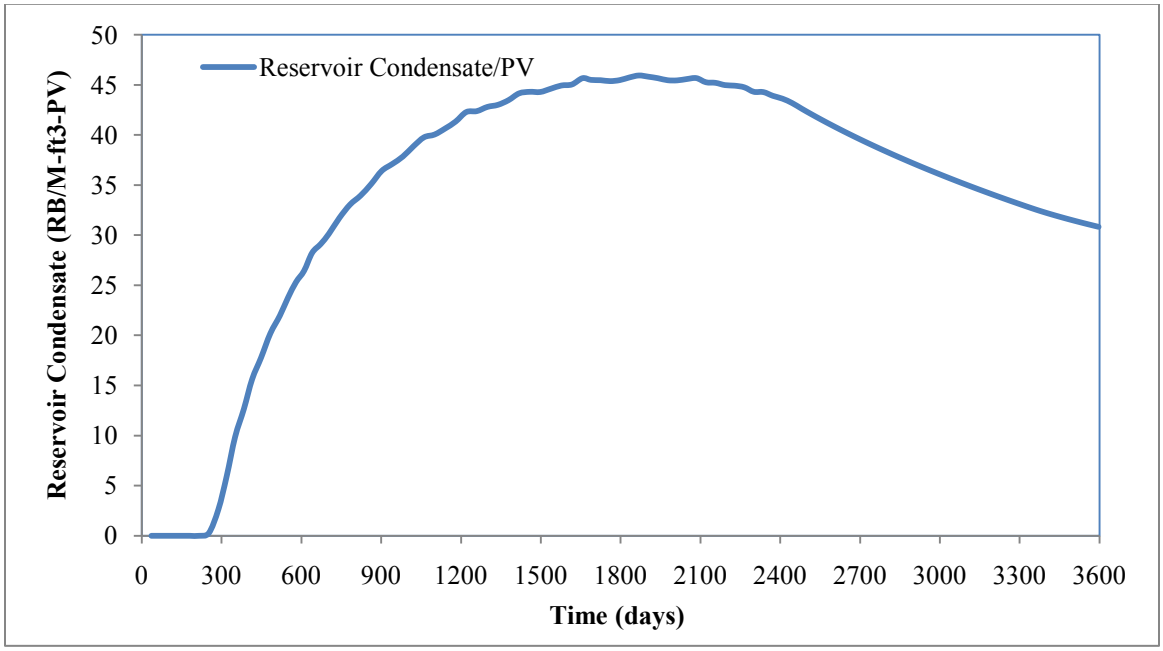

Figure 5.22: Condensation in the reservoir for Fluid D

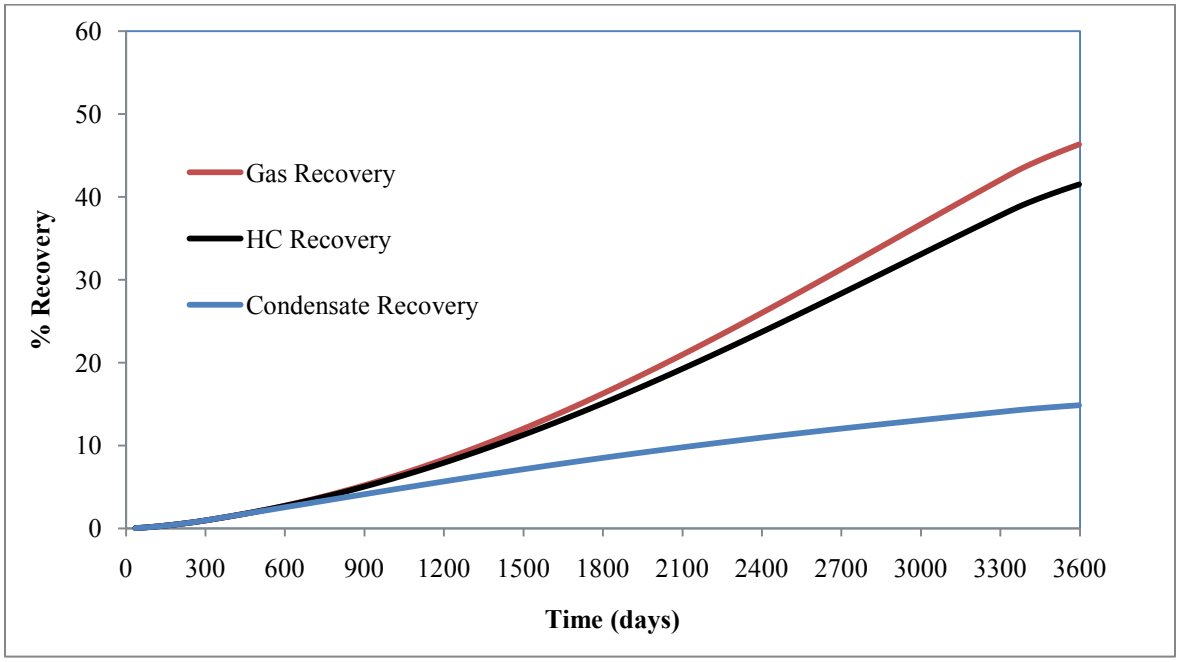

Figure 5.23: Gas and condensate recoveries for Fluid D

As the concentration of the heavy components becomes larger, the amount of condensation appears even earlier in the simulation and as a result revaporization of condensate will also take place earlier than anticipated in moderate cases. Fluid E represents the most severe case which has a maximum condensate content that is initiated at 310.1 bbl/MMSCF as shown in Figure **5.24.** Due to the high concentration of heavy components in Fluid E, the saturation pressure is reached early in the life of the reservoir and the system experience a great amount of condensate flushing the system as indicated by the behavior of the condensate content of the well stream. In addition, due to the flush of condensate at the beginning, the revaporization of condensate appears very soon in the life of the reservoir as indicated by the low saturation following the condensate appearance in Figure **5.26**. Under the conditions of Fluid E, it is very clear that due to the high volume of condensation and the early revaporization of condensate, most of the heavy components are lost to the formation as indicated by the interception of the two curves of the condensate content at 1300 days (Figure **5.24**). The trend of the condensate saturation curve presented in Figure **5.25** highlights the amount of condensate in the reservoir and the revaporization that takes place, which is indicated by the firm decline in condensate saturation. Moreover, the recoveries for Fluid E of gas, molar hydrocarbon, and condensate from the fluids in place are determined to be 44.24%, 38.90%, and 14.66% respectively as shown in Figure **5.27**.

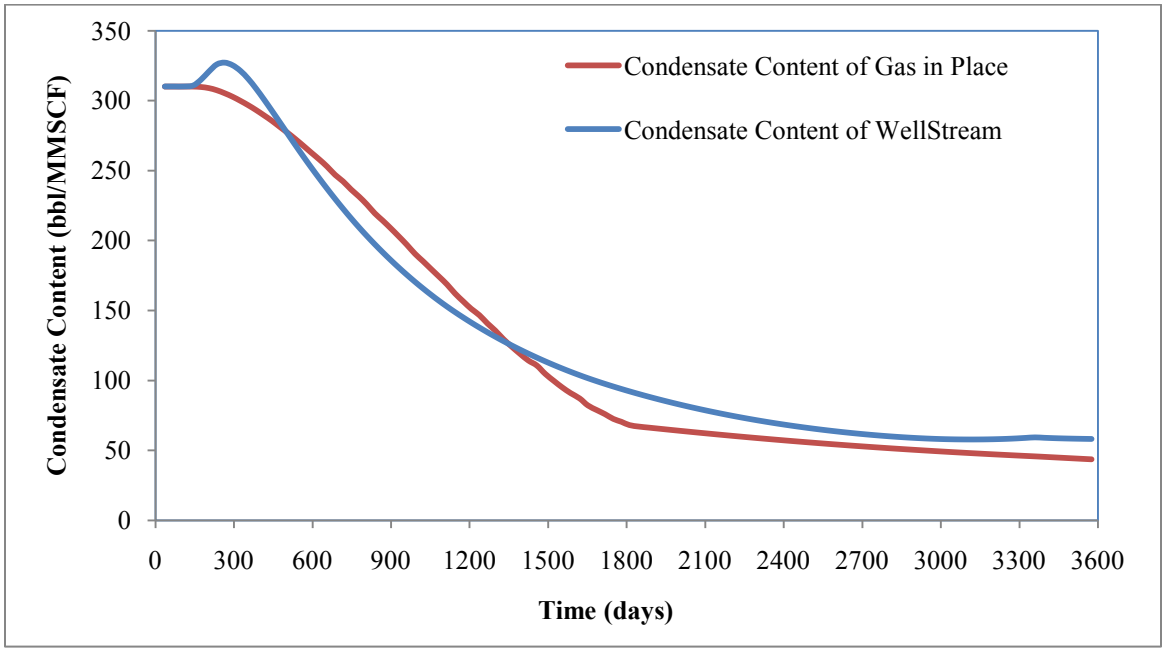

Figure 5.24: Condensate content changes for Fluid E

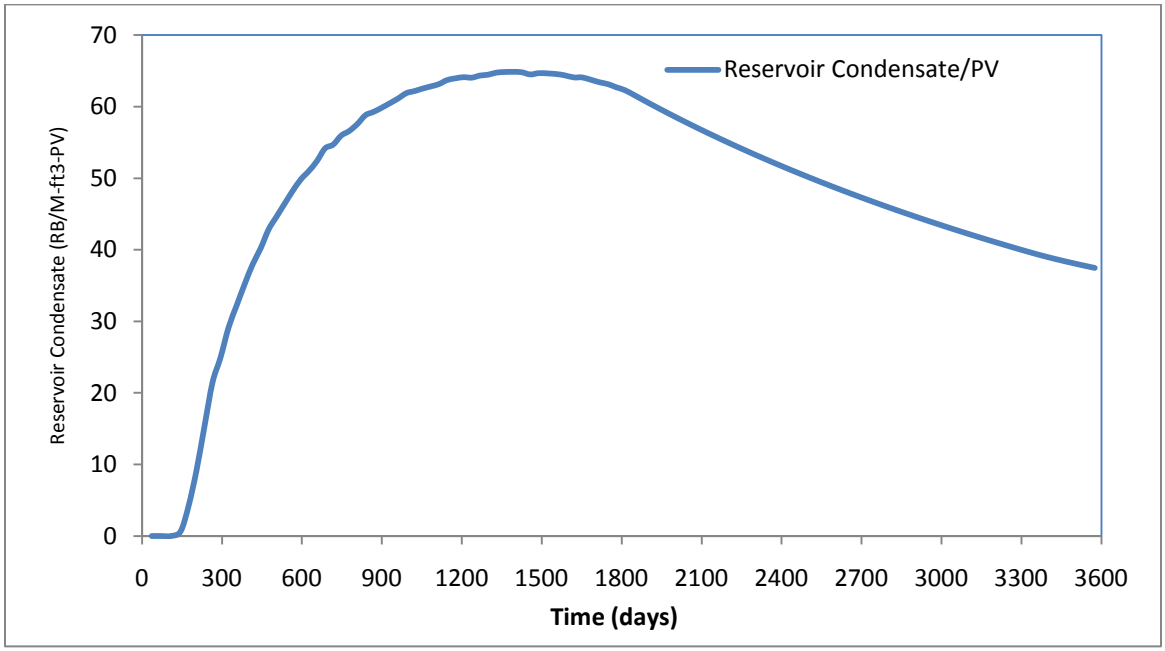

Figure 5.25: Condensation in the reservoir for Fluid E

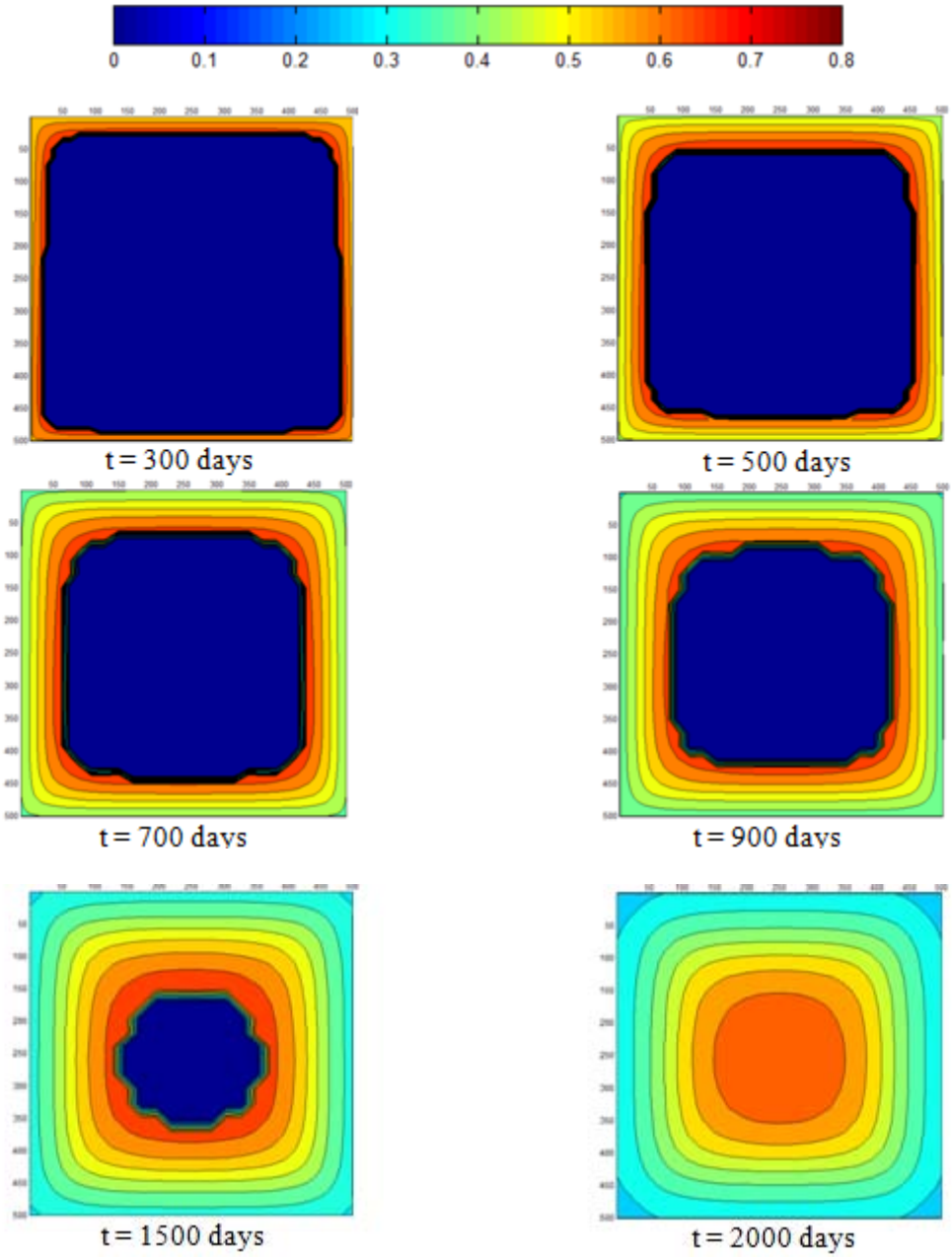

Figure 5.26: Condensate saturation profiles for Fluid E

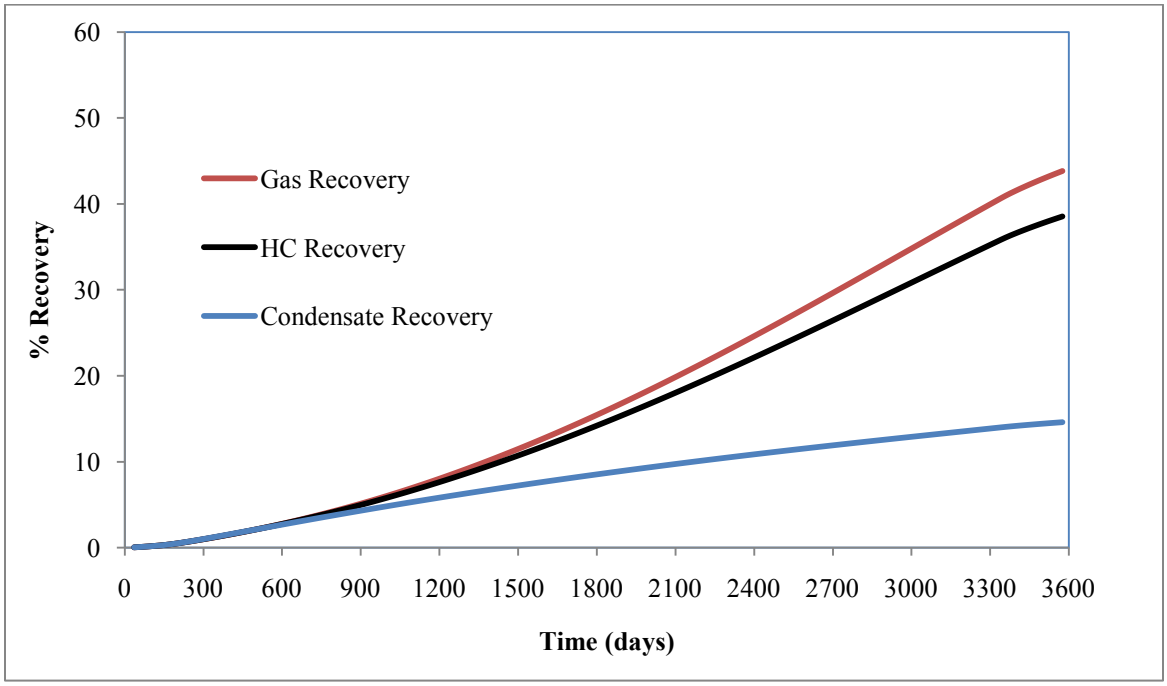

Figure 5.27: Gas and condensate recoveries for Fluid E

In summary, the saturation pressure point is controlled by the concentration of heavy components in reservoir fluid. The sooner the saturation pressure is reached the sooner condensate appears and hinders the overall recovery of fluids. In addition, as the concentration of condensate increases, more heavy components are lost to the formation and less recovery of condensate is achieved at surface because most of the gas produced is lean gas. Eventually, the overall production are higher with the leanest concentration represented by Fluid A and Fluid B because the appearance of condensate is not expected in the early life of the reservoir, and the gas is allowed to flow freely. The intermediate gas composition represents a more common occurrence for gas-condensate reservoirs, which in this project will be selected for further analysis using capillary effects and relative permeability testing. Heavy condensate concentration showed lower productions especially for condensate since most of the components are lost to the formation and producing leaner gas to the surface.

5.4 Analysis of capillary pressure effects

The focus of this section is to analyze the capillary pressure effect on the behavior of naturally fractured gas-condensate reservoirs with intermediate condensate content. In order to carry out this study, an applicable capillary pressure model must be selected in order to represent the capillary pressure curves. The selection included interactive models in which the shape of the capillary curve changes as a consequence of the interfacial tensions between rocks and fluids in a hydrocarbon reservoir, grain sizes and distribution, geometry of pore spaces, and the wetting characteristics of the fluids.

One of the most commonly used capillary pressure models is the Brooks and Corey. In the capillary pressure model of Brooks and Corey (1966), the pore size distribution index was introduced in the general form of equation (2.5) to represent the heterogeneity of the porous medium. The indication of the heterogeneity relies on the value of the pore size distribution index; the smaller the distribution index, the greater the heterogeneity of the formation. The value of the pores size distribution index is different from one reservoir to another based on the rock type, pore sizes, and geometry. Thus, various values of the distribution index were tested using a constant entry pressure of 0.1 psia, in order to indicate the range of reliable distribution index values to be associated with the current model. An illustration of the effect of heterogeneity on the capillary pressure calculations using Brooks and Corey's model is displayed in Figure **5.28**.

Using the same conditions applied to the different composition concentration earlier; the total recovery, appearance of condensate in different regions of the matrix block, and the condensate saturation profile has been studied. The analysis included comparing the behavior of the fractured gas-condensate reservoir after the activation of the capillary pressure using several different capillary pressure curves. The aim of this work was to address the influence of capillary forces on the reservoir fluids' distribution once condensate reaches the critical saturation of 0.08 and starts mobilizing and invading pore spaces.

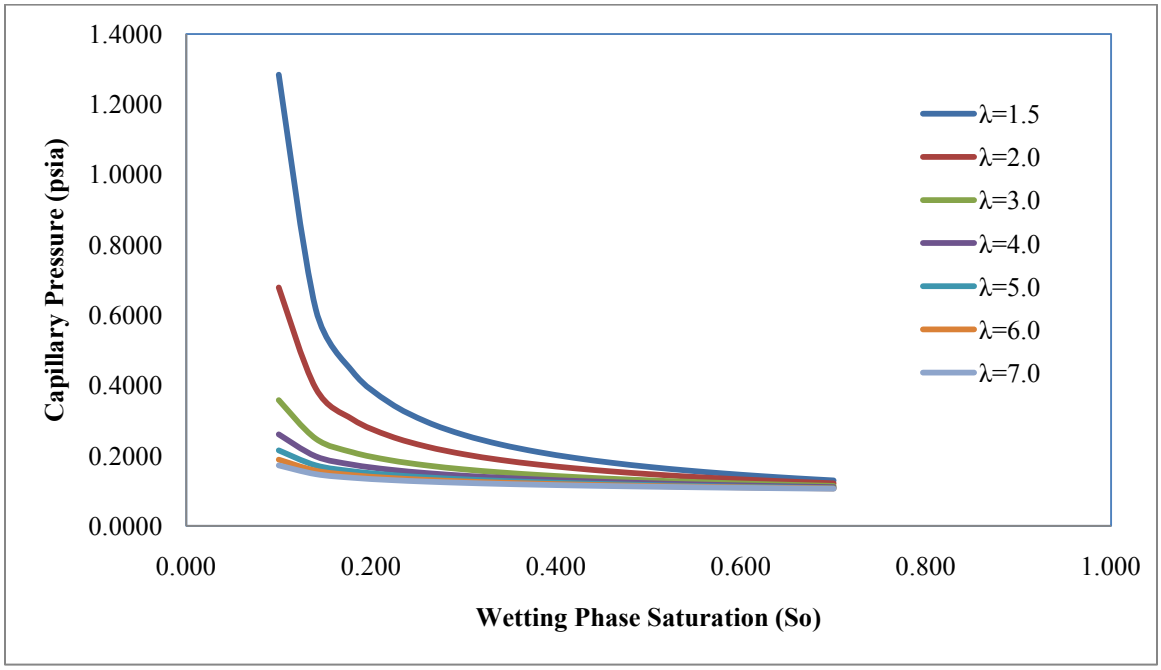

Figure 5.28: Capillary pressure curves at different pores size distributions

Apart from expecting different behaviors applied by the different curves obtained using different pore size distribution indexes, the results showed similar behavior in terms of fluid distribution, movement, and recovery. Figure **5.29** to Figure **5.31** indicate that the behavior of fluids using the compositional combination of Fluid C behaves similarly even after the activation of capillary pressure effect. Figure **5.29** shows the condensate saturation profile which mimics the exact behavior as seen earlier in Figure **5.11**, where the condensate appears at 828 days and propagate smoothly toward the inner of the block. In addition, the appearance of condensate at different locations of the matrix block appeared to be the same. Three blocks out of the total matrix blocks had been chosen to investigate the movement of the condensate, block from the top (1 1 9), block from the middle (1 1 22), and block from the bottom (1 1 34). Figure **5.30** tracks the movement of condensate in the indicated blocks, and it apparently shows the same track of condensate movement obtained without the activation of capillary pressure effect. In terms of recoveries, Figure **5.31** shows that there was a slight increase which is in fact totally insignificant and would not affect the overall behavior of the system. The recoveries obtained for gas, molar hydrocarbon, and condensate from the fluids in place were determined to be 50.99%, 47.78%, and 23.48% respectively.

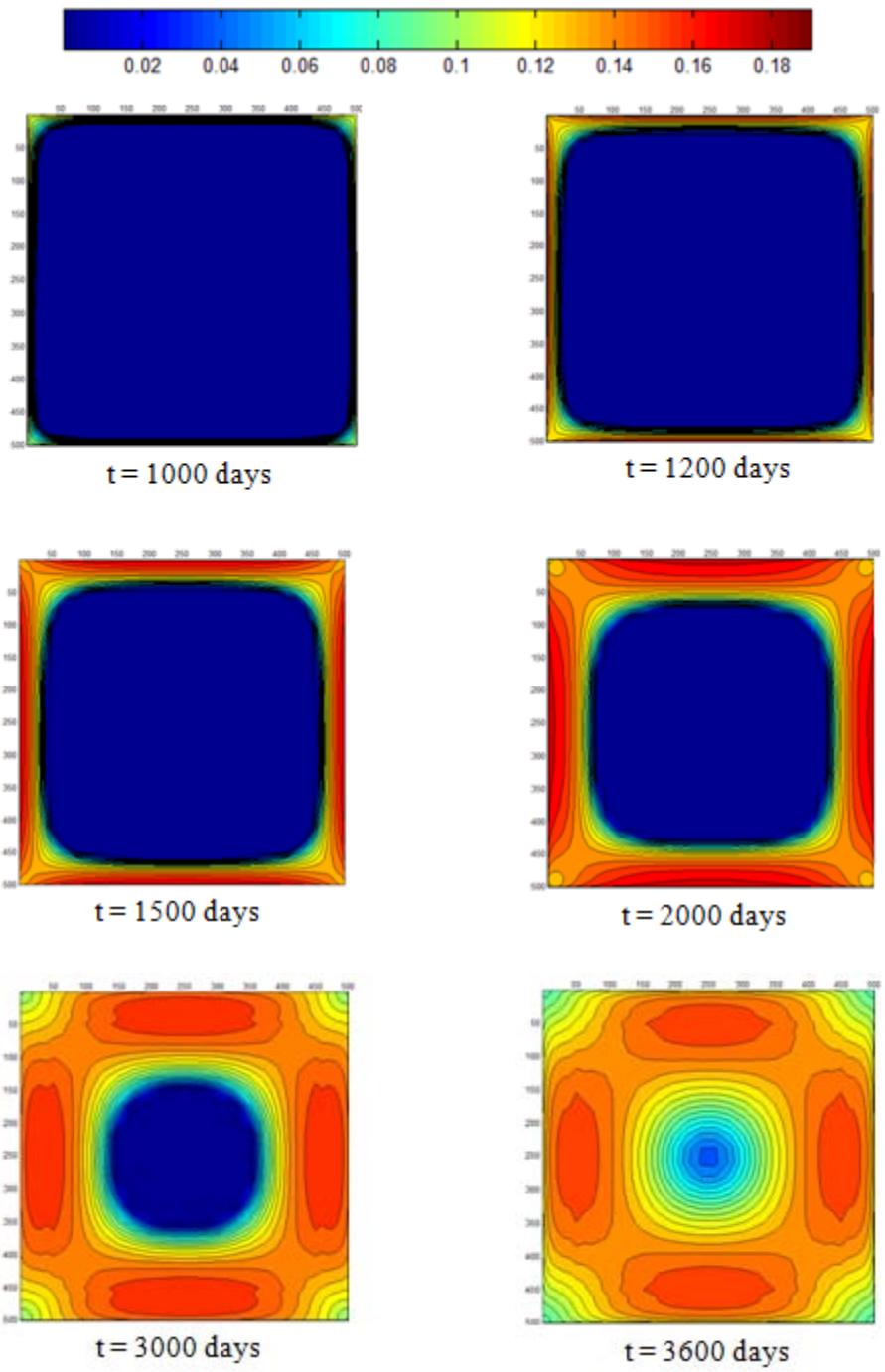

Figure 5.29: Condensate saturation profile using Fluid C with capillary pressure activated using λ =3

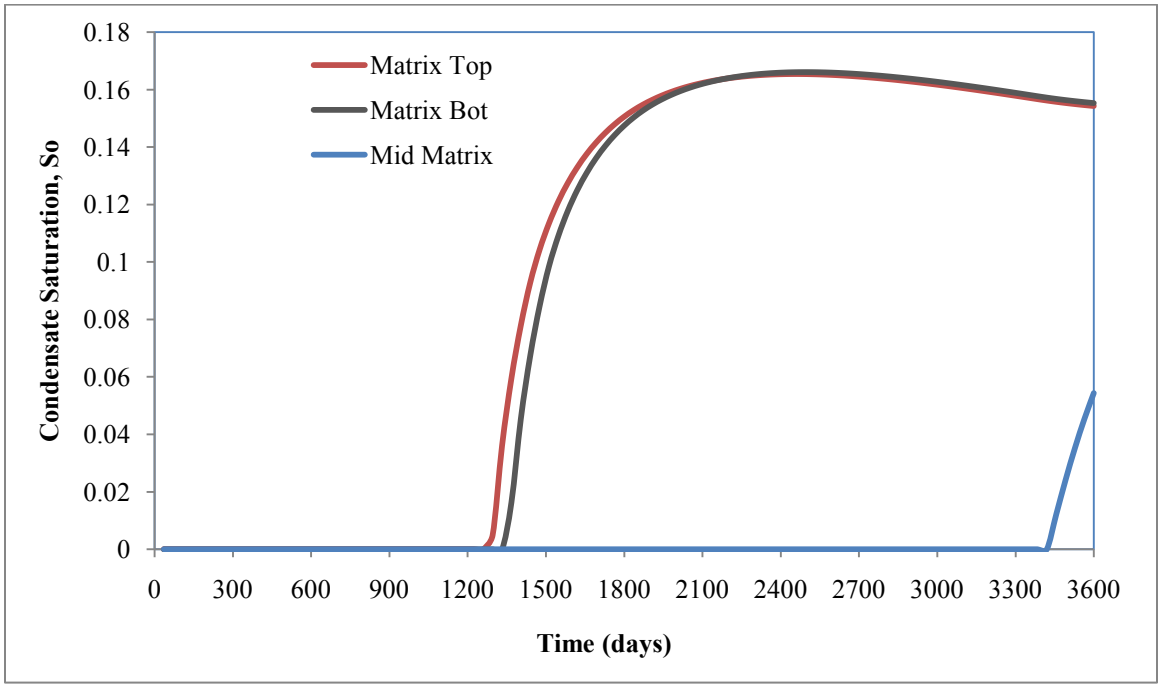

Figure 5.30: Condensate evolution at different locations in the matrix block using λ =3

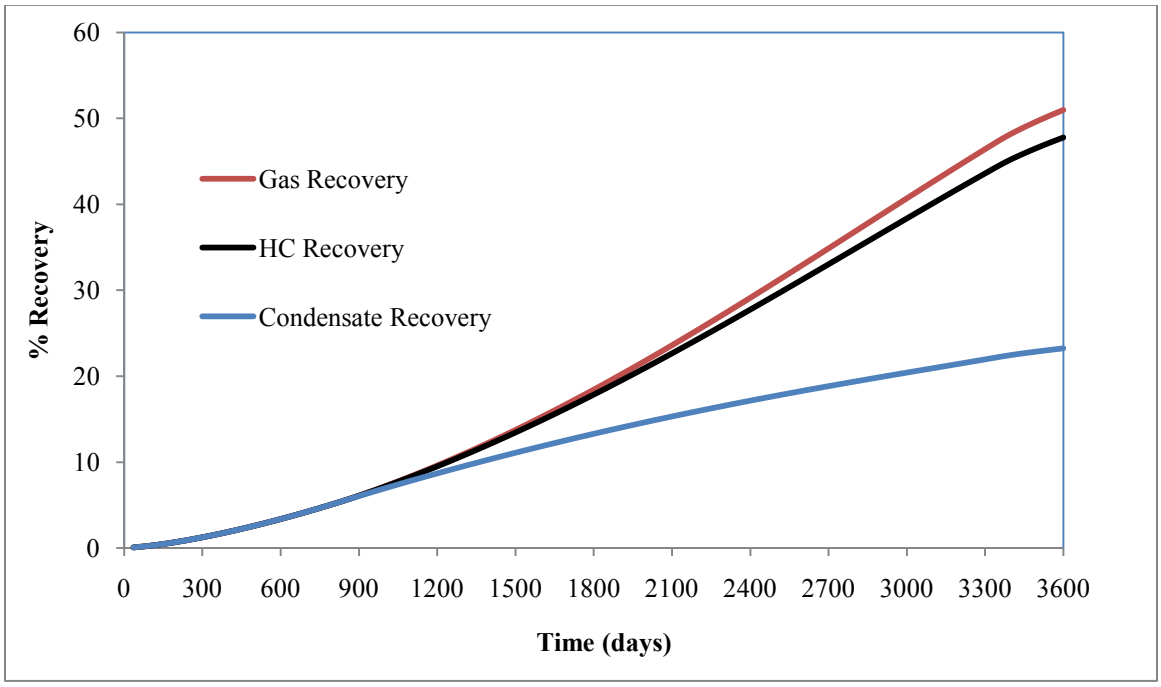

Figure 5.31: Recoveries obtained using Fluid C compositional combination with capillary pressure activated using λ =3

Understanding the effect of capillary pressure on the distribution of fluids requires that we look closer at the fluid movement during the appearance of condensate. Since the maximum capillary pressure obtained in Figure **5.28** is about 1.3 psia, it can be seen that the effect of such pressure would not be effective for a long period such as 10 years. Thus, the effect of pressure may only be visible during the first couple months after the condensate starts forming and picks mobility. Once the condensate is mobile and movements between condensate and gas start to take place, it would be very clear to make the conclusion of whether there would be a capillary pressure effect or not.

Figure **5.32** to Figure **5.41** present the condensate saturation profile between 800 days, which is 28 days before saturation pressure is reached, and 1100 days. The figures show the trend of condensate accumulation with distance as time progresses taken at the center of the matrix block and as shown in Figure **5.32**. The purpose of those figures is to compare the saturation accumulation profile while activating the capillary pressure effect to the saturation accumulation profile with zero capillary pressure. Figure **5.33** and Figure **5.34** show a compiled comparison of all the data collected versus distance. The plots mimic each other exactly, where they show the condensate saturation goes from zero to a maximum value of 0.16. Although the plots are crowded and might hide some trends at the early times of condensate formation, Figure **5.35** to Figure **5.41** split the saturation profile in pairs in order to make the comparison more visible as time progresses for the specified period. Figure **5.35** presents the saturation profile at 800 days and 828 days, at which the saturation pressure is reached. The same plot shows the saturation profile for zero capillary pressure and with the capillary pressure activated while condensate has not formed in sufficient quantities yet. Figure **5.36** and Figure **5.37** show the saturation profile at 850 days and 900 days for zero capillary and with the activation of capillary pressure. In both cases the condensate saturation progresses up to 0.084. Since the critical saturation of condensate is 0.08, toward the end of 900 days, condensate starts to be mobile. Overall, the performance of both examples is the same and showing no effect by the capillary pressure at the early stages of condensate forming. Figure **5.38** and Figure **5.39** illustrate the progress of oil saturation as it start to be mobile from 0.084 to 0.14 between 950 days and 1000 days. The observation shows no distinguishable differences between the two figures at the specified period. Furthermore, Figure **5.40** and Figure **5.41** show that the saturation profile of condensate starts to overlap as time progress further away from the time condensate starts to form. The overlap seems to indicate no influence is exerted by capillary forces on the flow of fluids within the system.

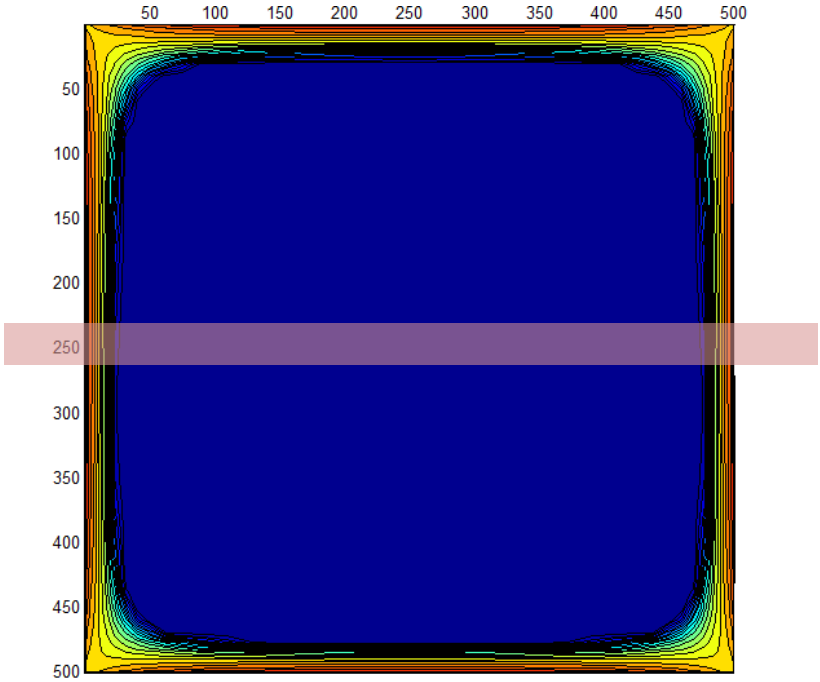

Figure 5.32: Condensate saturation profile at 1200 days for Fluid C using λ =3

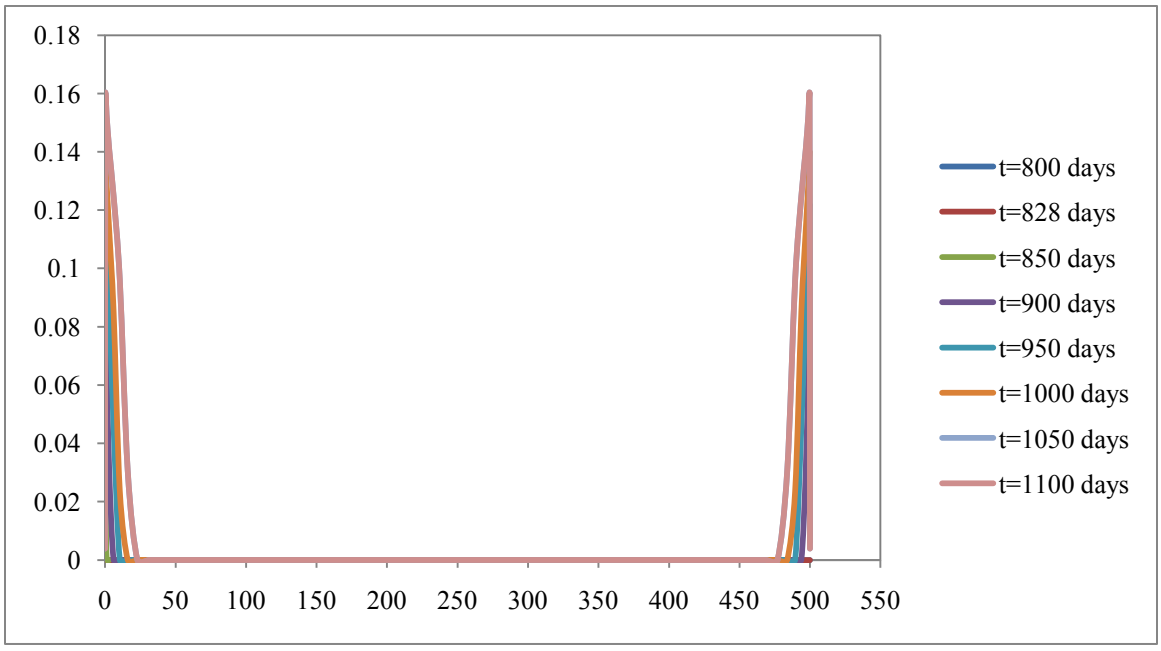

Figure 5.33: Saturation accumulation for Fluid C at 800-1100 days with zero capillary pressure

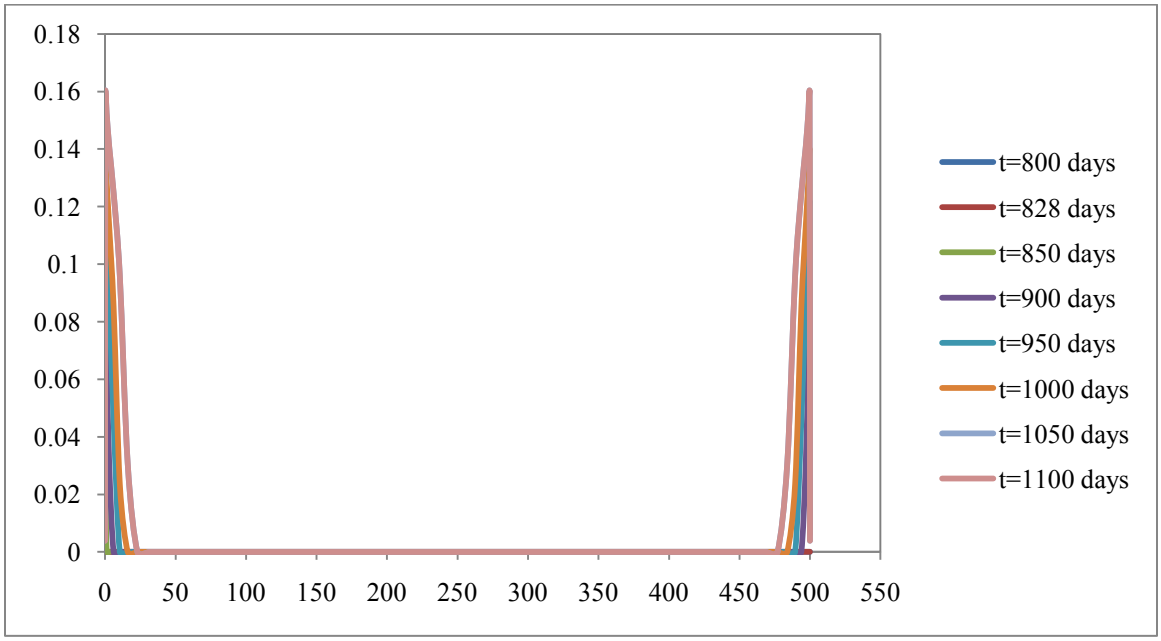

Figure 5.34: Saturation accumulation for Fluid C at 800-1100 days with capillary pressure activated using λ =3

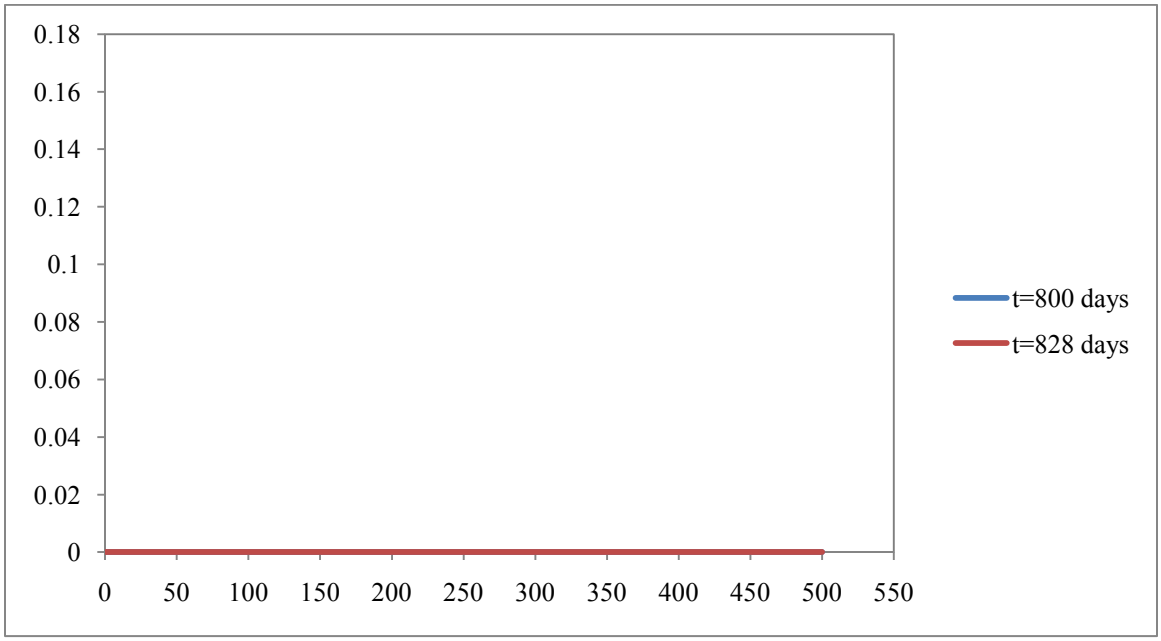

Figure 5.35: Saturation accumulation for Fluid C as saturation pressure is reached

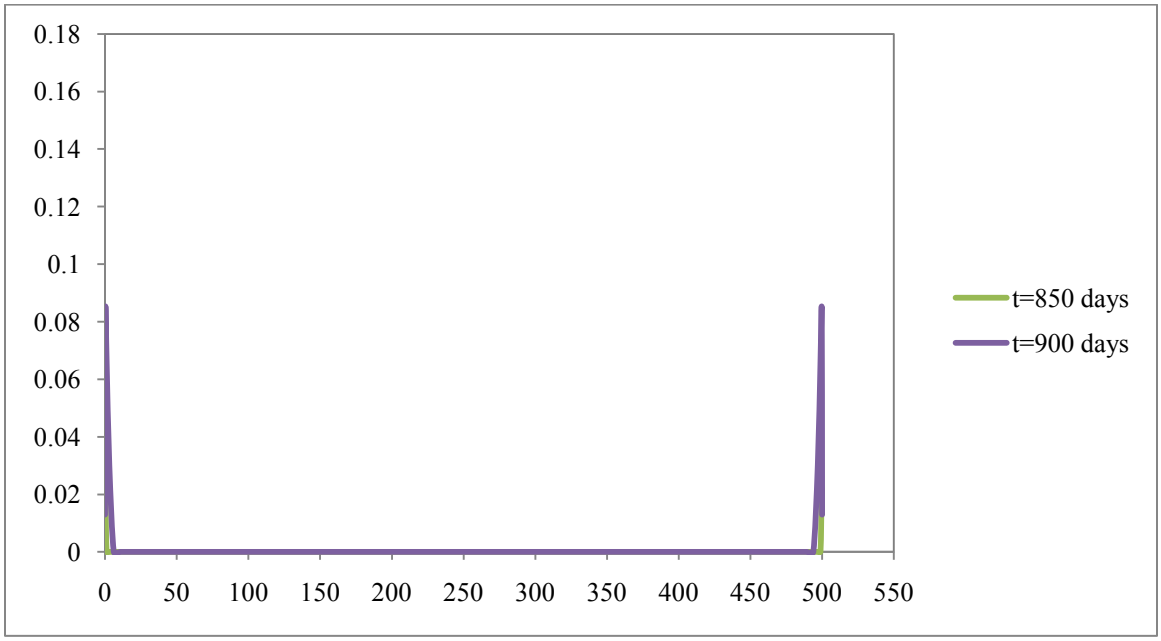

Figure 5.36: Saturation accumulation for Fluid C at 850-900 days with zero capillary pressure

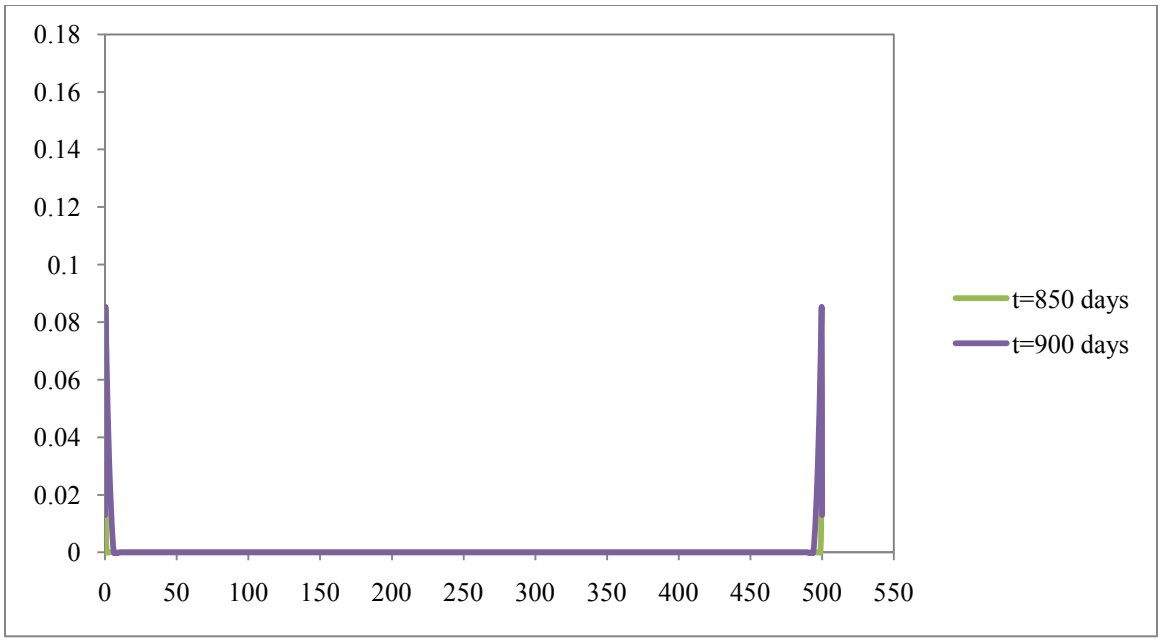

Figure 5.37: Saturation accumulation for Fluid C at 850-900 days with capillary pressure activated using λ =3

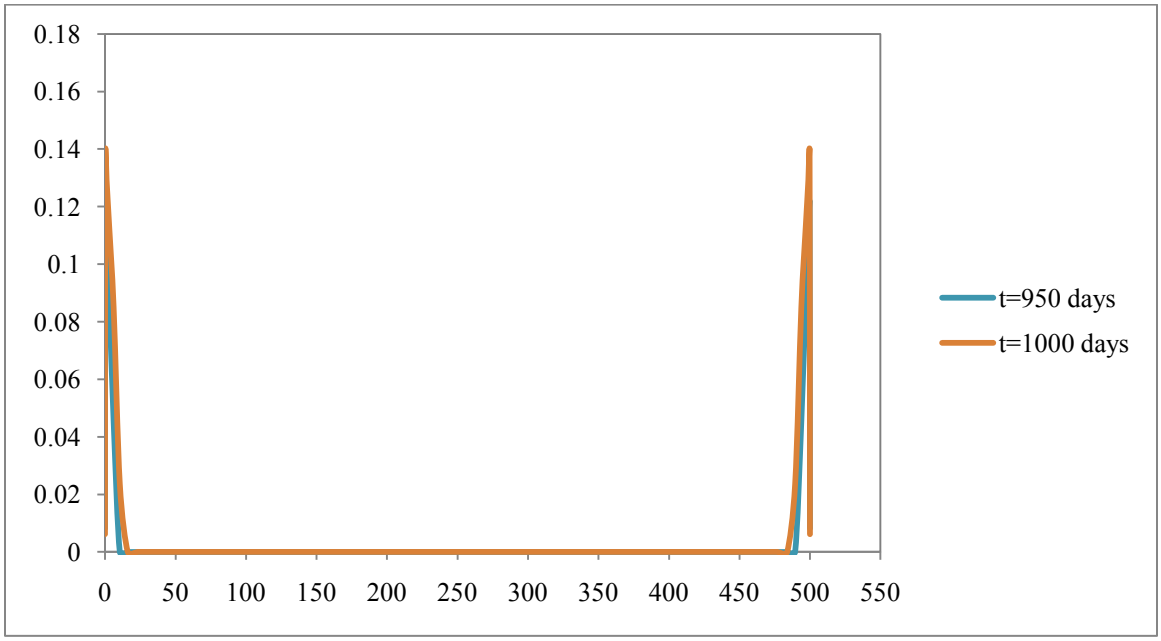

Figure 5.38: Saturation accumulation for Fluid C at 950-1000 days with zero capillary pressure

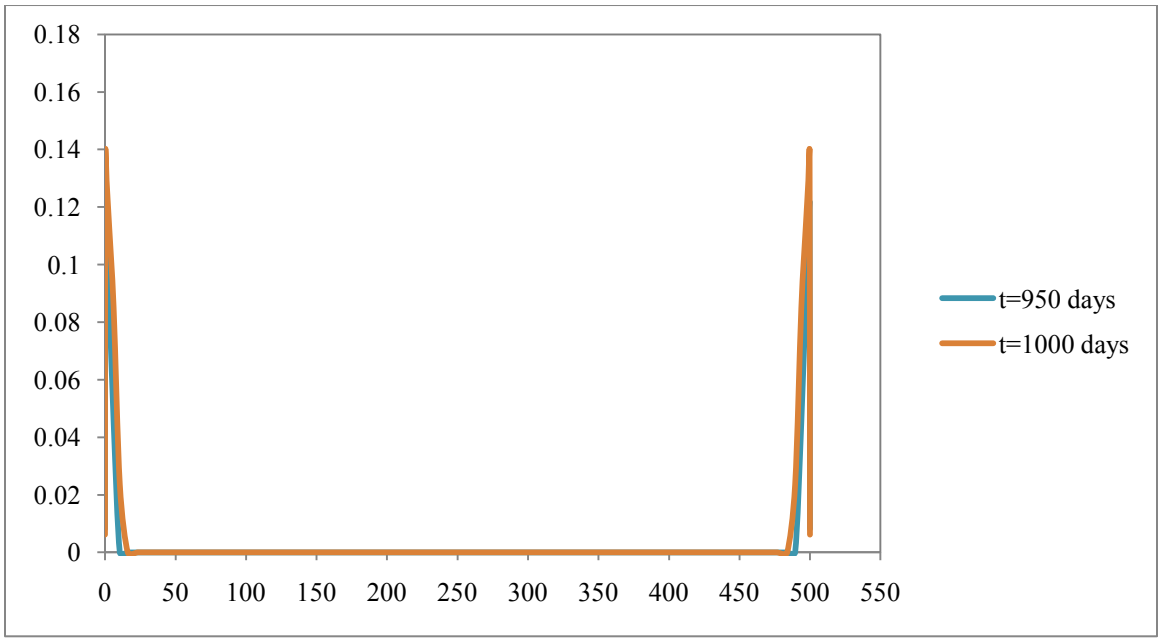

Figure 5.39: Saturation accumulation for Fluid C at 950-1000 days with capillary pressure activated using λ =3

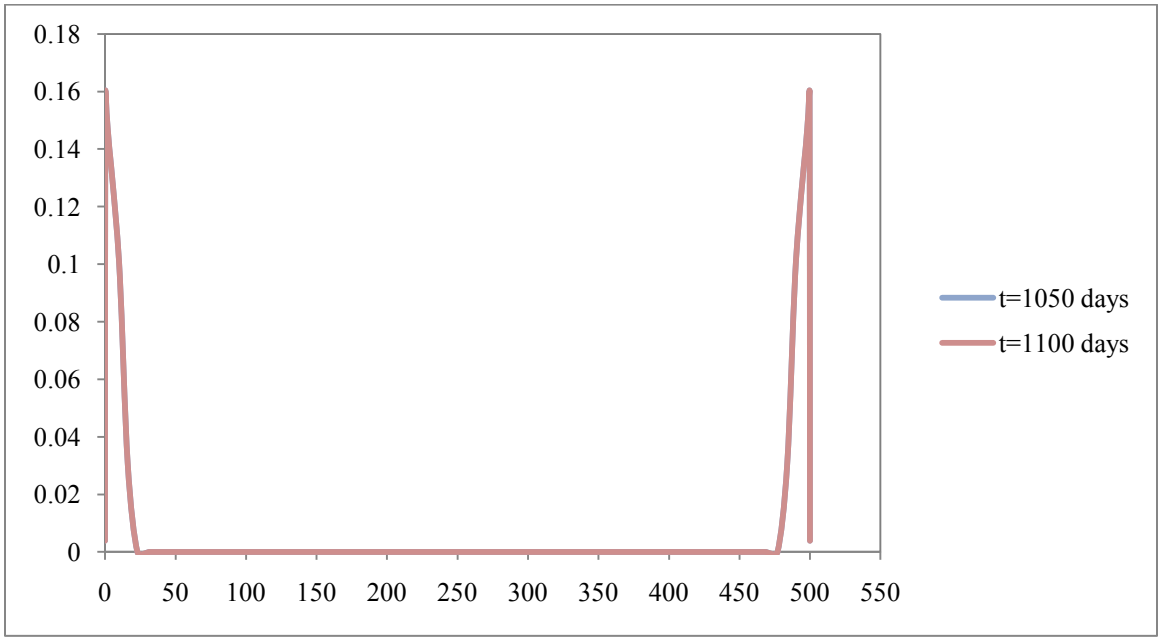

Figure 5.40: Saturation accumulation for Fluid C at 1050-1100 days with zero capillary pressure

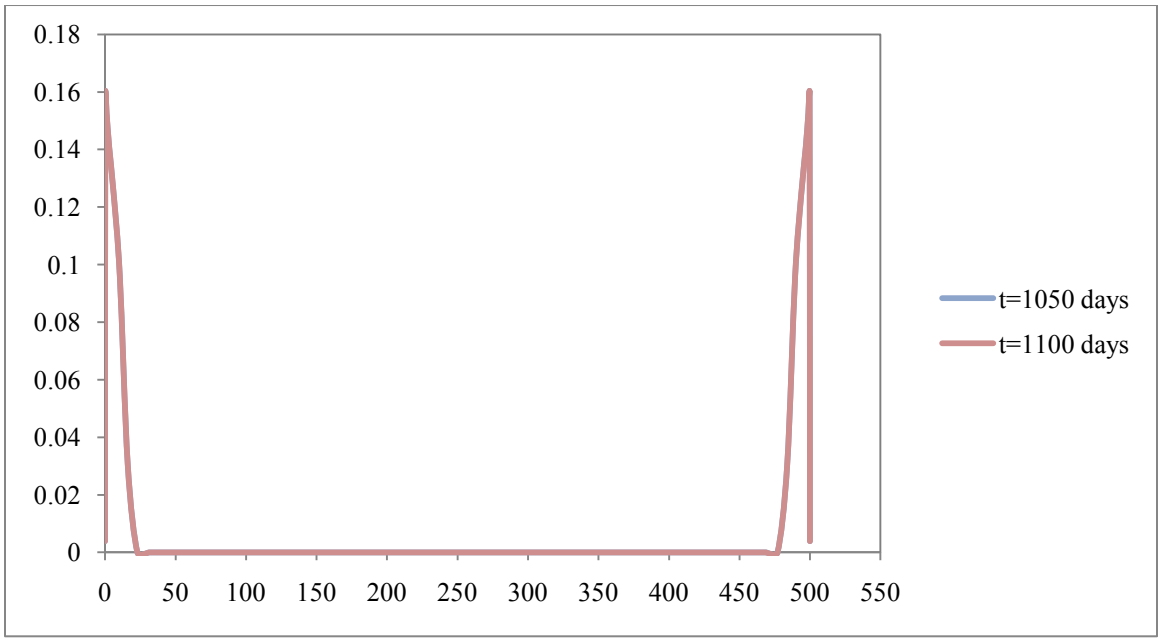

Figure 5.41: Saturation accumulation for Fluid C at 1050-1100 days with capillary pressure activated using $\lambda = 3$

In this section, the influence of capillary pressure effects on the behavior of gas-condensate reservoirs with intermediate condensate content was analyzed. Brooks and Corey's model was selected to represent the capillary pressure curves. The selected interactive model were used to test various values of the distribution index in order to indicate the range of reliable distribution index values to be associated with the current model.

Using the same conditions applied to the different composition concentration earlier; the total recovery, appearance of condensate in different regions of the matrix block, and the condensate saturation profile were analyzed. The analysis included comparing the behavior of the fractured gas-condensate reservoir after the activation of the capillary pressure using several capillary pressure curves. The results showed similar behavior in terms of fluid distribution, movement, and recovery, indicating that the behavior of fluids behaves the same even after the activation of capillary pressure effect.

Furthermore, a closer look has been considered to see the effect of capillary pressure on the distribution of fluids during the early times of condensate formation. It was believed that the effect of capillary pressure may only be visible during the first couple months after the condensate starts forming and picks mobility. Nevertheless, no differences between all the compiled results in terms of condensate saturation profiles were observed. The accumulation of condensate appears to progress smoothly on the sides of the block regardless of the capillary pressure values. As a result, it is concluded that the capillary pressure has no effect on the distribution of fluids and that the capillary pressure can be neglected for the system and conditions under consideration.

5.5 Effect of relative permeability on productivity

The relative permeabilities are the most important parameters in determining the productivity of gas-condensate reservoirs especially as condensate starts to form when the bottom hole pressure falls below the dew point. The determination of the relative permeability based on the near-well conditions, requires the understanding of the relationship between gas and oil relative permeabilities. Unfavorably, the condensate will continue to accumulate and cause condensate banking. According to Bang *et al.* (2006), condensate banking can reduce productivity of gas-condensate reservoirs by a factor of 2 to 4. Thus, the deliverability of gas-condensate reservoirs in such conditions is controlled by the transport properties, which are the relative permeabilities and capillary pressures between the fluids at the pore-scale.

Capillary pressure effects were addressed in the previous section and the analysis revealed insignificant impairment and/or enhancements in terms of fluid distribution and recoveries. Thus, the relative permeability has been put under investigation to measure the influence on productivity and condensate movement in the reservoir.

The relative permeability can be determined based on the capillary pressure through many ways. One of the general forms of calculating the relative permeability of the wetting and non-wetting phase is the Burdine Model (1953), which was developed to calculate the relative permeabilities using capillary pressures. The Burdine Model involves two equations represented with a tortuosity factor; the wetting phase relative permeability as shown in equation (2.9a), and the non-wetting phase relative permeability as illustrated by equation (2.10a). The application of the Burdine Model is utilized in the work of Brook-Corey (1966) and recently in the work of Li (2004). The Brook-Corey (1966) utilized the capillary pressure equation that they developed and derived general representative permeability equations by substituting the capillary pressure equation (2.5) into equation (2.9a) and (2.10a). The wetting and non-wetting equations shown in equations (2.11) and (2.12) were developed based on the Burdine Model with the assumption that the equilibrium saturation of the non-wetting phase is zero ($S_e = 0$).

Unfavorably, the relative permeability curves obtained using the Brooks and Corey's equation and the Li's equation consistently yielded very low oil-gas relative permeability as shown in Figure **5.42**. Looking closely at the equations for the relative permeability, the major variable that could improve the oil-gas relative permeability curve would be the pore size distribution index denoted by (λ). Several values had been used to address the fracture parameter to influence the position of the oil-gas relative permeability curve, but its influence was found to be two small. A representative relative permeability using the Brooks and Corey could have helped in coupling of the effect of capillary pressure with the relative permeability through the distribution index value. Unfortunately, this was not achieved and thus a modified form of calculating the relative permeabilities was used to represent the relationship between oil and gas. Equations (5.1) and equation (5.2) present a modified Corey's function which is equipped with van Genuchten's (1980) fracture parameter (λ) to calculate the oil and gas relative permeabilities. The van Genuchten's fracture parameter controls the shape of the oil relative permeability curve. In this exercise, several values were used for the fracture parameter as illustrated by Figure **5.43**. The constraint used to pick the values were to not reach a straight line oil relative permeability curve and also stay in the oil-wet region of the plot.

$$k_{ro} = \sqrt{S_o^*}\left\{1 - \left[1 - (S_o^*)^{\frac{1}{\lambda}}\right]^{\lambda}\right\}^2 \tag{5.1}$$

$$k_{rg} = (1 - S_o)^2 - (1 - S_o^2) \tag{5.2}$$

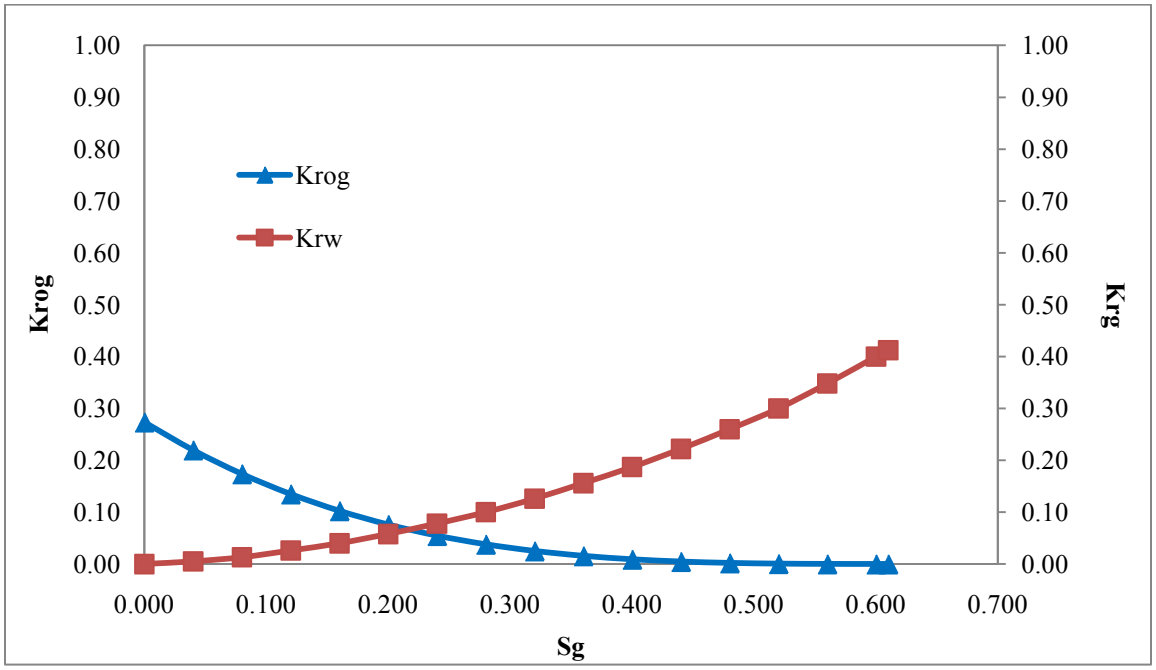

Figure 5.42: Relative permeability representation by Brooks and Corey's and Li's models

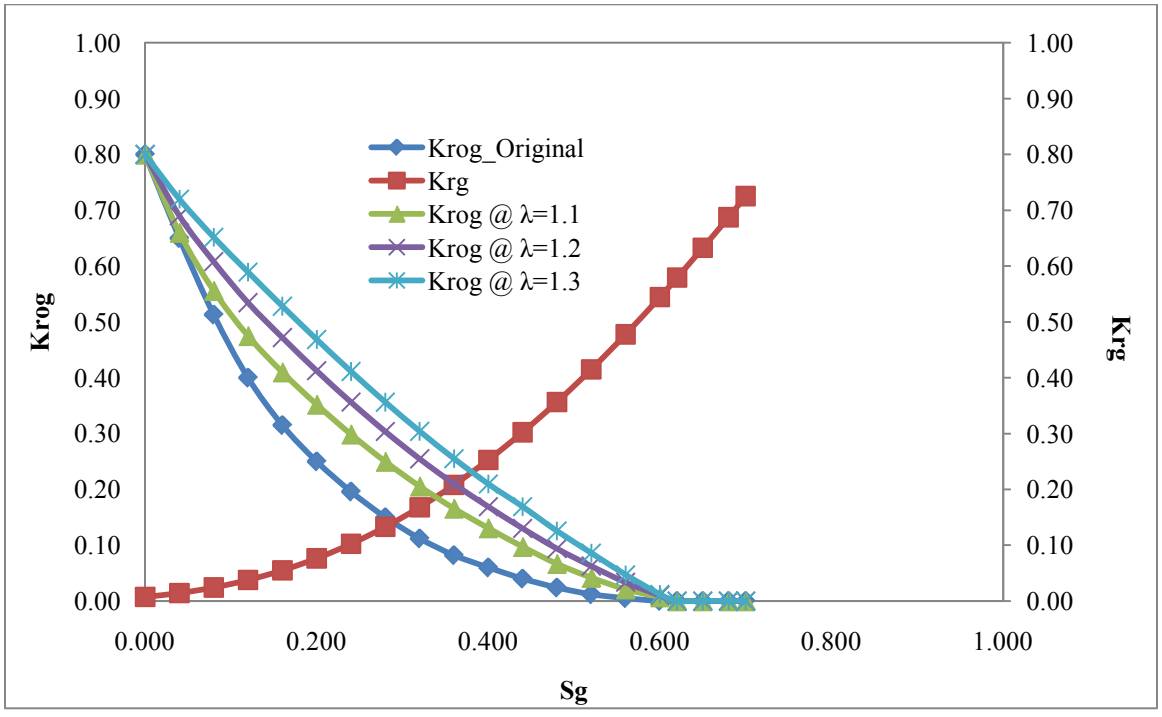

Figure 5.43: Relative permeability model representation using modified Corey's function

Using the same conditions applied to the different compositional concentrations earlier, total recoveries were studied. The analysis included comparing the behavior of the fractured gas-condensate reservoir using different relative permeability curves and comparing the performance to the original relative permeability curve used in this study. Figure **5.44** to Figure **5.46** show the effect of relative permeability on the coating of condensate for the lighter, intermediate, and heavier condensate content fluids. Figure **5.44** displays the condensate saturation evolution for Fluid A using different relative permeability curves. The condensate coating (Figure 5.44) has a slight increase in thickness compared to the condensate saturation profile using the original relative permeability curves shown in Figure **5.15**. The slight increase is related to the low condensate content of Fluid A. Similar influence is observed using the different relative permeability curves for Fluid A, where condensate evolution is enhanced and revaporization occurs earlier in the life of the reservoir.

Figure **5.45** demonstrates the condensate saturation evolution for Fluid C using different relative permeability curves. The condensate coating (Figure 5.45) displays a considerable increase in thickness compared to the condensate saturation profile using the original relative permeability curves shown in Figure **5.11**. The thickness increases as a function of time and as the condensate accumulation increases for Fluid C. The different relative permeability curves for Fluid C enhances the condensate evolution as the condensate relative permeability curve moves upward. Condensate revaporization is notable at the corners of the matrix block at 2000 days and at the sides of the matrix as time reaches 2500 days (Figure **5.45**).

Figure **5.46** shows the condensate saturation evolution for Fluid E using different relative permeability curves. The condensate coating exhibits a significant increase in thickness compared to the condensate saturation profile using the original relative permeability curves shown in Figure **5.26**. Thickness of condensate coating becomes more significant as condensate content increases in the matrix block as shown in Figure **5.46** at 900 days and 1200 days. The observed increase in thickness is related to the richness of heavy components in Fluid E. With the increase of condensate content, the condensate evolution for Fluid E increases considerably as the condensate relative permeability curve moves upward. Condensate evolution is represented with faster prorogation toward the inner of the matrix block and earlier revaporization near the fracture network (Figure **5.46**).

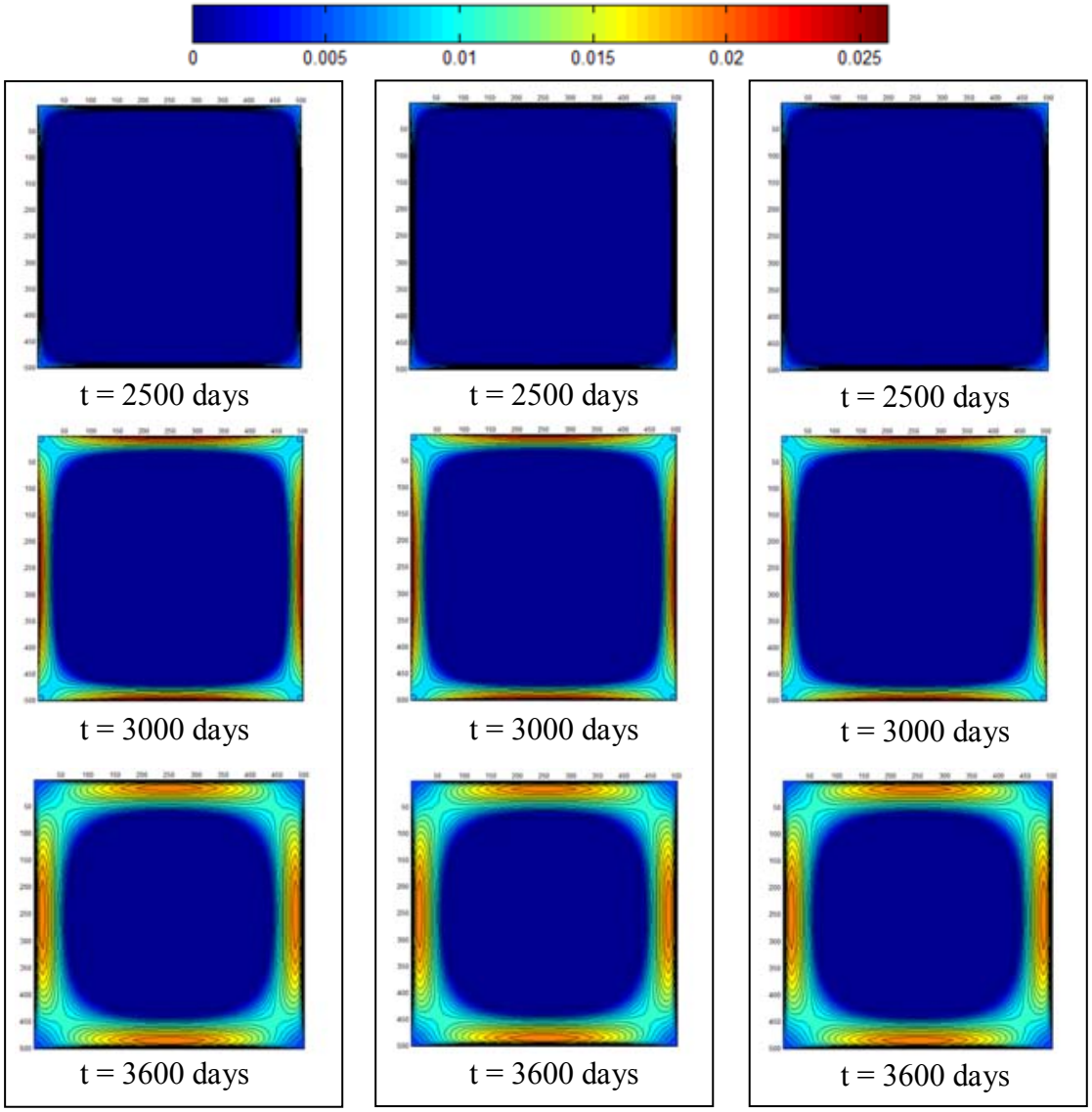

Figure 5.44: Condensate evolution for Fluid A using different relative permeability curves

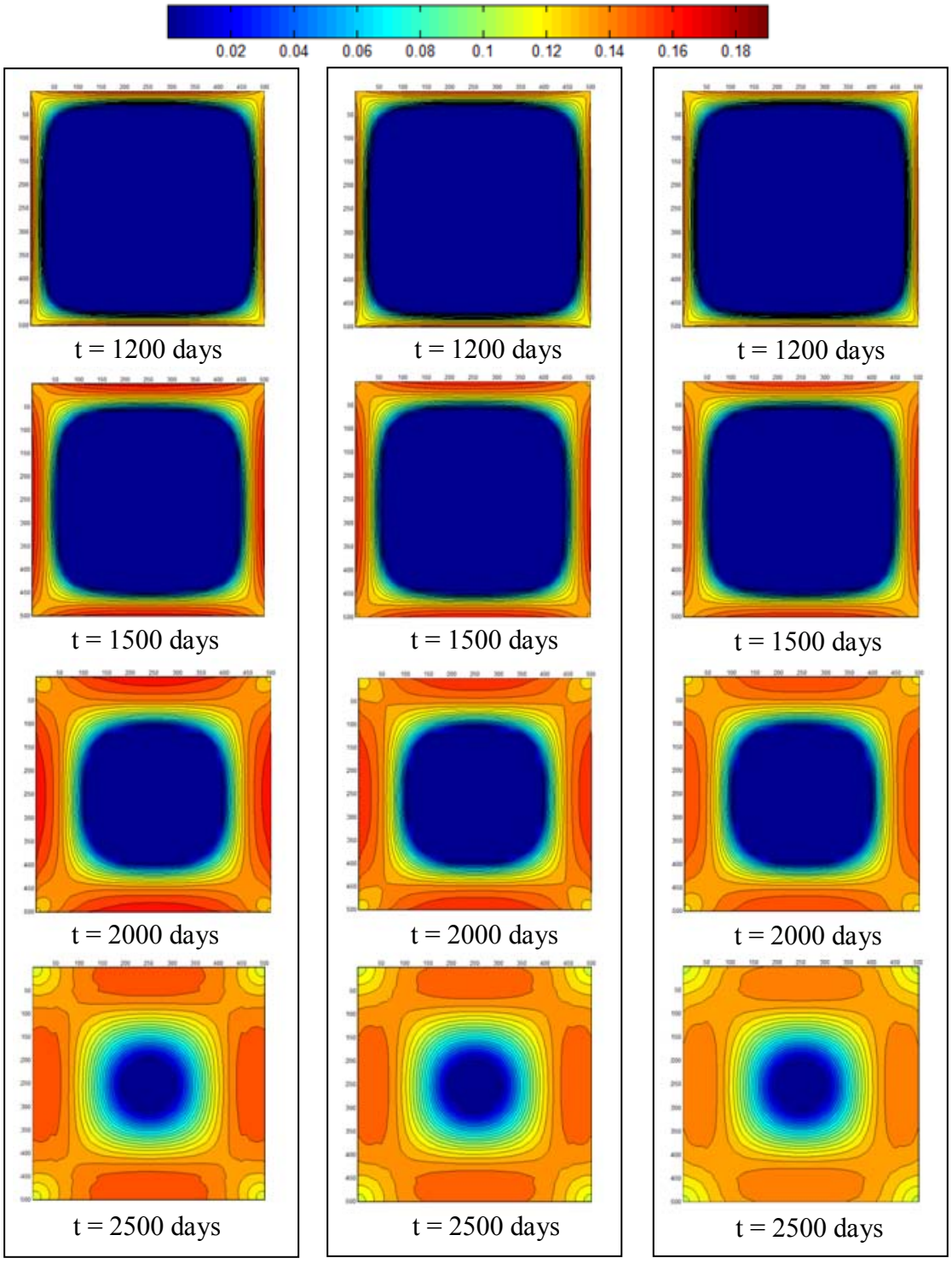

Figure 5.45: Condensate evolution for Fluid C using different relative permeability curves

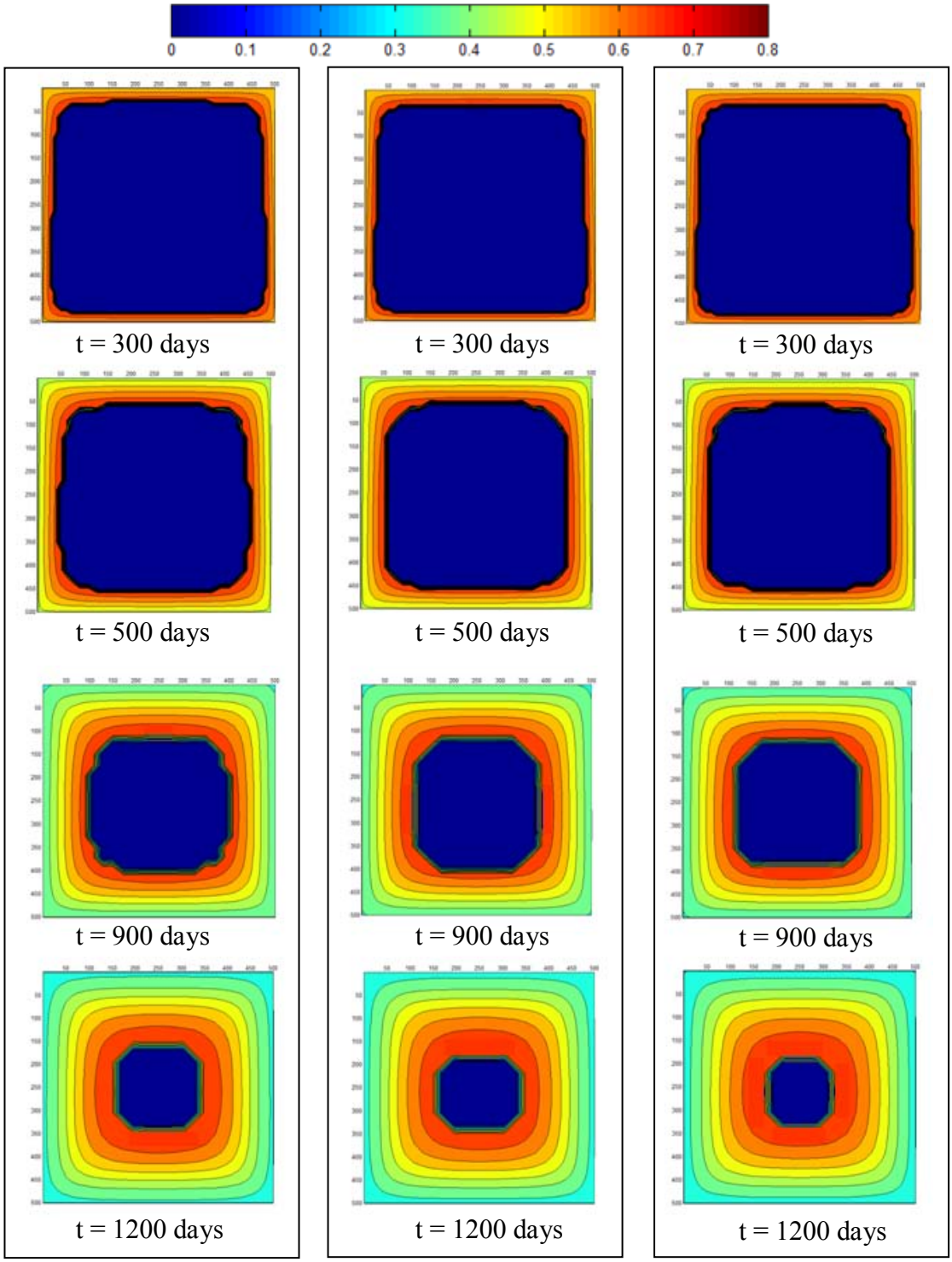

a. λ = 1.1 b. λ = 1.2 c. λ = 1.3

Figure 5.46: Condensate evolution for Fluid E using different relative permeability curves

In addition, the analysis included comparing the recoveries of the fractured gas-condensate reservoir using different relative permeability curves and comparing the performance to the original relative permeability curve used in this study. Table **5.9** shows the general recoveries of the five different composition fluids used under the condition of the original relative permeability curve.

Table 5.9: Recoveries of the five gas-condensate fluids using original relative permeability curves

	OGIP MMSCF	OCIP MSTB	OHIP lb/mole	Recovery (%)		
				Gas	Condensate	Hydrocarbon
Fluid A	776.21	51.74	2190815.81	53.38	49.53	53.14
Fluid B	753.20	87.72	2218874.60	52.20	34.48	50.38
Fluid C	737.87	113.10	2216311.13	50.93	23.14	47.71
Fluid D	694.91	168.39	2182677.05	46.32	14.48	41.49
Fluid E	659.78	204.56	2140187.11	44.24	14.66	38.90

Table **5.10** to Table **5.16** display the recoveries of the five sets as different relative permeability curves are used. Table **5.10** represents the recoveries of Fluid A, which indicates no changes as different relative permeability curves are used because there is less condensate to be controlled by the oil-gas relative permeability changes. The hydrocarbon using Fluid A contains lighter components rather than heavier components, which mean that gas phase should dominates the fluids in the reservoir. However, there is about 1.16% increase in the overall recovery of gas, condensate, and hydrocarbon at surface conditions due to the low impairment of condensate which was influenced by the increase of condensate relative permeability.

Table 5.10: Recoveries for Fluid A using different relative permeability curves

Rel. Perm Condition	Fluid A: Recovery (%)		
	Gas	Condensate	Hydrocarbon
$\lambda = 1.1$	62.16	57.83	61.88
$\lambda = 1.2$	62.16	57.83	61.88
$\lambda = 1.3$	62.16	57.83	61.88

Table **5.11** lists the recoveries of Fluid B, which indicates insignificant increase as different relative permeability curves are used. It is also due to the low condensate content in the reservoir and that there is less control applied by the change of oil-gas relative permeability curves. The results of this case shows that there is an average of 1.15% increase in the overall recovery of gas, condensate, and hydrocarbon at surface conditions which is also due to the low impairment of condensate.

Table 5.11: Recoveries for Fluid B using different relative permeability curves

Rel. Perm Condition	Fluid B: Recovery (%)		
	Gas	Condensate	Hydrocarbon
$\lambda = 1.1$	59.07	40.01	57.11
$\lambda = 1.2$	59.08	40.10	57.13
$\lambda = 1.3$	59.09	40.15	57.14

As the condensate content of the fluids in place increases, more condensate is expected to form in the reservoir as well as condensation at surface. Table **5.12** displays the results using the moderate case (Fluid C) which shows an increase in recoveries as the relative permeability curve moves upward. The increase is a result of the increase in condensate contents in the reservoir and as a result of the increase of heavy components in the fluid. The more condensate is present, the more the influence of relative permeability changes will be present since the changes are only applied to the oil-gas relative permeability curve. The recoveries for Fluid C show an average

increase of about 1.13% for gas and hydrocarbon, while for condensate it is; 1.20%, 1.25%, and 1.29% for the different relative permeability curves respectively.

Table 5.12: Recoveries for Fluid C using different relative permeability curves

Rel. Perm Condition	Fluid C: Recovery (%)		
	Gas	Condensate	Hydrocarbon
$\lambda = 1.1$	56.76	27.80	53.41
$\lambda = 1.2$	56.93	28.92	53.69
$\lambda = 1.3$	57.09	29.91	53.95

Considering the last two sets of Table **5.8** denoted as Fluid D and Fluid E, which consist mainly of heavy components and few light ends, higher condensate volumes are expected to form at reservoir conditions as the dew point pressure is reached. Table **5.13** indicates the recoveries of Fluid D using different relative permeability curves. It is clear from Table **5.13** that the increase in recoveries for condensate is more significant as the condensate relative permeability shifts upward. The increase of recoveries of gas, condensate, and hydrocarbon is as shown in Table **5.14**.

Table 5.13: Recoveries for Fluid D using different relative permeability curves

Rel. Perm Condition	Fluid D: Recovery (%)		
	Gas	Condensate	Hydrocarbon
$\lambda = 1.1$	52.25	19.84	47.28
$\lambda = 1.2$	52.80	22.18	48.11
$\lambda = 1.3$	53.34	24.51	48.93

Table 5.14: Increase in recoveries for Fluid D using different relative permeability curves

Rel. Perm Condition	Fluid D: Recovery Increase (%)		
	Gas	Condensate	Hydrocarbon
$\lambda = 1.1$	1.13	1.37	1.14
$\lambda = 1.2$	1.14	1.53	1.16
$\lambda = 1.3$	1.15	1.69	1.18

As the concentration of the heavy components becomes larger, the amount of condensation appears early in the simulation and as a result revaporization of condensate will also take place earlier than anticipated in moderate cases. Table **5.15** represents the recoveries of Fluid E using different relative permeability curves. Table **5.15** indicates an increase in the overall recoveries but not as much as the increase obtained using Fluid D. This can be explained due to larger amount of condensation in Fluid E; where more heavy components are lost to the formation and some of the condensate revaporizes, which eventually decreases the amount of condensate recovery at surface conditions. Table **5.16** indicates the increase in recoveries using Fluid E, which is less than Fluid D as indicated by the loss of heavy components to the formation.

Table 5.15: Recoveries for Fluid E using different relative permeability curves

Rel. Perm Condition	Fluid E: Recovery (%)		
	Gas	Condensate	Hydrocarbon
$\lambda = 1.1$	50.07	19.30	44.52
$\lambda = 1.2$	50.72	21.65	45.48
$\lambda = 1.3$	51.24	23.93	46.33

Table 5.16: Increase in recoveries for Fluid E using different relative permeability curves

Rel. Perm Condition	Fluid E: Recovery Increase (%)		
	Gas	Condensate	Hydrocarbon
λ = 1.1	1.13	1.32	1.14
λ = 1.2	1.15	1.48	1.17
λ = 1.3	1.16	1.63	1.19

As the condensate accumulate in the matrix blocks near the production channels, the deliverability of gas-condensate reservoirs is controlled by the transport properties, which are the relative permeabilities of oil and gas. The major variable that enhanced the oil-gas relative permeability curve was the fracture parameter (λ) obtained by van Genuchten's (1980) to calculate the oil and gas relative permeabilities. Several values had been used to address the fracture parameter to influence the position of the oil-gas relative permeability curve. As demonstrated by Table **5.11** to Table **5.16**, it appears that the influence depends on the amount of condensate content in the reservoir. The more condensation that takes place, the more influence is applied by the relative permeability curves. The increase in overall recoveries obtained by the different relative permeability compared to the original relative permeability curves used were in the range of 1.14% to 1.69% based on the composition set used. Nevertheless, the changes in recoveries are not significant enough that will change the reservoir performance dramatically. It could be concluded, that the influence of relative permeability is moderate and is controlled by the amount of condensate in place and the steepness of the relative permeability curves.

Furthermore, the deliverability of gas-condensate reservoirs can be altered by increasing the permeability of the matrix. The overall flow of fluids using moderate tight matrix permeability such as 0.01 md, is expected to be higher than with a permeability of 0.001 md as used throughout this work. The increase of fluid flow is related to the enhancement in mobility, which has improved by the increase of matrix permeability as indicated by equation (5.3).

$$Mobility = \frac{k \,.\, k_{rf}}{\mu_f} \quad ; \quad f = o, or\ g \qquad (5.3)$$

Figure **5.47** to Figure **5.49** display the results obtained from the numerical study using a moderate tight matrix permeability of 0.01 md. Figure **5.47** presents the recovery of gas, molar hydrocarbon, and condensate using the compositional combination of Fluid C. The recovery behavior of the given gas-condensate system is showing higher recoveries, which means that fluids are allowed to flow more freely to the surface. At the end of 10 years of production and under a fracture depletion condition of 1 psi/day; recoveries of gas, molar hydrocarbon, and condensate from the original fluid in place are determined to be 79.71%, 74.80%, and 37.27% respectively. The values indicate that the competition for flow paths had been reduced by the increase in matrix permeability. As a result, more flow is allowed to go through pore throats, which had reduced the effect of condensate impairment. In this case, the mobility of gas and condensate are both significant, and the deliverability is controlled by the fracture boundary conditions.

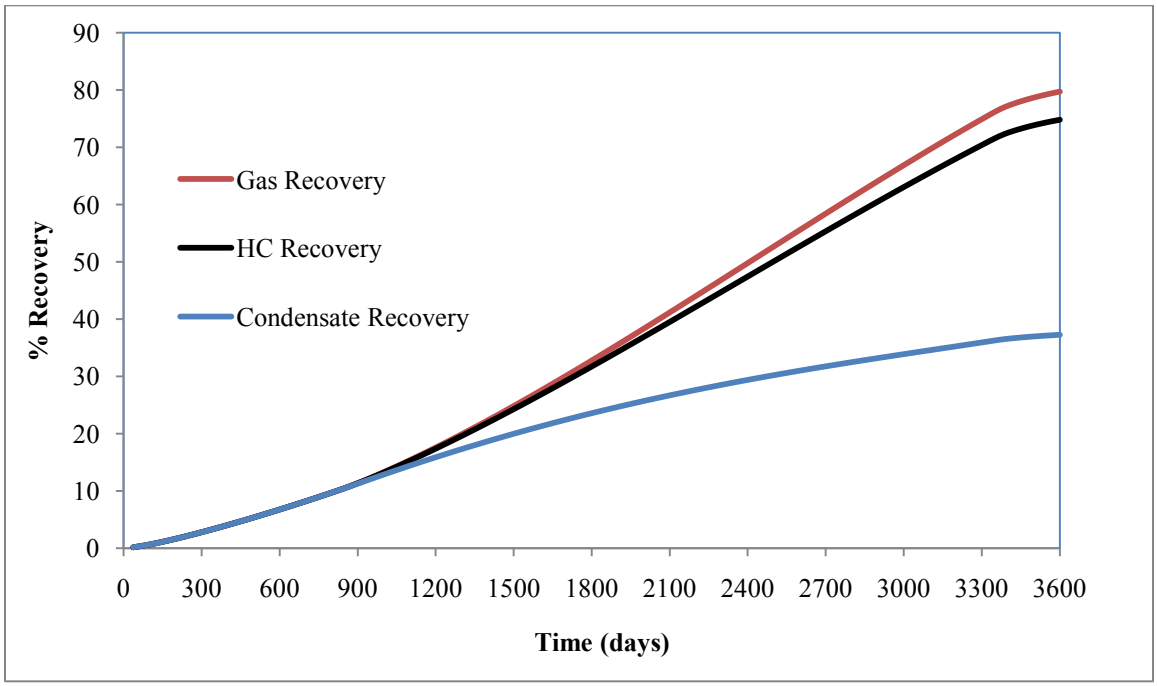

Figure 5.47: Gas and condensate recoveries for Fluid C with moderate tight matrix permeability

Since the mobility of fluids has been enhanced and more fluids are allowed to pass through the pore throats with less impairment, the appearance of condensate is significant at different parts of the matrix. Figure **5.48** represent the appearance of condensate at the top, middle, and bottom of the matrix block in order to track the propagation of condensate. The trends of the condensate appearance curves appear very close to each other, which mean that the higher matrix permeability is allowing the condensate to propagate more easily throughout the matrix block. Although the condensate is spread in the matrix block, the impairment is less significant compared to the tight matrix permeability used earlier since more fluids are allowed to flow through the pore throats.

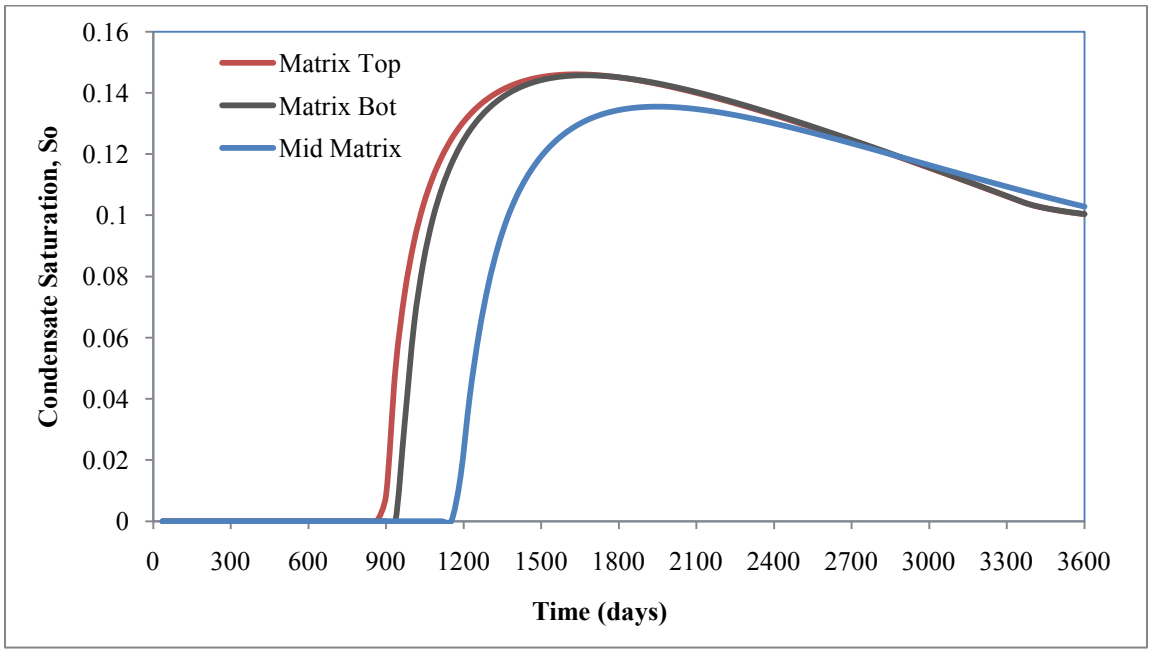

Figure 5.48: Condensate evolution for Fluid C with moderate tight matrix permeability

Figure **5.49** represents the condensate content for Fluid C which is initiated at 153.3 bbl/MMSCF and maintained until condensate forms in the reservoir. The condensate content of gas in place and the condensate content in the well stream is very close to each other after the saturation pressure is reached, which means that the fluid in place is not losing significant amount of heavy components to the formation. The illustration represent that the higher permeability used in this case allow no significant changes in composition of gas and condensate as the dew point is reached.

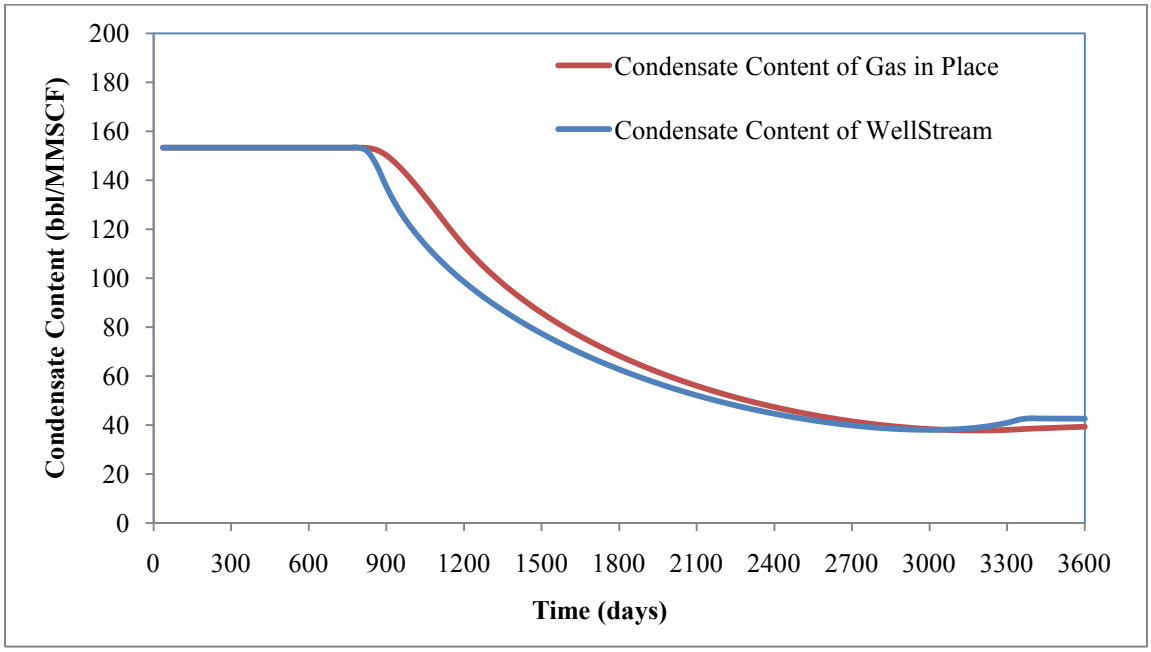

Figure 5.49: Condensate content changes for Fluid C with moderate tight matrix permeability

Using the same conditions applied using Fluid C with the moderate tight matrix permeability; the behavior of the fractured gas-condensate reservoir is analyzed using different relative permeability curves. The analysis includes comparing the performance to the original relative permeability curve used in this study. Table **5.17** shows the general recovery for Fluid C under the conditions of the original relative permeability curve.

Table 5.17: Recoveries for Fluid C with moderate tight matrix permeability and original relative permeability curve

	OGIP MMSCF	OCIP MSTB	OHIP lb/mole	Recovery (%) Gas	Condensate	Hydrocarbon
Fluid C	614.89	94.25	1846925.94	79.71	37.27	74.8

Table **5.18** displays the results under different relative permeability conditions, which shows an increase in recoveries as the relative permeability curve moves upward. The increase is a result of the increase in condensate contents in the reservoir and as a result of the increase of heavy components in the fluid. The more condensate is present, the more the influence of relative permeability changes will be present since the changes are only applied to the oil-gas relative permeability curve. The recoveries of Fluid C show an average increase of about 1.02% for gas, 0.55% for condensate hydrocarbon, and 2.06% for condensate using different relative permeability curves.

Table 5.18: Recoveries for Fluid C with moderate tight matrix permeability and different relative permeability curves

Rel. Perm Condition	Fluid C: Recovery (%)		
	Gas	Condensate	Hydrocarbon
$\lambda = 1.1$	81.24	76.55	39.93
$\lambda = 1.2$	81.27	76.59	40.91
$\lambda = 1.3$	81.29	76.72	41.77

The influence of relative permeability is related to the mobility equation presented by equation (5.3), which indicates that as the relative permeability increases the mobility will increase as well. In addition, higher permeability value for the matrix rock, allows more fluids to flow through pore throats which enhances deliverability. The same trends attained using Fluid C apply to all the composition sets used in this work since the mobility is constrained by the permeability and the relative permeability values. However, the recovery of fluids when using higher matrix permeability is constrained by the fracture depletion rate.

Chapter 6

CONCLUDING REMARKS

The productivity of gas-condensate reservoirs experiences a reduction in recovery due to the appearance of condensate near the wellbore, which in turn reduces the overall flow of hydrocarbons to the surface. In general, gas-condensate fluids are mixtures of hydrocarbon that are initially presented as gaseous components in the raw natural gas produced from natural gas fields. During the depletion of the reservoirs fluids, the gas condenses as the pressure of the reservoir reduces below the hydrocarbon dew point pressure, which introduces a liquid phase called retrograde condensate.

The phase behavior of the fluids in place impacts the production scheme of gas-condensate reservoirs, since the recovery of condensate is highly dependent on the changes in composition. In this study, the productivity of naturally fractured gas-condensate reservoirs was addressed using a compositional simulation model to examine the effect of capillary pressure on the recovery of gas-condensate fluids. The model was utilized to examine several scenarios of various compositional sets while activating capillary pressure effect to evaluate the productivity of gas-condensate reservoirs. In addition, the relative permeability effects were examined on the overall recovery of the fluids in place.

Several sets of composition combinations had been used for the analysis of the condensate coating on the edges of the matrix blocks. The purpose of this approach was to couple the severity of the hindering of gas flow by the appearance of condensate with the characteristics of the fluids in place. The results led to the conclusion that the saturation pressure point is controlled by the concentration of heavy components. The sooner the saturation pressure is reached, the sooner condensate appears and hinders the overall recovery of fluids. As an overall observation, as the condensate content of the in-situ fluids increase, more heavy components are lost to the formation and less recovery of condensate is achieved at surface because most of the gas produced is lean gas. Overall production is highest for in-situ fluids with the least condensate content because the appearance of condensate is not expected in the early life of the reservoir, and the gas is allowed to flow freely. In the contrary, reservoir fluids with large

condensate content showed lower surface productions especially for condensate since most of the components are lost to the formation and producing leaner gas to the surface.

Using the same conditions applied to the different composition concentration; the total recovery, appearance of condensate in different regions of the matrix block, and the condensate saturation profile were tested. The analysis included comparing the behavior of the fractured gas-condensate reservoir after the activation of the capillary pressure using several capillary pressure curves. Brooks and Corey's model was selected to represent the capillary pressure curves. The selected interactive model were used to test various values of the distribution index (1.5 to 7) in order to indicate the range of reliable distribution index values to be associated with the current model. Results showed similar behavior in terms of fluid distribution, movement, and recovery, indicating that the behavior of fluids behaves the same even after the activation of capillary pressure effect. Furthermore, the effect of capillary pressure on the distribution of fluids was analyzed during a short period of time as the condensate starts to form. Nevertheless, it appeared from the analysis that there are no significant effect and that the accumulation of condensate appears to progress smoothly on the sides of the block regardless of the capillary pressure effects for the ranges of capillary pressures under consideration.

Relative permeabilities proved to be the most important parameters in determining the productivity of gas-condensate reservoirs especially as condensate starts to form when the bottom hole pressure falls below the dew point. The major variable that enhanced the oil-gas relative permeability curve was the fracture parameter (λ) obtained by van Genuchten's (1980) to calculate the oil and gas relative permeabilities. Several values were used to address the fracture parameter to influence the position of the oil-gas relative permeability curve. As a result, it appeared that the influence depends on the amount of condensate content in the reservoir. The more condensation that takes place, the more influence is applied by the relative permeability curves. The condensate coating increases as a function of time and as the condensate accumulation increases in the matrix block. The thickness of condensate coating was much more considerable for the heavier condensate content reservoir fluids. The different relative permeability curves seem to enhance the condensate evolution as the condensate relative permeability curve moves upward. Condensate movement increases toward the inner of the matrix as well as earlier revaporization is notable at the edges of the matrix block. The increase in overall recoveries obtained by the different relative permeability compared to the original

relative permeability curves used were in the range of 1.14% to 1.69% based on the composition set used. Nevertheless, the changes in recoveries were not significant enough as to dramatically change reservoir performance.

Eventually, the variation of reservoir fluid distribution can be caused by many factors, production scheme, flow gradients, permeability of the matrix rock, and relative permeability of fluids in place. It is highly recommended for future work to activate diffusion forces in order to consider the multi-mechanistic flow concept introduced by Ertekin *et al.* (1986), which emphasized that the flow of fluids is driven by concentration or density gradients. It is also recommended to apply the same testing conditions using different matrix permeabilities other than a tight rock formation condition as used in this study. Activating diffusion forces and applying different matrix permeabilities might shed light to the effect of capillary forces on the distribution of fluids, which is believed to have a great relevance to the distribution of fluids in the reservoir.

BIBLIOGRAPHY

Ahmed, Tarek H.: *Reservoir Engineering Handbook*, Second edition, Gulf Professional Publishing Co, ISBN 0-88415-770-9, 2000.

Ansah, Joseph: *Production Rate and Cumulative Production Models for Advanced Decline Curve Analysis of Gas Reservoirs*. PhD Dissertation, Texas A&M University, 1996.

Arps, J. J.: *Analysis of Decline Curves*, Trans. AIME p. 160, 228-47, 1945.

Ayala, Luis F.: *Compositional Modeling of Naturally-Fractured Gas-Condensate Reservoirs in Multi-mechanistic Flow Domains*. PhD Dissertation, The Pennsylvania State University, 2004.

Ayala, Luis F., Ertekin, Turgay, and Adewumi, Michael: *Compositional Modeling of Retrograde Gas-Condensate Reservoirs in Multi-mechanistic Flow Domains*. SPE Paper 94856, SPE Journal, p. 480-487, December 2006.

Ayala, Luis F., Radespiel, Eduardo, and Ertekin, Turgay: *Numerical Analysis of Condensate-Flow Impairment in Retrograde-Gas Naturally Fractured Reservoirs and its Interplay with the Estimation of Diffusion Coefficients*. SPE Paper 107870, SPE Journal, p. 95-100, March 2009.

Bang, V., Kumar, V., Ayyalasomayajula, P. S., Pope, G. A., and Sharma, M. M.: *Relative Permeability of Gas-Condensate Fluids: A General Correlation*, SPE Paper 102741 presented at the 2006 SPE Annual Technical Conference and Exhibition held in San Antonio, Texas, September 2006.

Basbug, B. and Karpyn, Z. T.: *Determination of Relative Permeability and Capillary Pressure Curves Using an Automated History-Matching Approach,* SPE Paper 117767 presented at the 2008 SPE Eastern Regional/AAPG Eastern Section Joint Meeting held in Pittsburgh, Pennsylvania, October 2008.

Batycky, Rod P., Thiele, Marco R., Coats, K.H., Grindheim, Alan, Ponting, Dave, Killough, John E., Settari, Tony, Thomas, L. Kent, Wallis, John, Watts, J.W., and Whitson, Curtis H.: *Reservoir Simulation*, SPE Petroleum Engineering Handbook, Volume 5, Chapter 17, Editor: Lake, Larry W., Richardson, TX, 2007

Brooks, R. H. and Corey, A. T.: *Properties of Porous Media Affecting Fluid Flow*, J. Irrigation Drainage Division, Proc. of ASCE, 92 (No. IR2), p. 61-88, 1966.

Burdine, N. T.: *Relative Permeability Calculations from Pore Size Distribution Data*, Trans. AIME v. 198, p. 71-78, 1953.

Canel, C. A., and Rosbaco, J.: *Compositional Material Balance: Its Application to the Development of an Oil and Gas Field with Retrograde Condensation*, SPE Paper 23647 presented at the Second Latin American Petroleum Engineering Conference held in Caracas, Venezuela, March 1992.

Carlson, Mike R.: *Practical Reservoir Simulation*, PennWell Publishing Co, ISBN 0-87814-803-5, 2003.

Chopra, A. K., and Carter, Robert D.: *Proof of the Two-Phase Steady-State Theory for Flow Through Porous Media*, SPE Paper 14472, SPE Journal, p. 603-608, December 1986.

Coats, K. H.: *An Equation of State Compositional Model*, SPE Paper 8284, SPE Journal, p. 533-554, December 1980.

Corey, A. T.: *The Interrelation between Gas and Oil Relative Permeabilities*, Prod. Monthly, 19, 38, November 1954.

Doublet, L. E., Pande, P. K., McCollum, T. J., and Blasingame, T. A.: *Decline Curve Analysis Using Type Curves-Analysis of Oil Well Production Data Using Material Balance Time: Application to Field Cases*, SPE Paper 28688 presented at the 1994 Petroleum Conference and Exhibition of Mexico held in Veracruz, Mexico, October 1994.

Ertekin, T., Abou-Kassem, J. H., King, G. R.: *Basic Applied Reservoir Simulation*, SPE Textbook Series volume 7, Henry L. Doherty Memorial Fund of AIME, Richardson, TX, ISBN 1-55563-089-8, 2001.

Ertekin, T., King, G., and Schwerer, F.: *Dynamic Gas Slippage: A Unique Dual Mechanism Approach to the Flow of Gas in Tight Formations*, SPE Paper 12045, SPE Formation Evaluation, p. 43-52, February 1986.

Fan, Li, Harris, Billy W., Jamaluddin, A., Mott, Robert, Pope, Gary A., Shandrygin, Alexander, Whitson, Curtis H.: *Understanding Gas-Condensate Reservoirs*, Schlumberger Oil Field Review, p. 14-27, Winter 2005/2006.

Fanchi, John R.: *Principle of Applied Reservoir Simulation*, Third edition, Gulf Professional Publishing Co, ISBN 0-7506-7933-6, 2006.

Fevang, Oivind, and Whitson, C. H.: *Modeling Gas-Condensate Well Deliverability*, SPE Paper 30714, SPE Journal, p. 221-230, November 1996.

Firoozabadi, A. and Hauge, J.: *Capillary Pressure in Fractured Porous Media*, SPE Paper 18747, Journal of Petroleum Technology, p. 784-791, June 1990.

Gang, Tao, and Kelkar, Mohan: *A More General Capillary Pressure Curve and its Estimation from Production Data*, SPE Paper 108180 presented at the SPE Rocky Mountain Oil & Gas Technology Symposium held in Denver, Colorado, April 2007.

Gomes, Hamilton P., and Correa, Antonio Claudio F.: *Fully Implicit Compositional Modeling of Gas Condensate and Volatile Oil Reservoirs*. SPE Paper 23700 presented at the Second Latin American Petroleum Engineering Conference held in Caracas, Venezuela, March 8-11 1992.

Hepguler, G. , and Bard, W.: *Integration of a Field Surface and Production Network With a Reservoir Simulator*, SPE Paper 38937, SPE Computer Application Journal, p. 80-92, June 1997.

Kazemi, H., Vestal, C. R., and Shank, G.D.: *An Efficient Multi-component Numerical Simulator*, SPE Paper 6890, SPE Journal, p. 355-368, October 1978.

Kenyon, D. and Behie, G.: *Third SPE Comparative Project: Gas Cycling of Retrograde Condensate Reservoirs*, SPE Paper 12278, Journal of Petroleum Technology, p. 981-997, Aug. 1987.

Lee, S-T: *Capillary-Gravity Equilibria for Hydrocarbon Fluids in Porous Media*, SPE Paper 19650 presented at the 64th Annual Technical Conference and Exhibition held in San Antonio, TX, October 1989.

Leverett, M. C.: *Capillary Behavior in Porous Solids*, Trans. AIME v. 142, p. 152-168, 1941.

Li, Kewen: *Generalized Capillary Pressure and Relative Permeability Model Inferred from Fractal Characterization of Porous Media*, SPE Paper 89874 presented at the SPE Annual Technical Conference and Exhibition held in Houston, Texas, September 2004.

Li, Kewen: *Theoretical Development of the Brooks-Corey Capillary Pressure Model from Fractal Modeling of Porous Media*, SPE Paper 89429 presented at the 2004 SPE/DOE Fourteenth Symposium on Improved Oil Recovery held in Tulsa, Oklahoma, April 2004.

Li, Kewen, and Horne, Roland N.: *Experimental Verification of Methods to Calculate Relative Permeability Using Capillary Pressure Data*, SPE Paper 76757 presented at the SPE Western Regional/AAPG Pacific Section Joint Meeting held in Anchorage, Alaska, May 2002.

Li, Kewen, and Horne, Roland N.: *Fractal Characterization of the Geysers Rock*, Trans. Geothermal Resources Council, v. 27, p. 707-710, 2003.

McCain, W. D. Jr.: *Chemical Composition Determines Behavior of Reservoir Fluids*, Petroleum Engineer International, September 1993.

Mott, Robert, Cable, Andrew, and Spearing, Mike: *Measurements and Simulation of Inertial and High Capillary Number Flow Phenomena in Gas-Condensate Relative Permeability*, SPE Paper 62932 presented at the 2000 SPE Annual Technical Conference and Exhibition held in Dallas, Texas, October 2000.

Nghiem, L. X., Fong, D. K. and Aziz, K.: *Compositional Modeling with and Equation of State*, SPE Paper 9306, SPE Journal, p. 687-698, December 1981.

Peaceman, D.W.: *Convection in Fractured Reservoirs—The Effect of Matrix-Fissure Transfer on the Instability of a Density Inversion in a Vertical Fracture*, SPE Journal, p. 269-280, October 1976.

Pooladi-Darvish, Mehran, and Firoozabadi, Abbas: *Cocurrent and Countercurrent Imbibitions in a Water-Wet Matrix Block*, SPE Paper 38443, SPE Journal v.5, Num. 1, p. 3-11, March 2000.

Poston, Steven W., and Poe, Bobby D., Jr.: *Analysis of Production Decline Curves*, SPE Petroleum Engineers, Editor: Filler, Stuart L., Richardson, TX, ISBN 978-1-55563-144-4, 2008.

Schilthuis, R. J.: *Active Oil and Reservoir Energy*, Trans. AIME, v. 118, p. 33-52, 1936.

Shapiro, A. A., and Stenby, E. H.: *Effects of Capillary Forces and Adsorption on Reserves Distribution*, SPE Paper 36922 presented at the 1996 SPE European Petroleum Conference held in Milan, Italy, October 1996.

Shi, Chunmei, and Horne, Roland N.: *Improved Recovery in Gas-Condensate Reservoirs Considering Compositional Variations*, SPE Paper 115786 presented at the 2008 SPE Annual Technical Conference and Exhibition held in Denver, Colorado, September 2008.

Skjaeveland, S. M., Kjosavik, A., Hammervold Thomas, W. L., and Virnovsky, G. A.: *Capillary Pressure Correlation for Mixed-Wet Reservoirs*, SPE Paper 60900, SPE Reservoir Evaluation & Engineering v.3, number 1, p. 60-67, February 2000.

Thomeer, J. H. M.: *Introduction of a Pore Geometrical Factor Defined by the Capillary Pressure Curve*, Paper number 1324-G, Society of Petroleum Engineers of AIME, Journal of Petroleum Technology, v. 12, number 3, p. 73-77, 1960.

Tusiani, D.M., and Shearer, G.: *LNG a Nontechnical Guide*, PennWell Publishing Co, p. 5-11 and 27, 2007

Van Genuchten, M. T.: *A Closed-form Equation for Predicting the Hydraulic Conductivity of Unsaturated Soils*, Soil Sci. Soc. Am. J. 44:892-898, 1980.

Van Golf-Racht, T.D.: *Fundamentals of Fractured Reservoir Engineering*, Developments in Petroleum Science volume 12, Elsevier, New York, NY, ISBN 0-444-42046-0, 1982.

Warren, J. E. and Root, P. J.: *The Behavior of Naturally Fractured Reservoirs*, SPE Journal, p. 245-255, Trans. AIME, v. 234, September 1963.

Wheaton, R. J., and Zhang, H. R.*: Condensate Banking Dynamics in Gas Condensate Fields: Compositional Changes and Condensate Accumulation Around Production Wells*, SPE Paper 62930 presented at the 2000 SPE Annual Technical Conference and Exhibition held in Dallas, Texas, 1–4 October 2000.

Whitson, C. H., Fevang, Oivind, and Saevareid, A.: *Gas Condensate Relative Permeability for Well Calculations*, Transport in Porous Media 52: p. 279–311, 2003.

Young, L. C. and Stephenson, R. E.: *A Generalized Compositional Approach for Reservoir Simulation*, SPE Journal, p. 727-742, October 1983.

Appendix A

DERIVATION OF WATER FLOW EQUATION

The differential equation demonstrated in equation (4.12) is derived from the substitution of Darcy's law into the continuity equation. Since the water is not reacting with the hydrocarbon and the diffusion phenomenon is insignificant in the liquid phase water is treated as a mobile phase at which the flow is only driven by Darcy's law. The continuity equation is obtained through the same development used in Chapter 4 to represent the continuity equation for the hydrocarbon phases. It also required assigning a representative control volume (CV) at which the fluids is flowing through, and writing the molar-balance over the specified elemental volume accordingly.

Considering the control volume illustration in Figure **4.1**, the molar-balance of the continuity equation entering or leaving the system can be expresses over time (Δt) in the form of:

(Moles entering CV – Moles leaving CV) + Molar external source = Accumulation

… (A.1)

In order to obtain a mathematical representation of equation (A.1), the following representations are considered:

Moles of water IN = $(N_{w_x} + N_{w_y} + N_{w_z})\Delta t$ (A.2a)

Moles of water OUT = $(N_{w_{x+\Delta x}} + N_{w_{y+\Delta y}} + N_{w_{z+\Delta z}})\Delta t$ (A.2b)

Accumulation = $(\Delta x \Delta y \Delta z \phi(\mathrm{S_w} \frac{\rho_\mathrm{w}}{\mathrm{MW_w}}))_{t+\Delta t} - (\Delta x \Delta y \Delta z \phi(\mathrm{S_w} \frac{\rho_\mathrm{w}}{\mathrm{MW_w}}))_t$ (A.2c)

Considering that the molar flow rate (N_w) in the previous illustration is the flow rate of water within the system, equation A.1 can be expressed as shown in equation (A.3), which is the result of dividing by (Δt) and assigning positive (+) sign to flow going into the system and negative (-) for flow leaving the system.

$$-[(N_w)_{x+\Delta x} - (N_w)_x] - \left[(N_w)_{y+\Delta y} - (N_w)_y\right] - [(N_w)_{z+\Delta z} - (N_w)_z]$$

$$+Q_w = \frac{\Delta x \Delta y \Delta z}{\Delta t}\left(\left[\phi(\mathrm{S_w}\frac{\rho_\mathrm{w}}{\mathrm{MW_w}})\right]_{t+\Delta t} - \left[\phi(\mathrm{S_w}\frac{\rho_\mathrm{w}}{\mathrm{MW_w}})\right]_t\right) \quad \text{(A.3)}$$

The expression of (A.3) can be expanded by expressing the molar flow rate through each face of the control volume (x, y, and z) as a function of the phase movement velocity, the fraction of the molar density of the phase, and the area perpendicular to the flow direction. The expression can be re-constructed to give the following form:

$$-\frac{\rho_{wsc}}{MW_w}\left[\left(\frac{v_{wx}A_x}{B_w}\right)_{x+\Delta x} - \left(\frac{v_{wx}A_x}{B_w}\right)_x\right] - \frac{\rho_{wsc}}{MW_w}\left[\left(\frac{v_{wy}A_y}{B_w}\right)_{y+\Delta y} - \left(\frac{v_{wy}A_y}{B_w}\right)_y\right]$$

$$-\frac{\rho_{wsc}}{MW_w}\left[\left(\frac{v_{wz}A_z}{B_w}\right)_{z+\Delta z} - \left(\frac{v_{wz}A_z}{B_w}\right)_z\right] + Q_w = \frac{V_b}{\Delta t}\frac{\rho_{wsc}}{MW_w}\left(\left[\phi\left(\frac{\mathrm{S_w}}{\mathrm{B_w}}\right)\right]_{t+\Delta t} - \left[\phi\left(\frac{\mathrm{S_w}}{\mathrm{B_w}}\right)\right]_t\right)$$

… (A.4)

By dividing equation (A.4) by the bulk volume ($V_b = \Delta x \Delta y \Delta z$) and $\frac{\rho_{wsc}}{MW_w}$, the following expression is obtained:

$$-\frac{\left[\left(\frac{v_{wx}}{B_w}\right)_{x+\Delta x} - \left(\frac{v_{wx}}{B_w}\right)_x\right]}{\Delta x} - \frac{\left[\left(\frac{v_{wy}}{B_w}\right)_{y+\Delta y} - \left(\frac{v_{wy}}{B_w}\right)_y\right]}{\Delta y} - \frac{\left[\left(\frac{v_{wz}}{B_w}\right)_{z+\Delta z} - \left(\frac{v_{wz}}{B_w}\right)_z\right]}{\Delta z}$$

$$+\frac{Q_w MW_w}{V_b \rho_{wsc}} = \frac{1}{\Delta t}\left(\left[\phi\left(\frac{\mathrm{S_w}}{\mathrm{B_w}}\right)\right]_{t+\Delta t} - \left[\phi\left(\frac{\mathrm{S_w}}{\mathrm{B_w}}\right)\right]_t\right) \quad \text{(A.5)}$$

In order to write equation (A.5) in the differential form, the limits of Δx, Δy, Δz, and Δt need to be taken in for form of $\lim_{\Delta s \to 0}\{Left\ hand\ side\} = \lim_{\Delta s \to 0}\{Left\ hand\ side\}$. While recalling that $\lim_{\Delta s \to 0}\frac{f(s+\Delta s)-f(s)}{\Delta s} = \frac{\partial f}{\partial s}$, the previous expression can be re-written in the differential form as shown below:

$$-\frac{\partial}{\partial x}\left(\frac{v_{wx}}{B_w}\right) - \frac{\partial}{\partial y}\left(\frac{v_{wy}}{B_w}\right) - \frac{\partial}{\partial z}\left(\frac{v_{wz}}{B_w}\right) + \frac{Q_w MW_w}{V_b \rho_{wsc}} = \frac{\partial}{\partial t}\left[\phi\left(\frac{\mathrm{S_w}}{\mathrm{B_w}}\right)\right] \quad \text{(A.6)}$$

In order to express continuity equation for variable flow area, equation (A.6) need to be multiplied by the bulk volume which would give the following representation of the continuity equation used in this model:

$$-\frac{\partial}{\partial x}\left(\frac{v_{wx}\,A_x}{B_w}\right)-\frac{\partial}{\partial y}\left(\frac{v_{wy}\,A_y}{B_w}\right)-\frac{\partial}{\partial z}\left(\frac{v_{wz}\,A_z}{B_w}\right)+\frac{Q_w\,MW_w}{\rho_{wsc}}=V_b\,\frac{\partial}{\partial t}\left[\phi\left(\frac{\mathrm{S_w}}{\mathrm{B_w}}\right)\right] \qquad \text{(A.7)}$$

To come up with the governing differential equation of hydrocarbon presented in equation (4.12), a suitable velocity model needs to be substituted in the molar velocity terms of equation (4.7) to represent the flow of fluids within the system. The model used for this work, which was developed by Ayala (2006), was built to accommodate a multi-mechanists flow. That means that the model is capable of considering different flow potentials which are responsible of the flow in the system. The concept of the multi-mechanistic flow was introduced by Ertekin *et al.* (1986), which emphasizes that the fluid flow within the system is driven by the concentration or density gradients denoted as diffusion and the bulk velocity which is influenced by the pressure gradient. Thus, the total molar velocity is a result of the flow driven by the bulk Darcian effect (v_{fs}^{D}) added to the flow caused by the Flickian component (v_{mfs}^{F}) as illustrated in equations (A.8).

$$v_{ws}=v_{ws}^{D}+v_{ws}^{F} \quad ; \quad s = x, y, \text{ and } z \qquad \text{(A.8)}$$

However, since the water is not reacting with the hydrocarbon and the diffusion phenomenon is insignificant in the liquid phase, water is treated as a mobile phase at which the flow is only driven by Darcy's law as represented by equation (A.9a).

$$v_{ws}=v_{ws}^{D} \quad ; \quad s = x, y, \text{ and } z \qquad \text{(A.9a)}$$

$$\text{where: } v_{ws}^{D}=-5.615\,\frac{k_s k_{rw}}{\mu_w}\,\frac{\partial \Phi_w}{\partial s} \quad ; \quad s = x, y, \text{ and } z \qquad \text{(A.9b)}$$

By substituting the velocity terms in the continuity equation (A.7) and dividing the whole term by 5.615 to adjust the units to (STB/D), we get the following differential material balance equation:

$$\frac{\partial}{\partial x}\left(\frac{A_x k_x k_{rw}}{\mu_w}\frac{\partial \Phi_w}{\partial x}\right)\Delta x + \frac{\partial}{\partial y}\left(\frac{A_y k_y k_{rw}}{\mu_w}\frac{\partial \Phi_w}{\partial y}\right)\Delta y + \frac{\partial}{\partial z}\left(\frac{A_z k_z k_{rw}}{\mu_w}\frac{\partial \Phi_w}{\partial z}\right)\Delta z$$

$$+q_{sc,w} = \frac{V_b}{5.615}\frac{\partial}{\partial t}\left[\phi\left(\frac{S_w}{B_w}\right)\right] \quad ; \quad m = 1, 2, \ldots, n_c \qquad \text{(A.10a)}$$

where: $q_{sc,w} = \frac{Q_w MW_w}{5.615\rho_{wsc}}$ (A.10b)

and, $\frac{\partial \Phi_w}{\partial s} = \frac{\partial p_w}{\partial s} - \frac{1}{144}\frac{g}{g_c}\rho_w \frac{\partial G}{\partial s}$; *f = o, or g* , *s = x, y, and z* (A.10c)

Re-arranging equation (4.10a), leads to the final representation of the governing differential equations used in the model, which was presented in the work of Ayala (2006).

$$\frac{\partial}{\partial x}\left(\frac{A_x k_x k_{rw}}{\beta_w \mu_w}\frac{\partial p_w}{\partial x} - \frac{1}{144}\frac{g}{g_c}\rho_o \frac{A_x k_x k_{rw}}{\beta_w \mu_w}\frac{\partial G}{\partial x}\right)\Delta x + \frac{\partial}{\partial y}\left(\frac{A_y k_y k_{rw}}{\beta_w \mu_w}\frac{\partial p_w}{\partial y} - \frac{1}{144}\frac{g}{g_c}\rho_o \frac{A_y k_y k_{rw}}{\beta_w \mu_w}\frac{\partial G}{\partial y}\right)\Delta y$$

$$+\frac{\partial}{\partial z}\left(\frac{A_z k_z k_{rw}}{\beta_w \mu_w}\frac{\partial p_w}{\partial z} - \frac{1}{144}\frac{g}{g_c}\rho_o \frac{A_z k_z k_{rw}}{\beta_w \mu_w}\frac{\partial G}{\partial z}\right)\Delta z + q_{sc,w}$$

$$= \frac{V_b}{5.615}\frac{\partial}{\partial t}\left[\frac{\phi\, S_w}{\beta_w}\right] \qquad \text{(A.11)}$$

Appendix B

FINITE DIFFERENCE REPRESENTATION

Compositional simulators comprise of a system of non-linear partial differential equation, where the partial derivatives are replaced with finite differences approximation derived from Taylor's series. The finite differential representation of the compositional and water balance differential equation (4.11 and 4.12) is represented in the following form after the substitution of the unknowns with the primary unknowns:

$$\frac{A_x k_x}{\Delta x}\Big|_{i+\frac{1}{2},j,k} \frac{\bar{\rho}_o}{\mu_o}\Big|_{i+\frac{1}{2},j,k}^{n+1} x_m k_{ro}|_{i+\frac{1}{2},j,k}^{n+1} \left({p_g}_{i+1,j,k}^{n+1} - {p_g}_{i,j,k}^{n+1}\right)$$

$$-\frac{A_x k_x}{\Delta x}\Big|_{i-\frac{1}{2},j,k} \frac{\bar{\rho}_o}{\mu_o}\Big|_{i-\frac{1}{2},j,k}^{n+1} x_m k_{ro}|_{i-\frac{1}{2},j,k}^{n+1} \left({p_g}_{i,j,k}^{n+1} - {p_g}_{i-1,j,k}^{n+1}\right)$$

$$+\frac{A_x k_x}{\Delta x}\Big|_{i+\frac{1}{2},j,k} \frac{\bar{\rho}_g}{\mu_g}\Big|_{i+\frac{1}{2},j,k}^{n+1} y_m k_{rg}|_{i+\frac{1}{2},j,k}^{n+1} \left({p_g}_{i+1,j,k}^{n+1} - {p_g}_{i,j,k}^{n+1}\right)$$

$$-\frac{A_x k_x}{\Delta x}\Big|_{i-\frac{1}{2},j,k} \frac{\bar{\rho}_g}{\mu_g}\Big|_{i-\frac{1}{2},j,k}^{n+1} y_m k_{rg}|_{i-\frac{1}{2},j,k}^{n+1} \left({p_g}_{i,j,k}^{n+1} - {p_g}_{i-1,j,k}^{n+1}\right)$$

$$-\frac{A_x k_x}{\Delta x}\Big|_{i+\frac{1}{2},j,k} \frac{\bar{\rho}_o}{\mu_o}\Big|_{i+\frac{1}{2},j,k}^{n+1} x_m k_{ro}|_{i+\frac{1}{2},j,k}^{n+1} \left({p_{cgo}}_{i+1,j,k}^{n+1} - {p_{cgo}}_{i,j,k}^{n+1}\right)$$

$$+\frac{A_x k_x}{\Delta x}\Big|_{i-\frac{1}{2},j,k} \frac{\bar{\rho}_o}{\mu_o}\Big|_{i-\frac{1}{2},j,k}^{n+1} x_m k_{ro}|_{i-\frac{1}{2},j,k}^{n+1} \left({p_{cgo}}_{i,j,k}^{n+1} - {p_{cgo}}_{i-1,j,k}^{n+1}\right)$$

$$+\frac{D_{eff} A_x}{5.615\Delta x}\Big|_{i+\frac{1}{2},j,k} \phi S_g|_{i+\frac{1}{2},j,k} y_m|_{i+\frac{1}{2},j,k}^{n+1} \left({\bar{\rho}_g}_{i+1,j,k}^{n+1} - {\bar{\rho}_g}_{i,j,k}^{n+1}\right)$$

$$-\frac{D_{eff} A_x}{5.615\Delta x}\Big|_{i-\frac{1}{2},j,k} \phi S_g|_{i-\frac{1}{2},j,k} y_m|_{i-\frac{1}{2},j,k}^{n+1} \left({\bar{\rho}_g}_{i,j,k}^{n+1} - {\bar{\rho}_g}_{i-1,j,k}^{n+1}\right)$$

$$-\left\{\frac{1}{144}\frac{g}{g_c}\frac{A_x k_x}{\Delta x}\Big|_{i+\frac{1}{2},j,k} \frac{\rho_o \bar{\rho}_o}{\mu_o}\Big|_{i+\frac{1}{2},j,k}^{n+1} x_m k_{ro}|_{i+\frac{1}{2},j,k}^{n+1} \left(G_{i+1,j,k}^{n+1} - G_{i,j,k}^{n+1}\right)\right.$$

$$-\frac{1}{144}\frac{g}{g_c}\frac{A_x k_x}{\Delta x}\Big|_{i-\frac{1}{2},j,k}\frac{\rho_o\bar{\rho}_o}{\mu_o}\Big|_{i-\frac{1}{2},j,k}^{n+1}x_m k_{ro}|_{i-\frac{1}{2},j,k}^{n+1}\left(G_{i,j,k}^{n+1}-G_{i-1,j,k}^{n+1}\right)$$

$$+\frac{1}{144}\frac{g}{g_c}\frac{A_x k_x}{\Delta x}\Big|_{i+\frac{1}{2},j,k}\frac{\rho_g\bar{\rho}_g}{\mu_o}\Big|_{i+\frac{1}{2},j,k}^{n+1}y_m k_{rg}|_{i+\frac{1}{2},j,k}^{n+1}\left(G_{i+1,j,k}^{n+1}-G_{i,j,k}^{n+1}\right)$$

$$-\frac{1}{144}\frac{g}{g_c}\frac{A_x k_x}{\Delta x}\Big|_{i-\frac{1}{2},j,k}\frac{\rho_g\bar{\rho}_g}{\mu_g}\Big|_{i-\frac{1}{2},j,k}^{n+1}y_m k_{rg}|_{i-\frac{1}{2},j,k}^{n+1}\left(G_{i,j,k}^{n+1}-G_{i-1,j,k}^{n+1}\right)\Bigg\}$$

$$+\frac{A_y k_y}{\Delta y}\Big|_{i,j+\frac{1}{2},k}\frac{\bar{\rho}_o}{\mu_o}\Big|_{i,j+\frac{1}{2},k}^{n+1}x_m k_{ro}|_{i,j+\frac{1}{2},k}^{n+1}\left({p_g}_{i,j+1,k}^{n+1}-{p_g}_{i,j,k}^{n+1}\right)$$

$$-\frac{A_y k_y}{\Delta y}\Big|_{i,j-\frac{1}{2},k}\frac{\bar{\rho}_o}{\mu_o}\Big|_{i,j-\frac{1}{2},k}^{n+1}x_m k_{ro}|_{i,j-\frac{1}{2},k}^{n+1}\left({p_g}_{i,j,k}^{n+1}-{p_g}_{i,j-1,k}^{n+1}\right)$$

$$+\frac{A_y k_y}{\Delta y}\Big|_{i,j+\frac{1}{2},k}\frac{\bar{\rho}_g}{\mu_g}\Big|_{i,j+\frac{1}{2},k}^{n+1}y_m k_{rg}|_{i,j+\frac{1}{2},k}^{n+1}\left({p_g}_{i,j+1,k}^{n+1}-{p_g}_{i,j,k}^{n+1}\right)$$

$$-\frac{A_y k_y}{\Delta y}\Big|_{i,j-\frac{1}{2},k}\frac{\bar{\rho}_g}{\mu_g}\Big|_{i,j-\frac{1}{2},k}^{n+1}y_m k_{rg}|_{i,j-\frac{1}{2},k}^{n+1}\left({p_g}_{i,j,k}^{n+1}-{p_g}_{i,j-1,k}^{n+1}\right)$$

$$-\frac{A_y k_y}{\Delta y}\Big|_{i,j+\frac{1}{2},k}\frac{\bar{\rho}_o}{\mu_o}\Big|_{i,j+\frac{1}{2},k}^{n+1}x_m k_{ro}|_{i,j+\frac{1}{2},k}^{n+1}\left({p_{cgo}}_{i,j+1,k}^{n+1}-{p_{cgo}}_{i,j,k}^{n+1}\right)$$

$$+\frac{A_y k_y}{\Delta y}\Big|_{i.j-\frac{1}{2},k}\frac{\bar{\rho}_o}{\mu_o}\Big|_{i,j-\frac{1}{2},k}^{n+1}x_m k_{ro}|_{i,j-\frac{1}{2},k}^{n+1}\left({p_{cgo}}_{i,j,k}^{n+1}-{p_{cgo}}_{i,j-1,k}^{n+1}\right)$$

$$+\frac{D_{eff}A_y}{5.615\Delta y}\Big|_{i,j+\frac{1}{2},k}\phi S_g\big|_{i,j+\frac{1}{2},k}y_m|_{i,j+\frac{1}{2},k}^{n+1}\left({\bar{\rho}_g}_{i,j+1,k}^{n+1}-{\bar{\rho}_g}_{i,j,k}^{n+1}\right)$$

$$-\frac{D_{eff}A_y}{5.615\Delta y}\Big|_{i,j-\frac{1}{2},k}\phi S_g\big|_{i,j-\frac{1}{2},k}y_m|_{i,j-\frac{1}{2},k}^{n+1}\left({\bar{\rho}_g}_{i,j,k}^{n+1}-{\bar{\rho}_g}_{i,j-1,k}^{n+1}\right)$$

$$-\Bigg\{\frac{1}{144}\frac{g}{g_c}\frac{A_y k_y}{\Delta y}\Big|_{i,j+\frac{1}{2},k}\frac{\rho_o\bar{\rho}_o}{\mu_o}\Big|_{i,j+\frac{1}{2},k}^{n+1}x_m k_{ro}|_{i,j+\frac{1}{2},k}^{n+1}\left(G_{i,j+1,k}^{n+1}-G_{i,j,k}^{n+1}\right)$$

$$-\frac{1}{144}\frac{g}{g_c}\frac{A_y k_y}{\Delta y}\Big|_{i,j-\frac{1}{2},k}\frac{\rho_o\bar{\rho}_o}{\mu_o}\Big|_{i,j-\frac{1}{2},k}^{n+1}x_m k_{ro}|_{i,j-\frac{1}{2},k}^{n+1}\left(G_{i,j,k}^{n+1}-G_{i,j-1,k}^{n+1}\right)$$

$$+\frac{1}{144}\frac{g}{g_c}\frac{A_y k_y}{\Delta y}\Big|_{i,j+\frac{1}{2},k}\frac{\rho_g\bar{\rho}_g}{\mu_o}\Big|_{i,j+\frac{1}{2},k}^{n+1} y_m k_{rg}\big|_{i,j+\frac{1}{2},k}^{n+1}\left(G_{i,j+1,k}^{n+1}-G_{i,j,k}^{n+1}\right)$$

$$\left.-\frac{1}{144}\frac{g}{g_c}\frac{A_y k_y}{\Delta y}\Big|_{i,j-\frac{1}{2},k}\frac{\rho_g\bar{\rho}_g}{\mu_g}\Big|_{i,j-\frac{1}{2},k}^{n+1} y_m k_{rg}\big|_{i,j-\frac{1}{2},k}^{n+1}\left(G_{i,j,k}^{n+1}-G_{i,j-1,k}^{n+1}\right)\right\}$$

$$+\frac{A_z k_z}{\Delta z}\Big|_{i,j,k+\frac{1}{2}}\frac{\bar{\rho}_o}{\mu_o}\Big|_{i,j,k+\frac{1}{2}}^{n+1} x_m k_{ro}\big|_{i,j,k+\frac{1}{2}}^{n+1}\left({p_g}_{i,j,k+1}^{n+1}-{p_g}_{i,j,k}^{n+1}\right)$$

$$-\frac{A_z k_z}{\Delta z}\Big|_{i,j,k-\frac{1}{2}}\frac{\bar{\rho}_o}{\mu_o}\Big|_{i,j,k-\frac{1}{2}}^{n+1} x_m k_{ro}\big|_{i,j,k-\frac{1}{2}}^{n+1}\left({p_g}_{i,j,k}^{n+1}-{p_g}_{i,j,k-1}^{n+1}\right)$$

$$+\frac{A_z k_z}{\Delta z}\Big|_{i,j,k+\frac{1}{2}}\frac{\bar{\rho}_g}{\mu_g}\Big|_{i,j,k+\frac{1}{2}}^{n+1} y_m k_{rg}\big|_{i,j,k+\frac{1}{2}}^{n+1}\left({p_g}_{i,j,k+1}^{n+1}-{p_g}_{i,j,k}^{n+1}\right)$$

$$-\frac{A_z k_z}{\Delta z}\Big|_{i,j,k-\frac{1}{2}}\frac{\bar{\rho}_g}{\mu_g}\Big|_{i,j,k-\frac{1}{2}}^{n+1} y_m k_{rg}\big|_{i,j,k-\frac{1}{2}}^{n+1}\left({p_g}_{i,j,k}^{n+1}-{p_g}_{i,j,k-1}^{n+1}\right)$$

$$-\frac{A_z k_z}{\Delta z}\Big|_{i,j,k+\frac{1}{2}}\frac{\bar{\rho}_o}{\mu_o}\Big|_{i,j,k+\frac{1}{2}}^{n+1} x_m k_{ro}\big|_{i,j,k+\frac{1}{2}}^{n+1}\left({p_{cgo}}_{i,j,k+1}^{n+1}-{p_{cgo}}_{i,j,k}^{n+1}\right)$$

$$+\frac{A_z k_z}{\Delta z}\Big|_{i,j,k-\frac{1}{2}}\frac{\bar{\rho}_o}{\mu_o}\Big|_{i,j,k-\frac{1}{2}}^{n+1} x_m k_{ro}\big|_{i,j,k-\frac{1}{2}}^{n+1}\left({p_{cgo}}_{i,j,k}^{n+1}-{p_{cgo}}_{i,j,k-1}^{n+1}\right)$$

$$+\frac{D_{eff}A_z}{5.615\Delta z}\Big|_{i,j,k+\frac{1}{2}}\phi S_g\big|_{i,j,k+\frac{1}{2}} y_m\big|_{i,j,k+\frac{1}{2}}^{n+1}\left(\bar{\rho}_g{}_{i,j,k+1}^{n+1}-\bar{\rho}_g{}_{i,j,k}^{n+1}\right)$$

$$-\frac{D_{eff}A_z}{5.615\Delta z}\Big|_{i,j,k-\frac{1}{2}}\phi S_g\big|_{i,j,k-\frac{1}{2}} y_m\big|_{i,j,k-\frac{1}{2}}^{n+1}\left(\bar{\rho}_g{}_{i,j,k}^{n+1}-\bar{\rho}_g{}_{i,j,k-1}^{n+1}\right)$$

$$-\left\{\frac{1}{144}\frac{g}{g_c}\frac{A_z k_z}{\Delta z}\Big|_{i,j,k+\frac{1}{2}}\frac{\rho_o\bar{\rho}_o}{\mu_o}\Big|_{i,j,k+\frac{1}{2}}^{n+1} x_m k_{ro}\big|_{i,j,k+\frac{1}{2}}^{n+1}\left(G_{i,j,k+1}^{n+1}-G_{i,j,k}^{n+1}\right)\right.$$

$$-\frac{1}{144}\frac{g}{g_c}\frac{A_z k_z}{\Delta z}\Big|_{i,j,k-\frac{1}{2}}\frac{\rho_o\bar{\rho}_o}{\mu_o}\Big|_{i,j,k-\frac{1}{2}}^{n+1} x_m k_{ro}\big|_{i,j,k-\frac{1}{2}}^{n+1}\left(G_{i,j,k}^{n+1}-G_{i,j,k-1}^{n+1}\right)$$

$$+\frac{1}{144}\frac{g}{g_c}\frac{A_z k_z}{\Delta z}\Big|_{i,j,k+\frac{1}{2}}\frac{\rho_g\bar{\rho}_g}{\mu_o}\Big|_{i,j,k+\frac{1}{2}}^{n+1} y_m k_{rg}\big|_{i,j,k+\frac{1}{2}}^{n+1}\left(G_{i,j,k+1}^{n+1}-G_{i,j,k}^{n+1}\right)$$

$$-\frac{1}{144}\frac{g}{g_c}\frac{A_z k_z}{\Delta z}\Big|_{i,j,k-\frac{1}{2}}\frac{\rho_g \bar{\rho}_g}{\mu_g}\Big|_{i,j,k-\frac{1}{2}}^{n+1} y_m k_{rg}|_{i,j,k-\frac{1}{2}}^{n+1}\left(G_{i,j,k}^{n+1}-G_{i,j,k-1}^{n+1}\right)\Bigg\}$$

$$+M_m^l$$

$$=\frac{V_b}{5.615\Delta t}\left[\left(\phi\, S_o x_m \bar{\rho}_o+\phi(1-S_o-S_w)y_m\bar{\rho}_g\right)_{i,j,k}^{n+1}-\left(\phi\, S_o x_m \bar{\rho}_o+\phi(1-S_o-S_w)y_m\bar{\rho}_g\right)_{i,j,k}^{n}\right]$$

$$; \qquad m=1,2,\dots,n_c \qquad \dots \text{ (B.1a)}$$

and, the water equation is represented as the following:

$$\frac{A_x k_x}{\Delta x}\Big|_{i+\frac{1}{2},j,k}\frac{1}{\mu_w\beta_w}\Big|_{i+\frac{1}{2},j,k}^{n+1} k_{rw}|_{i+\frac{1}{2},j,k}^{n+1}\left({p_g}_{i+1,j,k}^{n+1}-{p_g}_{i,j,k}^{n+1}\right)$$

$$-\frac{A_x k_x}{\Delta x}\Big|_{i-\frac{1}{2},j,k}\frac{1}{\mu_w\beta_w}\Big|_{i-\frac{1}{2},j,k}^{n+1} k_{rw}|_{i-\frac{1}{2},j,k}^{n+1}\left({p_g}_{i,j,k}^{n+1}-{p_g}_{i-1,j,k}^{n+1}\right)$$

$$-\frac{A_x k_x}{\Delta x}\Big|_{i+\frac{1}{2},j,k}\frac{1}{\mu_w\beta_w}\Big|_{i+\frac{1}{2},j,k}^{n+1} k_{rw}|_{i+\frac{1}{2},j,k}^{n+1}\left({p_{cgo}}_{i+1,j,k}^{n+1}+{p_{cow}}_{i+1,j,k}^{n+1}-{p_{cgo}}_{i,j,k}^{n+1}-{p_{cow}}_{i,j,k}^{n+1}\right)$$

$$+\frac{A_x k_x}{\Delta x}\Big|_{i-\frac{1}{2},j,k}\frac{1}{\mu_w\beta_w}\Big|_{i-\frac{1}{2},j,k}^{n+1} k_{rw}|_{i-\frac{1}{2},j,k}^{n+1}\left({p_{cgo}}_{i,j,k}^{n+1}+{p_{cow}}_{i,j,k}^{n+1}-{p_{cgo}}_{i-1,j,k}^{n+1}-{p_{cow}}_{i-1,j,k}^{n+1}\right)$$

$$-\Bigg\{\frac{1}{144}\frac{g}{g_c}\frac{A_x k_x}{\Delta x}\Big|_{i+\frac{1}{2},j,k}\frac{\rho_w}{\mu_w\beta_w}\Big|_{i+\frac{1}{2},j,k}^{n+1} k_{rw}|_{i+\frac{1}{2},j,k}^{n+1}\left(G_{i+1,j,k}^{n+1}-G_{i,j,k}^{n+1}\right)$$

$$-\frac{1}{144}\frac{g}{g_c}\frac{A_x k_x}{\Delta x}\Big|_{i-\frac{1}{2},j,k}\frac{\rho_w}{\mu_w\beta_w}\Big|_{i-\frac{1}{2},j,k}^{n+1} k_{rw}|_{i-\frac{1}{2},j,k}^{n+1}\left(G_{i,j,k}^{n+1}-G_{i-1,j,k}^{n+1}\right)\Bigg\}$$

$$+\frac{A_y k_y}{\Delta y}\Big|_{i,j+\frac{1}{2},k}\frac{1}{\mu_w\beta_w}\Big|_{i,j+\frac{1}{2},k}^{n+1} k_{rw}|_{i,j+\frac{1}{2},k}^{n+1}\left({p_g}_{i,j+1,k}^{n+1}-{p_g}_{i,j,k}^{n+1}\right)$$

$$-\frac{A_y k_y}{\Delta y}\Big|_{i,j-\frac{1}{2},k}\frac{1}{\mu_w\beta_w}\Big|_{i,j-\frac{1}{2},k}^{n+1} k_{rw}|_{i,j-\frac{1}{2},k}^{n+1}\left({p_g}_{i,j,k}^{n+1}-{p_g}_{i,j-1,k}^{n+1}\right)$$

$$-\frac{A_y k_y}{\Delta y}\Big|_{i,j+\frac{1}{2},k}\frac{1}{\mu_w\beta_w}\Big|_{i,j+\frac{1}{2},k}^{n+1} k_{rw}|_{i,j+\frac{1}{2},k}^{n+1}\left(p_{cgo}{}_{i,j+1,k}^{n+1}+p_{cow}{}_{i,j+1,k}^{n+1}-p_{cgo}{}_{i,j,k}^{n+1}-p_{cow}{}_{i,j,k}^{n+1}\right)$$

$$+\frac{A_y k_y}{\Delta y}\Big|_{i,j-\frac{1}{2},k}\frac{1}{\mu_w\beta_w}\Big|_{i,j-\frac{1}{2},k}^{n+1} k_{rw}|_{i,j-\frac{1}{2},k}^{n+1}\left(p_{cgo}{}_{i,j,k}^{n+1}+p_{cow}{}_{i,j,k}^{n+1}-p_{cgo}{}_{i,j-1,k}^{n+1}-p_{cow}{}_{i,j-1,k}^{n+1}\right)$$

$$-\left\{\frac{1}{144}\frac{g}{g_c}\frac{A_y k_y}{\Delta y}\Big|_{i,j+\frac{1}{2},k}\frac{\rho_w}{\mu_w\beta_w}\Big|_{i,j+\frac{1}{2},k}^{n+1} k_{rw}|_{i,j+\frac{1}{2},k}^{n+1}\left(G_{i,j+1,k}^{n+1}-G_{i,j,k}^{n+1}\right)\right.$$

$$\left.-\frac{1}{144}\frac{g}{g_c}\frac{A_y k_y}{\Delta y}\Big|_{i,j-\frac{1}{2},k}\frac{\rho_w}{\mu_w\beta_w}\Big|_{i,j-\frac{1}{2},k}^{n+1} k_{rw}|_{i,j-\frac{1}{2},k}^{n+1}\left(G_{i,j,k}^{n+1}-G_{i,j-1,k}^{n+1}\right)\right\}$$

$$+\frac{A_z k_z}{\Delta z}\Big|_{i,j,k+\frac{1}{2}}\frac{1}{\mu_w\beta_w}\Big|_{i,j,k+\frac{1}{2}}^{n+1} k_{rw}|_{i,j,k+\frac{1}{2}}^{n+1}\left(p_g{}_{i,j,k+1}^{n+1}-p_g{}_{i,j,k}^{n+1}\right)$$

$$-\frac{A_z k_z}{\Delta z}\Big|_{i,j,k-\frac{1}{2}}\frac{1}{\mu_w\beta_w}\Big|_{i,j,k-\frac{1}{2}}^{n+1} k_{rw}|_{i,j,k-\frac{1}{2}}^{n+1}\left(p_g{}_{i,j,k}^{n+1}-p_g{}_{i,j,k-1}^{n+1}\right)$$

$$-\frac{A_z k_z}{\Delta z}\Big|_{i,j,k+\frac{1}{2}}\frac{1}{\mu_w\beta_w}\Big|_{i,j,k+\frac{1}{2}}^{n+1} k_{rw}|_{i,j,k+\frac{1}{2}}^{n+1}\left(p_{cgo}{}_{i,j,k+1}^{n+1}+p_{cow}{}_{i,j.k+1}^{n+1}-p_{cgo}{}_{i,j,k}^{n+1}-p_{cow}{}_{i,j,k}^{n+1}\right)$$

$$+\frac{A_z k_z}{\Delta z}\Big|_{i,j,k-\frac{1}{2}}\frac{1}{\mu_w\beta_w}\Big|_{i,j,k-\frac{1}{2}}^{n+1} k_{rw}|_{i,j,k-\frac{1}{2}}^{n+1}\left(p_{cgo}{}_{i,j,k}^{n+1}+p_{cow}{}_{i,j,k}^{n+1}-p_{cgo}{}_{i,j,k-1}^{n+1}-p_{cow}{}_{i,j,k-1}^{n+1}\right)$$

$$-\left\{\frac{1}{144}\frac{g}{g_c}\frac{A_z k_z}{\Delta z}\Big|_{i,j,k+\frac{1}{2}}\frac{\rho_w}{\mu_w\beta_w}\Big|_{i,j,k+\frac{1}{2}}^{n+1} k_{rw}|_{i,j,k+\frac{1}{2}}^{n+1}\left(G_{i,j,k+1}^{n+1}-G_{i,j,k}^{n+1}\right)\right.$$

$$\left.-\frac{1}{144}\frac{g}{g_c}\frac{A_z k_z}{\Delta z}\Big|_{i,j,k-\frac{1}{2}}\frac{\rho_w}{\mu_w\beta_w}\Big|_{i,j,k-\frac{1}{2}}^{n+1} k_{rw}|_{i,j,k-\frac{1}{2}}^{n+1}\left(G_{i,j,k}^{n+1}-G_{i,j,k-1}^{n+1}\right)\right\}$$

$$+q_{sc,w}^{l}=\frac{V_b}{5.615\Delta t}\left[\left(\frac{\phi S_w}{\beta_w}\right)_{i,j,k}^{n+1}-\left(\frac{\phi S_w}{\beta_w}\right)_{i,j,k}^{n}\right] \qquad \ldots \text{(B.1b)}$$

Equations (B.1a) and (B.1b) can be reduced to a shorter form by defining the transmissibility terms and substituting in the previous finite differential equations. The following will include the transmissibility terms for oil, gas, and water needed for the substitution:

$$T_{ox}\big|_{i\pm\frac{1}{2}}^{n+1} = \frac{A_x k_x}{\Delta x}\bigg|_{i\pm\frac{1}{2},j,k} \frac{\bar{\rho}_o}{\mu_o}\bigg|_{i\pm\frac{1}{2},j,k}^{n+1} x_m k_{ro}\big|_{i\pm\frac{1}{2},j,k}^{n+1} \tag{B.2a}$$

$$T_{gx}\big|_{i\pm\frac{1}{2}}^{n+1} = \frac{A_x k_x}{\Delta x}\bigg|_{i\pm\frac{1}{2},j,k} \frac{\bar{\rho}_g}{\mu_g}\bigg|_{i\pm\frac{1}{2},j,k}^{n+1} y_m k_{rg}\big|_{i\pm\frac{1}{2},j,k}^{n+1} \tag{B.2b}$$

$$D_{mx}\big|_{i\pm\frac{1}{2}} = \frac{D_{eff} A_x}{5.615\Delta x}\bigg|_{i\pm\frac{1}{2},j,k} \phi S_g\big|_{i\pm\frac{1}{2},j,k} y_m\big|_{i\pm\frac{1}{2},j,k}^{n+1} \tag{B.2c}$$

$$T_{wx}\big|_{i\pm\frac{1}{2}}^{n+1} = \frac{A_x k_x}{\Delta x}\bigg|_{i+\frac{1}{2},j,k} \frac{1}{\mu_w \beta_w}\bigg|_{i+\frac{1}{2},j,k}^{n+1} k_{rw}\big|_{i+\frac{1}{2},j,k}^{n+1} \tag{B.2d}$$

$$T'_{ox}\big|_{i\pm\frac{1}{2}} = \frac{1}{144}\frac{g}{g_c}\rho_o\big|_{i\pm\frac{1}{2},j,k}^{n+1} T_{ox}\big|_{i\pm\frac{1}{2}}^{n+1} \tag{B.2e}$$

$$T'_{gx}\big|_{i\pm\frac{1}{2}} = \frac{1}{144}\frac{g}{g_c}\rho_g\big|_{i\pm\frac{1}{2},j,k}^{n+1} T_{gx}\big|_{i\pm\frac{1}{2}}^{n+1} \tag{B.2f}$$

$$T'_{wx}\big|_{i\pm\frac{1}{2}} = \frac{1}{144}\frac{g}{g_c}\rho_w\big|_{i\pm\frac{1}{2},j,k}^{n+1} T_{wx}\big|_{i\pm\frac{1}{2}}^{n+1} \tag{B.2g}$$

$$T_{oy}\big|_{j\pm\frac{1}{2}}^{n+1} = \frac{A_y k_y}{\Delta y}\bigg|_{i,j\pm\frac{1}{2},k} \frac{\bar{\rho}_o}{\mu_o}\bigg|_{i,j\pm\frac{1}{2},k}^{n+1} x_m k_{ro}\big|_{i,j\pm\frac{1}{2},k}^{n+1} \tag{B.2h}$$

$$T_{gy}\big|_{j\pm\frac{1}{2}}^{n+1} = \frac{A_y k_y}{\Delta y}\bigg|_{i,j\pm\frac{1}{2},k} \frac{\bar{\rho}_g}{\mu_g}\bigg|_{i,j\pm\frac{1}{2},k}^{n+1} y_m k_{rg}\big|_{i,j\pm\frac{1}{2},k}^{n+1} \tag{B.2i}$$

$$D_{my}\big|_{j\pm\frac{1}{2}} = \frac{D_{eff} A_y}{5.615\Delta y}\bigg|_{i,j\pm\frac{1}{2},k} \phi S_g\big|_{i,j\pm\frac{1}{2},k} y_m\big|_{i,j\pm\frac{1}{2},k}^{n+1} \tag{B.2j}$$

$$T_{wy}\big|_{j\pm\frac{1}{2}} = \frac{A_y k_y}{\Delta y}\bigg|_{i,j+\frac{1}{2},k} \frac{1}{\mu_w \beta_w}\bigg|_{i,j+\frac{1}{2},k}^{n+1} k_{rw}\big|_{i,j+\frac{1}{2},k}^{n+1} \tag{B.2k}$$

$$T'_{oy}\big|_{j\pm\frac{1}{2}} = \frac{1}{144}\frac{g}{g_c}\rho_o\big|_{i,j\pm\frac{1}{2},k}^{n+1} T_{oy}\big|_{j\pm\frac{1}{2}}^{n+1} \tag{B.2l}$$

$$T'_{gy}\big|_{j\pm\frac{1}{2}} = \frac{1}{144}\frac{g}{g_c}\rho_g\big|_{i,j\pm\frac{1}{2},k}^{n+1} T_{gy}\big|_{j\pm\frac{1}{2}}^{n+1} \tag{B.2m}$$

$$T'_{wy}\big|_{j\pm\frac{1}{2}} = \frac{1}{144}\frac{g}{g_c}\rho_w\big|^{n+1}_{i,j\pm\frac{1}{2},k} T_{wy}\big|^{n+1}_{j\pm\frac{1}{2}} \tag{B.2n}$$

$$T_{oz}\big|^{n+1}_{k\pm\frac{1}{2}} = \frac{A_y k_y}{\Delta y}\bigg|_{i,j,k\pm\frac{1}{2}} \frac{\bar{\rho}_o}{\mu_o}\bigg|^{n+1}_{i,j,k\pm\frac{1}{2}} x_m k_{ro}\big|^{n+1}_{i,j,k\pm\frac{1}{2}} \tag{B.2o}$$

$$T_{gz}\big|^{n+1}_{k\pm\frac{1}{2}} = \frac{A_y k_y}{\Delta y}\bigg|_{i,j,k\pm\frac{1}{2}} \frac{\bar{\rho}_g}{\mu_g}\bigg|^{n+1}_{i,j,k\pm\frac{1}{2}} y_m k_{rg}\big|^{n+1}_{i,j,k\pm\frac{1}{2}} \tag{B.2p}$$

$$D_{mz}\big|_{k\pm\frac{1}{2}} = \frac{D_{eff}\,A_z}{5.615\Delta z}\bigg|_{i,j,k\pm\frac{1}{2}} \phi S_g\big|_{i,j,k\pm\frac{1}{2}} y_m\big|^{n+1}_{i,j,k\pm\frac{1}{2}} \tag{B.2q}$$

$$T_{wz}\big|^{n+1}_{k\pm\frac{1}{2}} = \frac{A_y k_y}{\Delta y}\bigg|_{i,j,k+\frac{1}{2}} \frac{1}{\mu_w \beta_w}\bigg|^{n+1}_{i,j,k+\frac{1}{2}} k_{rw}\big|^{n+1}_{i,j,k+\frac{1}{2}} \tag{B.2r}$$

$$T'_{oz}\big|_{k\pm\frac{1}{2}} = \frac{1}{144}\frac{g}{g_c}\rho_o\big|^{n+1}_{i,j,k\pm\frac{1}{2}} T_{oz}\big|^{n+1}_{k\pm\frac{1}{2}} \tag{B.2s}$$

$$T'_{gz}\big|_{k\pm\frac{1}{2}} = \frac{1}{144}\frac{g}{g_c}\rho_g\big|^{n+1}_{i,j,k\pm\frac{1}{2}} T_{gz}\big|^{n+1}_{k\pm\frac{1}{2}} \tag{B.2t}$$

$$T'_{wz}\big|_{k\pm\frac{1}{2}} = \frac{1}{144}\frac{g}{g_c}\rho_w\big|^{n+1}_{i,j,k\pm\frac{1}{2}} T_{wz}\big|^{n+1}_{k\pm\frac{1}{2}} \tag{B.2u}$$

The substitution of the oil and gas transmissibility terms into the finite difference equation (B.1a) for hydrocarbon would form the following expression:

$$\begin{aligned}
&T_{ox}\big|^{n+1}_{i+\frac{1}{2}}\left(p_g{}^{n+1}_{i+1,j,k} - p_g{}^{n+1}_{i,j,k}\right) - T_{ox}\big|^{n+1}_{i-\frac{1}{2}}\left(p_g{}^{n+1}_{i,j,k} - p_g{}^{n+1}_{i-1,j,k}\right)\\
&T_{gx}\big|^{n+1}_{i+\frac{1}{2}}\left(p_g{}^{n+1}_{i+1,j,k} - p_g{}^{n+1}_{i,j,k}\right) - T_{gx}\big|^{n+1}_{i-\frac{1}{2}}\left(p_g{}^{n+1}_{i,j,k} - p_g{}^{n+1}_{i-1,j,k}\right)\\
&-T_{ox}\big|^{n+1}_{i+\frac{1}{2}}\left(p_{cgo}{}^{n+1}_{i+1,j,k} - p_{cgo}{}^{n+1}_{i,j,k}\right) + T_{ox}\big|^{n+1}_{i-\frac{1}{2}}\left(p_{cgo}{}^{n+1}_{i,j,k} - p_{cgo}{}^{n+1}_{i-1,j,k}\right)\\
&+D_{mx}\big|_{i+\frac{1}{2}}\left(\bar{\rho}_g{}^{n+1}_{i+1,j,k} - \bar{\rho}_g{}^{n+1}_{i,j,k}\right) - D_{mx}\big|_{i-\frac{1}{2}}\left(\bar{\rho}_g{}^{n+1}_{i,j,k} - \bar{\rho}_g{}^{n+1}_{i-1,j,k}\right)\\
&-\Big\{T'_{ox}\big|_{i+\frac{1}{2}}\left(G^{n+1}_{i+1,j,k} - G^{n+1}_{i,j,k}\right) - T'_{ox}\big|_{i-\frac{1}{2}}\left(G^{n+1}_{i,j,k} - G^{n+1}_{i-1,j,k}\right)\\
&\qquad + T'_{gx}\big|_{i+\frac{1}{2}}\left(G^{n+1}_{i+1,j,k} - G^{n+1}_{i,j,k}\right) - T'_{gx}\big|_{i-\frac{1}{2}}\left(G^{n+1}_{i,j,k} - G^{n+1}_{i-1,j,k}\right)\Big\}
\end{aligned}$$

$$+T_{oy}\Big|_{j+\frac{1}{2}}^{n+1}\left(p_g{}_{i,j+1,k}^{n+1}-p_g{}_{i,j,k}^{n+1}\right)-T_{oy}\Big|_{j-\frac{1}{2}}^{n+1}\left(p_g{}_{i,j,k}^{n+1}-p_g{}_{i,j-1,k}^{n+1}\right)$$

$$+T_{gy}\Big|_{j+\frac{1}{2}}^{n+1}\left(p_g{}_{i,j+1,k}^{n+1}-p_g{}_{i,j,k}^{n+1}\right)-T_{gy}\Big|_{j-\frac{1}{2}}^{n+1}\left(p_g{}_{i,j,k}^{n+1}-p_g{}_{i,j-1,k}^{n+1}\right)$$

$$-T_{oy}\Big|_{j+\frac{1}{2}}^{n+1}\left(p_{cgo}{}_{i,j+1,k}^{n+1}-p_{cgo}{}_{i,j,k}^{n+1}\right)+T_{oy}\Big|_{j-\frac{1}{2}}^{n+1}\left(p_{cgo}{}_{i,j,k}^{n+1}-p_{cgo}{}_{i,j-1,k}^{n+1}\right)$$

$$+D_{my}\Big|_{j+\frac{1}{2}}\left(\bar{\rho}_g{}_{i,j+1,k}^{n+1}-\bar{\rho}_g{}_{i,j,k}^{n+1}\right)-D_{my}\Big|_{j-\frac{1}{2}}\left(\bar{\rho}_g{}_{i,j,k}^{n+1}-\bar{\rho}_g{}_{i,j-1,k}^{n+1}\right)$$

$$-\Big\{T'_{oy}\Big|_{j+\frac{1}{2}}\left(G_{i,j+1,k}^{n+1}-G_{i,j,k}^{n+1}\right)-T'_{oy}\Big|_{j-\frac{1}{2}}\left(G_{i,j,k}^{n+1}-G_{i,j-1,k}^{n+1}\right)$$

$$+T'_{gy}\Big|_{j+\frac{1}{2}}\left(G_{i,j+1,k}^{n+1}-G_{i,j,k}^{n+1}\right)-T'_{gy}\Big|_{j+\frac{1}{2}}\left(G_{i,j,k}^{n+1}-G_{i,j-1,k}^{n+1}\right)\Big\}$$

$$+T_{oz}\Big|_{k+\frac{1}{2}}^{n+1}\left(p_g{}_{i,j,k+1}^{n+1}-p_g{}_{i,j,k}^{n+1}\right)-T_{oz}\Big|_{k-\frac{1}{2}}^{n+1}\left(p_g{}_{i,j,k}^{n+1}-p_g{}_{i,j,k-1}^{n+1}\right)$$

$$+T_{gz}\Big|_{k+\frac{1}{2}}^{n+1}\left(p_g{}_{i,j,k+1}^{n+1}-p_g{}_{i,j,k}^{n+1}\right)-T_{gz}\Big|_{k-\frac{1}{2}}^{n+1}\left(p_g{}_{i,j,k}^{n+1}-p_g{}_{i,j,k-1}^{n+1}\right)$$

$$-T_{oz}\Big|_{k+\frac{1}{2}}^{n+1}\left(p_{cgo}{}_{i,j,k+1}^{n+1}-p_{cgo}{}_{i,j,k}^{n+1}\right)+T_{oz}\Big|_{k-\frac{1}{2}}^{n+1}\left(p_{cgo}{}_{i,j,k}^{n+1}-p_{cgo}{}_{i,j,k-1}^{n+1}\right)$$

$$+D_{mz}\Big|_{k+\frac{1}{2}}\left(\bar{\rho}_g{}_{i,j,k+1}^{n+1}-\bar{\rho}_g{}_{i,j,k}^{n+1}\right)-D_{mz}\Big|_{k-\frac{1}{2}}\left(\bar{\rho}_g{}_{i,j,k}^{n+1}-\bar{\rho}_g{}_{i,j,k-1}^{n+1}\right)$$

$$-\Big\{T'_{oz}\Big|_{k+\frac{1}{2}}\left(G_{i,j,k+1}^{n+1}-G_{i,j,k}^{n+1}\right)-T'_{oz}\Big|_{k-\frac{1}{2}}\left(G_{i,j,k}^{n+1}-G_{i,j,k-1}^{n+1}\right)$$

$$+T'_{gz}\Big|_{k+\frac{1}{2}}\left(G_{i,j,k+1}^{n+1}-G_{i,j,k}^{n+1}\right)-T'_{gz}\Big|_{k-\frac{1}{2}}\left(G_{i,j,k}^{n+1}-G_{i,j,k-1}^{n+1}\right)\Big\}+M_m^l$$

$$=\frac{V_b}{5.615\Delta t}\left[\left(\phi\, S_o x_m \bar{\rho}_o+\phi(1-S_o-S_w)y_m\bar{\rho}_g\right)_{i,j,k}^{n+1}-\left(\phi\, S_o x_m \bar{\rho}_o+\phi(1-S_o-S_w)y_m\bar{\rho}_g\right)_{i,j,k}^{n}\right]$$

$$;\qquad m=1,2,\ldots,n_c \qquad \ldots \text{ (B.3a)}$$

and, the substitution of the water transmissibility terms into the finite difference equation (B.2a) for water would form the following expression:

$$
\begin{aligned}
&T_{wx}\big|_{i+\frac{1}{2}}^{n+1}\left({p_g}_{i+1,j,k}^{n+1}-{p_g}_{i,j,k}^{n+1}\right)-T_{wx}\big|_{i-\frac{1}{2}}^{n+1}\left({p_g}_{i,j,k}^{n+1}-{p_g}_{i-1,j,k}^{n+1}\right)\\
&-T_{wx}\big|_{i+\frac{1}{2}}^{n+1}\left({p_{cgo}}_{i+1,j,k}^{n+1}+{p_{cow}}_{i+1,j,k}^{n+1}-{p_{cgo}}_{i,j,k}^{n+1}-{p_{cow}}_{i,j,k}^{n+1}\right)\\
&+T_{wx}\big|_{i-\frac{1}{2}}^{n+1}\left({p_{cgo}}_{i,j,k}^{n+1}+{p_{cow}}_{i,j,k}^{n+1}-{p_{cgo}}_{i-1,j,k}^{n+1}-{p_{cow}}_{i-1,j,k}^{n+1}\right)\\
&\quad-\left\{T'_{wx}\big|_{i+\frac{1}{2}}\left(G_{i+1,j,k}^{n+1}-G_{i,j,k}^{n+1}\right)-T'_{wx}\big|_{i-\frac{1}{2}}\left(G_{i,j,k}^{n+1}-G_{i-1,j,k}^{n+1}\right)\right\}\\
&+T_{wy}\big|_{j+\frac{1}{2}}^{n+1}\left({p_g}_{i,j+1,k}^{n+1}-{p_g}_{i,j,k}^{n+1}\right)-T_{wy}\big|_{j-\frac{1}{2}}^{n+1}\left({p_g}_{i,j,k}^{n+1}-{p_g}_{i,j-1,k}^{n+1}\right)\\
&-T_{wy}\big|_{j+\frac{1}{2}}^{n+1}\left({p_{cgo}}_{i,j+1,k}^{n+1}+{p_{cow}}_{i,j+1,k}^{n+1}-{p_{cgo}}_{i,j,k}^{n+1}-{p_{cow}}_{i,j,k}^{n+1}\right)\\
&+T_{wy}\big|_{j-\frac{1}{2}}^{n+1}\left({p_{cgo}}_{i,j,k}^{n+1}+{p_{cow}}_{i,j,k}^{n+1}-{p_{cgo}}_{i,j-1,k}^{n+1}-{p_{cow}}_{i,j-1,k}^{n+1}\right)\\
&\quad-\left\{T'_{wy}\big|_{j+\frac{1}{2}}\left(G_{i,j+1,k}^{n+1}-G_{i,j,k}^{n+1}\right)-T'_{wy}\big|_{j-\frac{1}{2}}\left(G_{i,j,k}^{n+1}-G_{i,j-1,k}^{n+1}\right)\right\}\\
&+T_{wz}\big|_{k+\frac{1}{2}}^{n+1}\left({p_g}_{i,j,k+1}^{n+1}-{p_g}_{i,j,k}^{n+1}\right)-T_{wz}\big|_{k-\frac{1}{2}}^{n+1}\left({p_g}_{i,j,k}^{n+1}-{p_g}_{i,j,k-1}^{n+1}\right)\\
&-T_{wz}\big|_{k+\frac{1}{2}}^{n+1}\left({p_{cgo}}_{i,j,k+1}^{n+1}+{p_{cow}}_{i,j.k+1}^{n+1}-{p_{cgo}}_{i,j,k}^{n+1}-{p_{cow}}_{i,j,k}^{n+1}\right)\\
&+T_{wz}\big|_{k-\frac{1}{2}}^{n+1}\left({p_{cgo}}_{i,j,k}^{n+1}+{p_{cow}}_{i,j,k}^{n+1}-{p_{cgo}}_{i,j,k-1}^{n+1}-{p_{cow}}_{i,j,k-1}^{n+1}\right)\\
&\quad-\left\{T'_{wz}\big|_{k+\frac{1}{2}}\left(G_{i,j,k+1}^{n+1}-G_{i,j,k}^{n+1}\right)-T'_{wz}\big|_{k-\frac{1}{2}}\left(G_{i,j,k}^{n+1}-G_{i,j,k-1}^{n+1}\right)\right\}\\
&+q_{sc,w}^{l}=\frac{V_b}{5.615\Delta t}\left[\left(\frac{\phi\,S_w}{\beta_w}\right)_{i,j,k}^{n+1}-\left(\frac{\phi\,S_w}{\beta_w}\right)_{i,j,k}^{n}\right]
\end{aligned}
\qquad \ldots \text{(B.3b)}
$$

The flow of fluids expressed by equation (B.3a) and (B.3b) which governs the inflow, outflow, and the accumulation at the gridblocks of the control volume described in Chapter 4, can be reduced to a shorter form which will be used later on to solve for the unknowns using Newton Raphson method. Equations (B.3a) and (B.3b) can be described in terms of interfacial molar flows ($\widehat{N}_m$) in three flow directions (x, y, and z) as illustrated in the following expressions:
For hydrocarbon flowing in the x, y, and z direction respectively:

$$\widehat{N}_{m\,i\pm\frac{1}{2}}^{\,n+1} = \left(T_{ox}|_{i\pm\frac{1}{2}}^{n+1} + T_{gx}|_{i\pm\frac{1}{2}}^{n+1}\right)\left(p_{g\,i\pm1,j,k}^{\,n+1} - p_{g\,i,j,k}^{\,n+1}\right) - T_{ox}|_{i\pm\frac{1}{2}}^{n+1}\left(p_{cgo\,i\pm1,j,k}^{\,n+1} - p_{cgo\,i,j,k}^{\,n+1}\right)$$
$$+D_{mx}|_{i\pm\frac{1}{2}}\left(p_{g\,i\pm1,j,k}^{\,n+1} - p_{g\,i,j,k}^{\,n+1}\right) + \left(T'_{ox}|_{i\pm\frac{1}{2}} + T'_{gx}|_{i\pm\frac{1}{2}}\right)\left(G_{i\pm1,j,k} - G_{i,j,k}\right) \qquad \text{(B.4a)}$$

$$\widehat{N}_{m\,j\pm\frac{1}{2}}^{\,n+1} = \left(T_{oy}|_{j\pm\frac{1}{2}}^{n+1} + T_{gy}|_{j\pm\frac{1}{2}}^{n+1}\right)\left(p_{g\,i,j\pm1,k}^{\,n+1} - p_{g\,i,j,k}^{\,n+1}\right) - T_{oy}|_{j\pm\frac{1}{2}}^{n+1}\left(p_{cgo\,i,j\pm1,k}^{\,n+1} - p_{cgo\,i,j,k}^{\,n+1}\right)$$
$$+D_{my}|_{j\pm\frac{1}{2}}\left(p_{g\,i,j\pm1,k}^{\,n+1} - p_{g\,i,j,k}^{\,n+1}\right) + \left(T'_{oy}|_{j\pm\frac{1}{2}} + T'_{gy}|_{j\pm\frac{1}{2}}\right)\left(G_{i,j\pm1,k} - G_{i,j,k}\right) \qquad \text{(B.4b)}$$

$$\widehat{N}_{m\,k\pm\frac{1}{2}}^{\,n+1} = \left(T_{oz}|_{k\pm\frac{1}{2}}^{n+1} + T_{gz}|_{k\pm\frac{1}{2}}^{n+1}\right)\left(p_{g\,i,j,k\pm1}^{\,n+1} - p_{g\,i,j,k}^{\,n+1}\right) - T_{oz}|_{k\pm\frac{1}{2}}^{n+1}\left(p_{cgo\,i,j,k\pm1}^{\,n+1} - p_{cgo\,i,j,k}^{\,n+1}\right)$$
$$+D_{mz}|_{k\pm\frac{1}{2}}\left(p_{g\,i,j,k\pm1}^{\,n+1} - p_{g\,i,j,k}^{\,n+1}\right) + \left(T'_{oz}|_{k\pm\frac{1}{2}} + T'_{gz}|_{k\pm\frac{1}{2}}\right)\left(G_{i,j,k\pm1} - G_{i,j,k}\right) \qquad \text{(B.4c)}$$

For water flowing in the x, y, and z direction respectively:

$$\widehat{N}_{w\,i\pm\frac{1}{2}}^{\,n+1} = T_{wx}|_{i\pm\frac{1}{2}}^{n+1}\left(p_{g\,i\pm1,j,k}^{\,n+1} - p_{g\,i,j,k}^{\,n+1}\right)$$
$$-T_{wx}|_{i\pm\frac{1}{2}}^{n+1}\left(p_{cgo\,i\pm1,j,k}^{\,n+1} + p_{cow\,i\pm1,j,k}^{\,n+1} - p_{cgo\,i,j,k}^{\,n+1} - p_{cow\,i,j,k}^{\,n+1}\right)$$
$$-T'_{wx}|_{i\pm\frac{1}{2}}\left(G_{i\pm1,j,k} - G_{i,j,k}\right) \qquad \text{(B.4d)}$$

$$\widehat{N}_{w_{j\pm\frac{1}{2}}}^{n+1} = T_{wy}\big|_{k\pm\frac{1}{2}}^{n+1}\left(p_{g_{i,j\pm1,k}}^{n+1} - p_{g_{i,j,k}}^{n+1}\right)$$

$$-T_{wy}\big|_{k\pm\frac{1}{2}}^{n+1}\left(p_{cgo_{i,j\pm1,k}}^{n+1} + p_{cow_{i,j\pm1,k}}^{n+1} - p_{cgo_{i,j,k}}^{n+1} - p_{cow_{i,j,k}}^{n+1}\right)$$

$$-T'_{wy}\big|_{k\pm\frac{1}{2}}\left(G_{i,j\pm1,k} - G_{i,j,k}\right) \qquad \text{(B.4e)}$$

$$\widehat{N}_{w_{k\pm\frac{1}{2}}}^{n+1} = T_{wz}\big|_{k\pm\frac{1}{2}}^{n+1}\left(p_{g_{i,j,k\pm1}}^{n+1} - p_{g_{i,j,k}}^{n+1}\right)$$

$$-T_{wz}\big|_{k\pm\frac{1}{2}}^{n+1}\left(p_{cgo_{i,j,k\pm1}}^{n+1} + p_{cow_{i,j,k\pm1}}^{n+1} - p_{cgo_{i,j,k}}^{n+1} - p_{cow_{i,j,k}}^{n+1}\right)$$

$$-T'_{wz}\big|_{k\pm\frac{1}{2}}\left(G_{i,j,k\pm1} - G_{i,j,k}\right) \qquad \text{(B.4f)}$$

The representation of equations (B.4a) and (B.4b) after the substitution would result in the final form of the molar flow expressed at the interfaces as shown below:

$$\widehat{N}_{m_{i+\frac{1}{2}}}^{n+1} + \widehat{N}_{m_{i-\frac{1}{2}}}^{n+1} + \widehat{N}_{m_{i+\frac{1}{2}}}^{n+1} + \widehat{N}_{m_{i-\frac{1}{2}}}^{n+1} + \widehat{N}_{m_{i+\frac{1}{2}}}^{n+1} + \widehat{N}_{m_{i-\frac{1}{2}}}^{n+1} + \widehat{N}_{m_{i+\frac{1}{2}}}^{n+1} + M_m^l$$
$$= \frac{V_b}{5.615\Delta t}\left[\left(\phi\, S_o x_m \bar{\rho}_o + \phi(1 - S_o - S_w) y_m \bar{\rho}_g\right)_{i,j,k}^{n+1} - \left(\phi S_o x_m \bar{\rho}_o + \phi(1 - S_o - S_w) y_m \bar{\rho}_g\right)_{i,j,k}^{n}\right]$$
$$; \qquad m = 1, 2, \ldots, n_c \qquad \ldots \text{(B.5a)}$$

$$\widehat{N}_{w_{i+\frac{1}{2}}}^{n+1} + \widehat{N}_{w_{i-\frac{1}{2}}}^{n+1} + \widehat{N}_{w_{i+\frac{1}{2}}}^{n+1} + \widehat{N}_{w_{i-\frac{1}{2}}}^{n+1} + \widehat{N}_{w_{i+\frac{1}{2}}}^{n+1} + \widehat{N}_{w_{i-\frac{1}{2}}}^{n+1} + \widehat{N}_{w_{i+\frac{1}{2}}}^{n+1} + q_{sc,w}^l$$
$$= \frac{V_b}{5.615\Delta t}\left[\left(\frac{\phi\, S_w}{\beta_w}\right)_{i,j,k}^{n+1} - \left(\frac{\phi\, S_w}{\beta_w}\right)_{i,j,k}^{n}\right] \qquad \ldots \text{(B.5b)}$$